공학박사학위논문

A study on design and realization of layered bistable shell structures with arbitrary shape

임의의 형상을 가지는 쌍안정 적층 쉘 구조물의 형상 구현 방법에 관한 연구

2016년 2월

서울대학교 대학원

기계항공공학부

이 종 구

Abstract

In this dissertation, the numerical analysis model and design technique of plate and shell is proposed based on the Gauss's Theorema Egregium, in order to materialize the bistable shell structure with arbitrary shape. The classical bistable plate and shell structure is limited to the cylindrical shape. Besides which, the curvature value of cylindrical shape does not change independently without changing the thickness and material locally. The morphological limitation is blocking progress in the application research on the bistable plate and shell structure. In summary, this problem is categorized into two main engineering issue: 'how to change the cylindrical curvature value of classical bistable structure?' and 'how to induce the bistable structure with non-cylindrical shape?'. In order to address this problem, firstly, curvature tailoring technique of classical bistable shell structure is suggested by using the initially curved tool-plate. The suggested method is verified by Rayleigh-Ritz analysis and experiment.

Secondly, second-generation technique which inducing bistable structure with arbitrary shape is proposed based on the Gauss's Theorema Egregium. The suggested method is also verified numerically and experimentally.

Specifically, the second-generation technique, which inducing bistable structure with arbitrary shape, is motivated from the geometrical characteristic that shear deformation does not occur in the case of transformation between two isometric surfaces. Based on this geometrical characteristic, the realization

method of bistable shell structure with arbitrary shape is suggested through face-to-face perfect bonding of two non-developable surfaces.

In the analysis of bistable structure in order to handle the above issue, various efficient and accurate numerical models are developed.

Firstly, the classical bistable structure analysis model is mostly based on displacement field in order to build up the total potential energy. However, the total potential energy is not explicitly expressed by displacement field. For this reason, the analysis from the model based on the displacement field is not efficient. In order to address this problem, the new analysis model is proposed, which is combining the approximated implicit strain field and the compatibility equation. The efficiency and accuracy of the suggested model is validated, by comparing with the result obtained by FE analysis.

Secondly, the classical bistable structure analysis model is mostly based on the plate theory due to the limitation of numerical derivative precision and the complexity of calculation, although the deformed curvature of bistable plate and shell is large. In this dissertation, however, in order to obtain the accurate solution, the bistable structure analysis model is developed based on the shell theory. In the development of corresponding shell model, the limitation problem of numerical derivative precision and the complexity of calculation are addressed by utilizing the matrix derivative method. As a result, the analysis of bistable plate and shell has become so accurately and so easily.

Finally, for the practical application of the bistable shell structure, the effect of initial shape of bistable shell structure on the snap-through load is studied. Based on the snap-through load obtained from numerical analysis, the Shape memory alloy spring is suggested as actuator. At first, specification of SMA spring is suggested. The performance of SMA spring is simulated by FE analysis where the constitutive model of shape memory alloy is implemented based on the Lagoudas model. Then, for the verification of snap-through by means of SMA spring, snap-through FE analysis of the bistable structure with SMA spring is performed. From this FE analysis, it is verified that the snap-through of bistable shell structure is well induced when SMA spring is utilized as actuator.

The morphological design technique and model of bistable plate and shell structure, which are developed and verified in the dissertation, overcome the morphological limitation of the existing bistable structure and improve the design degree freedom of it. If the improved design degree freedom and the bistability is applied into the classic mechanical system which have been focus on the mechanical property (i.e. strength or mass), the new mechanical system accompanied by the concept of morphing can be designed and expected as the high value-added system breaking stereotype.

Key word: Bistability, Plate and shell, Gauss's Theorema Egregium, Compatibility equation, Shape Memory Alloy spring

Student Number: 2009-23913

CONTENTS

Part Ⅱ: Bistable structure with non-zero Gaussian curvature

LIST OF FIGURES

LIST OF TABLES

Chapter 1

Introduction

1.1 Paradigm change of structures

The study of the elastic [1, 2] or inelastic structure is experiencing a paradigm change from classical structures with load-carrying capacity to smart structure with self-adapting capacity for service environment. Adapting capacity of smart structure comes from the nonlinear behavior of structure itself (i.e. buckling and phase transformation which are accompanied by rapid large deformation and rapid energy release) [3]. In the past, buckling phenomenon, one of the research field of elastic, such as wrinkling, snapping is treated as something to avoid by considering the load carrying capacity. However, except for the load carrying capacity, post-bucking has good structural characteristics which are related to a rapid energy release and a rapid motion within elastic region of structure (i.e. without permanent deformation or plastic behavior). These characteristics of post-buckling of smart structure are attractive for the application of energy harvesting and morphing structure because the aspects of smart structure (i.e.

rapid energy release and rapid motion with large deformation) expand the performance, which is not expected with just using classical structure [4].

For this reasons, the researcher in the field of biomimetic[5], energy related application[6-22], and aerodynamics[23-29] are focusing the smart structure with non-trivial deformation in order to improve the performance of the mechanical device itself or to mimic the nature of creatures like real thing.

1.2 Bistable structure or composites

Among of the smart structures with non-trivial deformation, bistable structure or composite are suitable for the needs of researcher. Bistable composites have two stable shape as shown in Figure 1.1 (cylindrical shapes [30-36] or saddle shapes [37])as a result of the coupling effect between their residual stress and geometric nonlinearity. These composites can be snapped through as shown in Figure 1.2 (i.e. from one stable shape to the other at a specific mechanical load) [38-40]. During this snap-through action, a large out-of-plane deflection occurs at a fast time scale with respect to quasi-static phenomena. After snap-through, the bistable composites remain in a stable state without requiring any additional energy supply to maintain a constant shape. Owing to these interesting properties, bistable composites have attracted research attention in the fields of aerodynamics, energy harvesting and robotics for developing a high-energy-efficiency morphing structure or device [5, 12, 16, 23-29].

1.3 Literature survey

Bistability of unsymmetric laminated composite plates has been first reported by Hyer[30]. He reported that bistability is induced by the coupling effect between a thermal residual stress and geometric nonlinearity; and the cured shapes of bistable composite laminates have been investigated by Rayleigh-Ritz analysis [31]. Since Hyer provided the new perspective about the unsymmetric laminate composites, over the past 30 years, a considerable number of advanced studies have been progressed on the cured shape of bistable composites. Jun and Hong proposed the modified model by adding more polynomial terms into Hyer's displacement field to consider the shear strain[32, 33]. They found that the shear strain has non-negligible value when width-to-thickness ratio is closest to bi-furcation point. Conversely, they found that the shear strain is negligible when width-to-thickness ratio is far away from bi-furcation point. Cho et al. [35]; and Cho and Roh [36] considered the slippage effect resulting from interaction between a tool-plate and laminates by introducing a dimensionless slippage effect. They observed that the cured shape is also affected by the type of the tool-plate and the thickness of laminates. Ren et al. estimated the cured shape of cross-ply composite thin shells with initial curvature implicitly using the Rayleigh-Ritz energy method [34]. Ryu et al. developed an explicit model to easily estimate the final curvature of unsymmetric cross-ply laminates cured on an initially curved tool plate [41]. They showed that x-direction final curvature

which is parallel to the initial curvature of tool-plate, increases as much as the added initial curvature and the y-direction final curvature, however, is not affected by the initial curvature. Kebadze, Seffen and Guest investigated the steel-type bistable structures and the bistability of these structures results from the mechanical residual stress induced by plastic bending [42, 43].

In recent years, a considerable number of studies have focused not only on the cured shapes of the bistable structures, but also on the practical application of the bistable structures. In the aerodynamic engineering field, Mattioni et al. suggested the concept for a morphing airfoil based on bistable laminated composite structures [23]. Schultz developed an airfoil-like active twisting structure using the bistable laminated composites [24]. In the energy harvesting field, Betts et al. presented the energy harvesting device using the bistable composite plates with bonded piezoelectric patches for an effective energy harvesting across broad-frequency bandwidth. In the bio-mimetic field [16], Kim et al developed the flytrap robot employing the cross-ply laminated bistable composite, which is inspired by the snap-through motion of bistable composites. The bistable flytrap robot concept is similar to the prey capture behavior of the Venus flytrap [44].

1.4 Issues of bistable structure or composites

Generally, morphing structures such as a morphing wing or a flytrap-inspired robot require different stable shapes and different structural stabilities depending on the circumstances (e.g., the flight condition or the open and closed states of a flytrap) [24, 26]. For this reason, the snap-through load, the cured curvatures or shape of bistable structure should be designed differently in each stable state depending on the design requirement.

Unfortunately, this adjustment is not easy to perform, because unsymmetric cross-ply laminates are ordinarily cured on a flat tool plate. Moreover, if the laminates have an alternating layers of orthotropic laminae with equal thickness and identical material properties on both sides of the mid-plane axis, e.g., [90°/0°], [90°/0°/90°/0°], or [90°/90°/0°/0°], the cured curvatures of both the stable states are forced to be identical to each other, and so are the snap-through loads of these states.

Although the desired result is expected to be obtained by the modification of the lay-up sequence of laminates, e.g., [90°/90°/90°/0°/0°], this approach results in alteration of other design-dependent variables (e.g., the thickness and stiffness of laminates). As a result, this design approach of bistable composites results in a structurally overweight or a mechanically over-stiff composite. Therefore, to be able to apply the design of bistable composites more flexibly to morphing structures, it would be desirable to consider a method for adjusting the cured

curvature or the snap-through load while minimizing the change in the design-dependent variables.

Several strategies were introduced to address this problem. These can be categorized into three strategies. One strategy is to connect the different angle-ply laminated composites with each other in parallel or series [45-47]. From this strategy, the multi-stable shape of bistable composite was attained and controlled without changing the thickness of composite. Another strategy is to prestress the selected plies of sysmmetric laminates before curing process by means of the specifically manufactured prestress machine [48, 49]. The snap-through load and curvature of the symmetric laminated composites was tailored by unsymmetrically prestressing on the basis of the neutral axis. Other approach is to apply an initial curvature to unsymmetric laminated composites by using an initially curved tool plate. In this approach, the initial curvature of the tool plate affects the cured curvature while keeping the thickness and stiffness of the composites.

Although mentioned strategies had been introduced, classically, these studies have something in common limitations and issues. Firstly, the method using initial tool curvature was limited to tailoring the curvature of only one state of the two equilibrium state. Therefore, the curvature of the other state mode cannot be tailored in the bistable CFRP cross-ply laminates as shown in Figure 1.3.

Secondly, the shape of bistable CFRP cross-ply laminates is limited to constant cylindrical curvatures. In the practical biological system or mechanical system, cylindrical bistable panel is not adequate. Actually, it is not easy for bistable composite cylinder to mimic entirely Venus flytrap due to its complex shape; the shape of the Venus flytrap is more like a saddle shape (non-developable surface), not a cylindrical shape. These limitations are obstacles to extend the potential of the bistable composites to more practical applications.

Finally, although the previous paper [34, 41] did not focus on the snap-through load, the change of snap-through load with changing the curvature or shape of bistable must be predicted and estimated. Because snap-through load is another important design factor in the practical application of morphing structures that are based on the snap-through action of bistable composites.

1.5 Objectives and Contributions

Based on these issues of bistable structure makes, this thesis mainly focus on how to tailor and realize the shape of bistable structures generally; and how to predict snap-through load of its. Unlike with controlling only one state curvature of the two equilibrium state with initial curvature, general method has a need to show a capacity which controls both state curvatures of the two equilibrium states. Moreover, unlike with the classical bistable structure with cylindrical

shape, general method has a need to show a capacity which realizes the non-cylindrical shape of bistable structure (i.e. non-zero Gaussian curvature). In order to satisfy these needs, various numerical models were developed and thus numerical models were verified by comparing the numerical solution with FE solution. The major contributions of this dissertation are listed as follow:

- Method to control cured curvatures of bistable composites at the both two stable state by using misalignment between unsymmetrically laminated composites and tool plate
- Development of snap-through load analysis technique and model.
- Realization of the bistable structure with non-zero Gaussian curvature at the both two stable state.
- Development of analysis model of bistable structure based on the assumed strain field which satisfy the compatibility.
- Manufacture of the bistable structure with non-zero Gaussian curvature.

1.6 Organization

Depending on the shape type of bistable structure, this thesis is mainly organized into two parts as follow: bistable structure with zero Gaussian curvature and bistable structure with non-zero Gaussian curvature. In Part Ⅰ, bistable structure with zero Gaussian curvature is described. Firstly, in Chapter 2, curvature tailoring technique of bistable composite with misalignment is described. Analysis procedure is described based on Rayleigh-Ritz approach. The advantage of suggested curvature tailoring technique will be described based on the result obtained by developed analytical model. In Chapter 3, Effect of initial curvature on the snap-through load of bistable composite is described to design the snap-through load of bistable composite with initial curvature. The qualitatively change of snap-through load is effectively obtained by Rayleigh-Ritz analysis which apply moment equilibrium condition with Lagrange multiplier. In the view point of designer, the advantage of suggested curvature tailoring technique will be described again based on the result obtained by developed analytical model. In Chapter 4, FE model of bistable shell structure with Shape Memory Alloy coil spring is described. Why SMA spring is selected as actuator to trigger the snap-through action, will be discussed based on the large recovery force and large recovery deformation of SMA spring. Next, in order to simulate the behavior of SMA spring, Lagoudas model, which is most well-known 3D SMA model, will be described. Finally, after integrating the

SMA spring over bistable composite, snap-through action will be triggered by considering actuation condition.

In Part Ⅱ, bistable structure with non-zero Gaussian curvature is described. In Chapter 5, Why Saddle shape bistable shell structure is possible, will be discussed based on the Gauss's Theorema Egregium [50]. In order to verify it, analytical model will be developed by assuming strain field of saddle shape panel. The result obtained by the analytical model will show that bistability can exist in the saddle shape (i.e. non-zero Gaussian curvature). In Chapter 6, analysis model of saddle shape bistable structure based on the assumed strain field, which satisfy the compatibility condition, will be developed in order to analyze and design bistable structure with more complex shape, not merely cylindrical shape or saddle shape. In Chapter 7, Saddle shape bistable shell structure with large curvature, is described based on the shell theory. By defining Green-Langrage strain field from difference between metric tensors of unreformed and deformed configuration, the analytical model, which can represent the large curvature of structure, will be developed. The developed model will be verified by comparing with FE solution. Additionally, manufacturing process of saddle shape bistable shell structure will be expressed. Finally, mechanical meanings and significance of this thesis is summarized in Chapter 8.

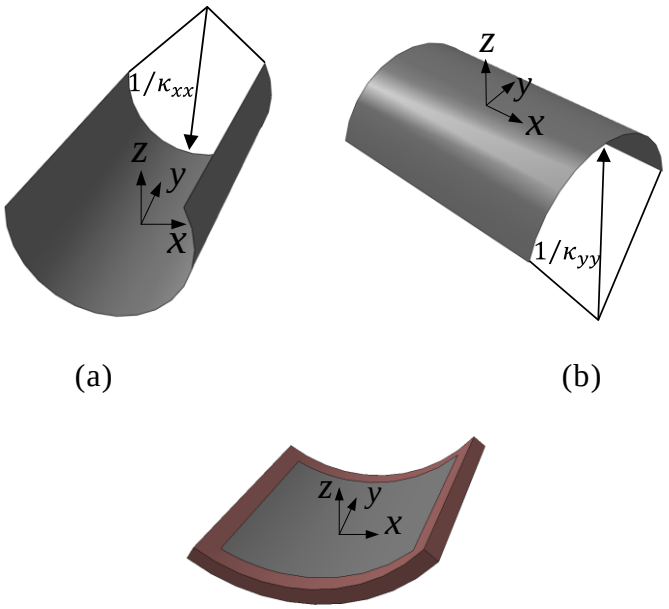

(a) (b)

(c)

Figure 1.1 Two stable configurations of bistable composites:

(a) Mode 1: $\kappa_{xx} > 0, \kappa_{yy} \approx 0$; (b) Mode 2: $\kappa_{xx} \approx 0, \kappa_{yy} < 0$; and (c) tool plate:

$$\kappa_{xx} \neq 0, \kappa_{yy} = 0.$$

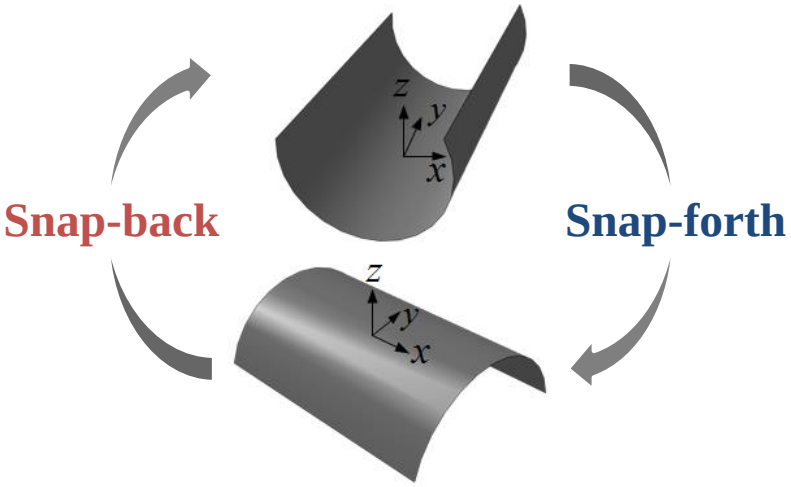

Figure 1.2 Schematic of snap-forth and snap-back processes.

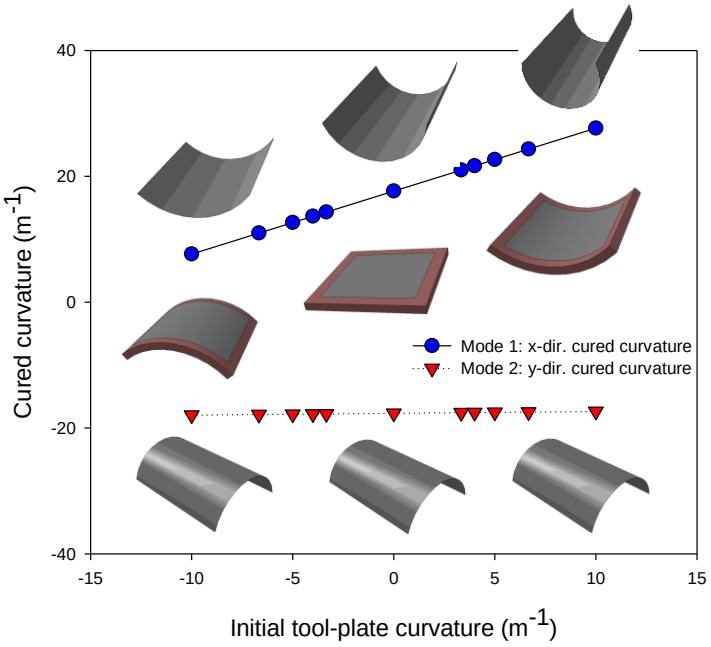

Figure 1.3 Cured curvature as a function of x-directional initial tool-plate curvature.

Chapter 2

Curvature tailoring of bistable composite with misalignment

2.1 Introduction

Inducing an initial curvature is advantageous for tailoring the curvature of bistable Carbon Fiber Reinforced Prepreg (CFRP) laminate because the final curvature of the laminate can be tailored without changing its mechanical properties, i.e., bending rigidity, thickness, and weight. However, curvature tailoring with initial curvature has been limited to tailoring the curvature of only one state of the two equilibrium states. In this chapter, a curvature tailoring scheme, which can tailor the curvatures of both equilibrium states, is proposed by misaligning the laminate and the cylindrical tool-plate for curing. This method is verified by analysis with the Rayleigh-Ritz method and experiments. In addition, explicit equations to determine the misalignment angle and tool-plate curvature are derived for curvature tailoring of the bistable CFRP cross-ply laminates. These equations provide a simple engineering guideline for designers

of bistable CFRP cross-ply laminate. The proposed curvature tailoring method gives the designer the ability to select the curvature of both equilibrium states without changing its mechanical properties, and increasing the functionality of bistable CFRP laminates.

2.2 Analytical model development

To describe the effect of initial curvature with misalignment, the Green-Lagrangian strain field proposed in a previous study [41] must be generalized. The key feature required to describe the initial curvature effect in the previous study is the rearrangement of Green-Lagrangian strain field, which is described in Eq. (2.1); a flat reference state is introduced to define the final strain field and define the initial strain, (i. e. a kind of inelastic strain). This concept is illustrated in Figure 2.1.

$$E_{ij} = \frac{1}{2}\left(g_{ij} - G_{ij}\right) = \frac{1}{2}\left(g_{ij} - \delta_{ij}\right) - \frac{1}{2}\left(G_{ij} - \delta_{ij}\right) = E_{ij}^{fianl} - E_{ij}^{initial} \tag{2.1}$$

where, g_{ij} is the metric at final state and G_{ij} is the metric at initial state.

A trigonometric displacement field, the basis of the Green-Lagrangian strain field for constant curvature assumption, provides more accurate results than a quadratic displacement field [30]. The Green-Lagrangian strain field to describe initial curvature without the misalignment angle between the bistable CFRP

cross-ply laminate and tool-plate is described by

$$\begin{bmatrix} E_{xx} \\ E_{yy} \\ 2E_{xy} \end{bmatrix} = \left\{ \begin{bmatrix} \xi_{xx} + \lambda_{xx} y^2 \\ \xi_{yy} + \lambda_{yy} x^2 \\ \left(\kappa_{xx}\kappa_{yy} + 2\lambda_{xx} + 2\lambda_{yy} \right) xy \end{bmatrix} - \begin{bmatrix} \kappa_{xx} - \kappa_{xx}^{initial} \\ \kappa_{yy} - \kappa_{yy}^{initial} \\ 0 \end{bmatrix} z \right\} \tag{2.2}$$

where, ξ_{xx}, ξ_{yy}, ξ_{xy}, means constant strains, λ_{xx}, λ_{yy}, means constants for quadratic normal strain variation, κ_{xx}, κ_{yy}, means principal curvature values after curing, and $\kappa_{xx}^{initial}$, $\kappa_{yy}^{initial}$ means initial curvature values.

The Green-Lagrangian strain field in Eq. (2.2) does not contain constant shear strain and twisting curvature because it is applied to bistable CFRP cross-ply laminate and the non-zero curvature direction of the tool-plate is aligned with the fiber direction. However, as shown in Eq. (2.3), the misalignment angle φ has an additive effect the both normal curvatures that have non-zero values, although the tool-plate has only one non-zero principal curvature value. A graphical illustration of the coordinate system is shown in Figure 2.2. It should be noted that the reference of the coordinate system is the fiber direction of the laminate; a fiber angle of 0° means that the fiber direction is aligned to the x-direction and a fiber angle of 90° means that the fiber direction is aligned to y-direction. Positive curvature indicates convex shape. As a result, the non-zero tool plate curvature, κ, in Figure 2.2 (a) has a negative value. Initial curvature tensor with misalignment angle φ is described by

$$\kappa^{initial} = \begin{bmatrix} \kappa \sin^2 \varphi & -\kappa \sin \varphi \cos \varphi \\ -\kappa \sin \varphi \cos \varphi & \kappa \cos^2 \varphi \end{bmatrix} \tag{2.3}$$

where, misalignment angle between principal curvature directions of tool plate and material axis of the laminate, φ, is illustrated in Figure 2.2 (b).

Constant shear strain and twisting curvature should be considered in the strain field because the initial twisting curvature can affect not only the final twisting curvature but also shear strain. However, it should be noted that the constant curvature assumption is still valid because the tool plate curvature, κ, is constant in the overall domain of the laminate. As a result, the final shape of the bistable CFRP laminate is cylindrical because this is the only surface that can satisfy the requirement for a constant curvature surface and developable surface.

In this sense, using a strain field for an unsymmetric angle-ply laminate [33] is an efficient scheme to accomplish this generalization because it can describe the degrees of freedoms - constant shear strain and twisting curvature - with a minimum of unknowns. Combining this scheme with the initial curvature formulation, Eq. (2.1), describes the general deformation behavior of a bistable CFRP laminate with sufficiently long side length. The generalized Green-Lagrangian strain field is described by

$$\begin{bmatrix} E_{xx} \\ E_{yy} \\ 2E_{xy} \end{bmatrix} = \begin{bmatrix} \xi_{xx} \\ \xi_{yy} \\ \xi_{xy} \end{bmatrix} + \begin{bmatrix} m^2 & n^2 & -mn \\ n^2 & m^2 & mn \\ 2mn & -2mn & m^2 - n^2 \end{bmatrix} \left(\begin{bmatrix} \lambda_{xx} y'^2 \\ \lambda_{yy} x'^2 \\ \left(\kappa_1 \kappa_2 + 2\lambda_{xx} + 2\lambda_{yy} \right) x' y' \end{bmatrix} - \begin{bmatrix} \kappa_1 \\ \kappa_2 \\ 0 \end{bmatrix} z \right) + \begin{bmatrix} \kappa_{xx}^{initial} \\ \kappa_{yy}^{initial} \\ 2\kappa_{xy}^{initial} \end{bmatrix} z \tag{2.4}$$

where, ξ_{xx}, ξ_{yy}, ξ_{xy}, means constant strains λ_{xx}, λ_{yy}, constants for quadratic normal strain variation, κ_1, κ_2, principal curvature values, and θ means angle difference between principal curvature direction and material coordinate. in addition, $m=\cos\theta$, $n= \sin\theta$, $x'=mx+ny$, and $y'=-nx+my$.

Calculation of the unknown variables in Eq. (2.4), ξ_{xx}, ξ_{yy}, ξ_{xy}, λ_{xx}, λ_{yy}, κ_1, κ_2, and θ is the same as in previous study [30]. Minimizing the strain energy function using the Newton-Raphson iteration procedure, the equilibrium states can be determined by obtaining the unknown variables in Eq. (2.4). The Strain energy function with proposed strain field and thermal strain is described by

$$U = \frac{1}{2}\int_V C_{ijkl}\left(E_{ij} - \alpha_{ij}\Delta T\right)\left(E_{kl} - \alpha_{kl}\Delta T\right)dV = U_{\text{normal}} + U_{\text{shear}} + U_{\text{coupling}} \tag{2.5}$$

where, U_{normal}: (i=j & k=l), U_{shear}: (i≠j & k≠l), $U_{couplig}$: other indices, detail expressions of U_{normal}, U_{shear}, and $U_{coupling}$ is described in Appendix A.

The proposed strain field which is described in Eq. (2.4) can handle the initial curvature effect with misaligned fiber angle configuration for angle-ply as well as cross-ply laminate. The final curvature prediction from the strain field given in Eq. (2.4) cannot be made in simple explicit manner because final curvature direction can be changed when lay-up sequence changes or initial curvature in Eq. (2.3) changes.

In the case of cross-ply laminates, however, explicit prediction of final curvature

can be made even including the effect of initial curvature with misalignment angle. Final curvature direction of unsymmetric cross-ply laminate should be aligned with fiber directions because the difference of the thermal expansion coefficients between layers is maximized along that directions and they are orthogonal to each other. As a result, strain field in Eq. (2.4) can be reduced to the following compact equation for the cross-ply laminate configuration because m=1 and n=0. The reduced Green-Lagrangian strain filed for cross-ply laminate is described by

$$\begin{bmatrix} E_{xx} \\ E_{yy} \\ 2E_{xy} \end{bmatrix} = \begin{bmatrix} \xi_{xx} \\ \xi_{yy} \\ \xi_{xy} \end{bmatrix} + \begin{bmatrix} \lambda_{xx} y^2 \\ \lambda_{yy} x^2 \\ \left(\kappa_1 \kappa_2 + 2\lambda_{xx} + 2\lambda_{yy}\right) xy \end{bmatrix} - \begin{bmatrix} \kappa_1 - \kappa_{xx}^{initial} \\ \kappa_2 - \kappa_{yy}^{initial} \\ 2\kappa_{xy}^{initial} \end{bmatrix} z \tag{2.6}$$

Final curvatures, κ_1 and κ_2, can be predicted in explicit manner for the following reasons. First, minimizing strain energy in Eq. (2.5) for the cross-ply laminates is the sum of minimal normal strain energy and minimal shear strain energy, i.e. coupling strain energy, $U_{coupling}$, is zero. Second, the principal curvature values, κ_1 and κ_2, become independent of the shear strain. It is because second terms of in-plane shear strain in Eq. (2.6) yields to zero as the side length of the laminate increases[32, 38]. Therefore, principal curvature values of the bistable laminate, κ_1 and κ_2, can be determined by minimizing the normal strain energy only. It should be noted that normal strain field in Eq. (2.6) is same as that of Eq. (2.2).

In this sense, explicit approximation scheme in previous study [41] is still valid.

The detailed derivation is given below. First, force/moment balance equations for classical lamination theory are given by

$$\begin{bmatrix} A_{11} & B_{11} & A_{12} & B_{12} & 0 & 0 \\ B_{11} & D_{11} & B_{12} & D_{12} & 0 & 0 \\ A_{12} & B_{12} & A_{22} & B_{22} & 0 & 0 \\ B_{12} & D_{12} & B_{22} & D_{12} & 0 & 0 \\ 0 & 0 & 0 & 0 & A_{66} & B_{66} \\ 0 & 0 & 0 & 0 & B_{66} & D_{66} \end{bmatrix} \begin{bmatrix} \xi_{xx} \\ \kappa_{xx} \\ \xi_{yy} \\ \kappa_{yy} \\ \xi_{xy} \\ 2\kappa_{xy} \end{bmatrix} = \begin{bmatrix} N_1 \\ M_1 \\ N_2 \\ M_2 \\ N_6 \\ M_6 \end{bmatrix} \tag{2.7}$$

where, the stiffness expression, A_{ij}, B_{ij}, D_{ij}, and force and moment resultant N_i, M_i, are described in Appendix B.

In the case of cross-ply CFRP laminate, Eq. (2.7) can be approximated to Eq. (2.8) by neglecting the normal strain coupling terms because fiber stiffness, E_1, is much higher than matrix stiffness, E_2. The simplified force/moment balance equations for cross-ply laminate are given by

$$\begin{bmatrix} A_{11} & B_{11} & 0 & 0 & 0 & 0 \\ B_{11} & D_{11} & 0 & 0 & 0 & 0 \\ 0 & 0 & A_{22} & B_{22} & 0 & 0 \\ 0 & 0 & B_{22} & D_{22} & 0 & 0 \\ 0 & 0 & 0 & 0 & A_{66} & B_{66} \\ 0 & 0 & 0 & 0 & B_{66} & D_{66} \end{bmatrix} \begin{bmatrix} \xi_{xx} \\ \kappa_{xx} \\ \xi_{yy} \\ \kappa_{yy} \\ \xi_{xy} \\ 2\kappa_{xy} \end{bmatrix} = \begin{bmatrix} N_1 \\ M_1 \\ N_2 \\ M_2 \\ N_6 \\ M_6 \end{bmatrix} \tag{2.8}$$

Reduced stain field in Eq. (2.6) can be reduced further as the side length of the laminate goes to infinite because the deformed shape yield to a perfect cylinder, i.e. one of κ_{xx} or κ_{yy} vanishes. As a result, the number of variable is reduced to five, ξ_{xx}, ξ_{yy}, ξ_{xy}, κ_{xy}, and either of κ_{xx} or κ_{yy}. The simplified strain field for

cross-ply laminate with infinite side length yield to

$$E=\begin{cases}\begin{bmatrix}\xi_{xx}\\ \xi_{yy}\\ \xi_{xy}\end{bmatrix}-\begin{bmatrix}\kappa_1-\kappa_{xx}^{initial}\\ -\kappa_{yy}^{initial}\\ 2\kappa_{xy}^{initial}\end{bmatrix}z & \text{for Mode 1}\\ \begin{bmatrix}\xi_{xx}\\ \xi_{yy}\\ \xi_{xy}\end{bmatrix}-\begin{bmatrix}-\kappa_{xx}^{initial}\\ \kappa_2-\kappa_{yy}^{initial}\\ 2\kappa_{xy}^{initial}\end{bmatrix}z & \text{for Mode 2}\end{cases} \tag{2.9}$$

If the laminate shows bistability, either one of normal moment balance equation cannot be satisfied because the deformed shape is cylinder. As a result, explicit approximation equation for final curvature and constant strains for each stable states are derived and expressed by

$$\begin{bmatrix}A_{11}&B_{11}&0&0&0\\ B_{11}&D_{11}&0&0&0\\ 0&0&A_{22}&0&0\\ 0&0&0&A_{66}&B_{66}\\ 0&0&0&B_{66}&D_{66}\end{bmatrix}\begin{bmatrix}\xi_{xx}\\ \kappa_1-\kappa_{xx}^{initial}\\ \xi_{yy}\\ \xi_{xy}\\ 2\kappa_{xy}^{initial}\end{bmatrix}+\kappa_{yy}^{initial}\begin{bmatrix}0\\0\\B_{22}\\0\\0\end{bmatrix}=\begin{bmatrix}N_1\\M_1\\N_2\\N_6\\M_6\end{bmatrix}\quad\text{for Mode 1}\left(\kappa_2=0\right)$$

$$\begin{bmatrix}A_{11}&0&0&0&0\\ 0&A_{22}&B_{22}&0&0\\ 0&B_{22}&D_{22}&0&0\\ 0&0&0&A_{66}&B_{66}\\ 0&0&0&B_{66}&D_{66}\end{bmatrix}\begin{bmatrix}\xi_{xx}\\ \xi_{yy}\\ \kappa_2-\kappa_{yy}^{initial}\\ \xi_{xy}\\ 2\kappa_{xy}^{initial}\end{bmatrix}+\kappa_{xx}^{initial}\begin{bmatrix}B_{11}\\0\\0\\0\\0\end{bmatrix}=\begin{bmatrix}N_1\\N_2\\M_2\\N_6\\M_6\end{bmatrix}\quad\text{for Mode 2}\left(\kappa_1=0\right) \tag{2.10}$$

Based on this, we can generalize the conclusion of the previous study on the effect of initial curvature to the following statement: final non-zero normal curvature of a bistable CFRP cross-ply laminate cured on a curved tool-plate is the sum of the tool-plate normal curvature and final non-zero normal curvature

of the laminate cured on a flat tool-plate. As a result, initial curvature effect to the final curvature with misalignment angle can be summarized to

$$\begin{array}{lll} \text{Mode 1:} & \kappa_1 = \kappa_{flat} + \kappa_{tool}\cos^2\varphi & \kappa_2 = 0 \\ \text{Mode 2:} & \kappa_1 = 0 & \kappa_2 = -\kappa_{flat} + \kappa_{tool}\sin^2\varphi \end{array} \tag{2.11}$$

As a result, a manufacturer of bistable CFRP laminate can easily tailor the final curvature of a bistable CFRP cross-ply laminate if he or she knows the final non-zero normal curvature of the laminate when cured on a flat tool-plate, κ_{flat}.

2.3 Numerical simulation and verification

2.3.1 Numerical simulation

In order to verify the proposed strain field described in the previous section, numerical simulations for CFRP cross-ply laminate with initial curvature are performed. CFRP from HANKUK CARBON CO. LTD. was used for bitable CFRP cross-ply laminate; the material properties are listed in Table 2.1. Final curvature of a bistable CFRP cross-ply laminate with and without misalignment angle as a function of side length change is illustrated in Figure 2.3(a) and (b). The final curvatures of both stable states are changed when an initial curvature with misalignment angle is induced while only one final curvature of stable state is changed when misalignment angle is zero.

Figure 2.4 shows the final curvature changes in bistable CFRP cross-ply

laminates when the side lengths of the laminates were fixed to 150 mm x 150 mm and the radius of curvature of the tool-plate is 200 mm. It shows that Eq. (2.11) is valid, i.e. the final curvature change is proportional to the tool plate non-zero curvature when the misalignment angle is fixed.

2.3.2 Experiments

To validate the Eq. (2.6), principal curvature direction is aligned with fiber direction although initial twisting curvature is applied, with experiment, bistable CFRP cross-ply laminates are cured with two different misalignment angles, 0° and 45°. The shape of the composites before curing was perfectly square with a length of 150 mm. Two square CFRP plies were perfectly aligned [0°/90°] and cured at 170˚C with a curing time of two hours and bagging pressure of 1 atm. Figure 2.5 shows that twisting curvature and in-plane shear strain are negligibly small and the equilibrium shape is very close to cylindrical even with the misalignment angle.

To validate Eq. (2.11), the change of the final curvatures of two stable states as a function of misalignment angle was measured experimentally. The radius of curvature of the tool-plate was fixed at 300mm. Three different misalignment angles, 15°, 30°, and 45° were tested for the lay-up sequences [0°/90°] and [90°/0°], and three specimens were cured for each misalignment angle. The final curvatures of the specimens as a function of misalignment angle and their scattering are given in Figure 2.6.

Tool plate curvature is measured based on the assumption that the final curvature of the laminate is almost constant. Curvature equation as a function of chord length and height of the laminate is given by

$$\kappa = \frac{8d}{C^2 + 4d^2} \tag{2.12}$$

where, C is the length of chord and d is the height of laminate after curing.

The model predictions agree well with the experimental measurements. It should be noted the [90°/0°] lay-up sequence with misalignment angles 15°, 30° and 45° is equivalent to the [0°/90°] lay-up sequence with misalignment angles 75°, 60° and 45°, respectively.

2.3.3 Design Guideline

For the designer, schematic diagram of the procedure to determine the misalignment angle and initial tool plate curvature in order to meet the required final laminate curvatures κ_1 and κ_2 is presented in Figure 2.7. The key equations in Figure 2.7 are given in Eq. (2.13) which is the rearrangement of Eq. (2.11). These equations are useful for designing the final curvatures of a bistable CFRP cross-ply laminates using misalignment angles. Misalignment angle as a function of final curvatures κ_1, κ_2 and misalignment angle φ is given by

$$\varphi = \tan^{-1}\sqrt{\frac{\kappa_2 + \kappa_{flat}}{\kappa_1 - \kappa_{flat}}}$$
$$\kappa_{tool} = \frac{\kappa_1 - \kappa_{flat}}{\cos^2\varphi} = \frac{\kappa_2 + \kappa_{flat}}{\sin^2\varphi} \tag{2.13}$$

Based on Eq. (2.13) and Figure 2.7, the tool curvature and initial angle between the fiber direction of the laminate and x-axis are predicted for the desired final curvature of a bistable CFRP cross-ply laminate. These can be calculated systematically. For example, suppose that the design requirements for the final curvatures of a bistable CFRP cross-ply laminate are 24 (1/m) in the x-direction, κ1, and -15 (1/m) in the y-direction, κ2, and the magnitude of the final curvature of the bistable CFRP cross-ply laminate without initial curvature, κ, is 18 (1/m); The final curvature of the bistable CFRP cross-ply laminate without initial curvature can be obtained by either simulation or the experiment. In this case, we can calculate the misalignment angle and tool plate curvature in an explicit manner by following the procedure shown in Figure 2.7. First, the misalignment angle is 35.2644°, from the first row of the Eq. (2.13). Next, the amount the tool-plate curvature is 9 (1/m) based on the second row of Eq. (2.13). Thus, we can satisfy the design requirements for the final curvatures of a bistable CFRP laminate with a cylindrical tool-plate alone.

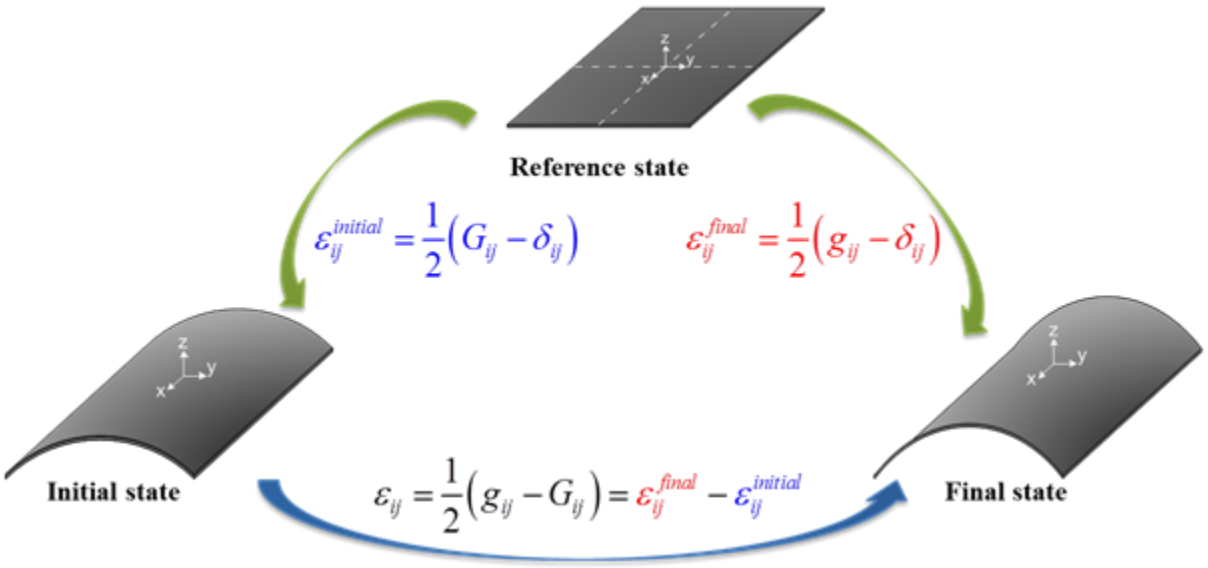

Figure 2.1 Reference state definitions to describe initial and final strain field.

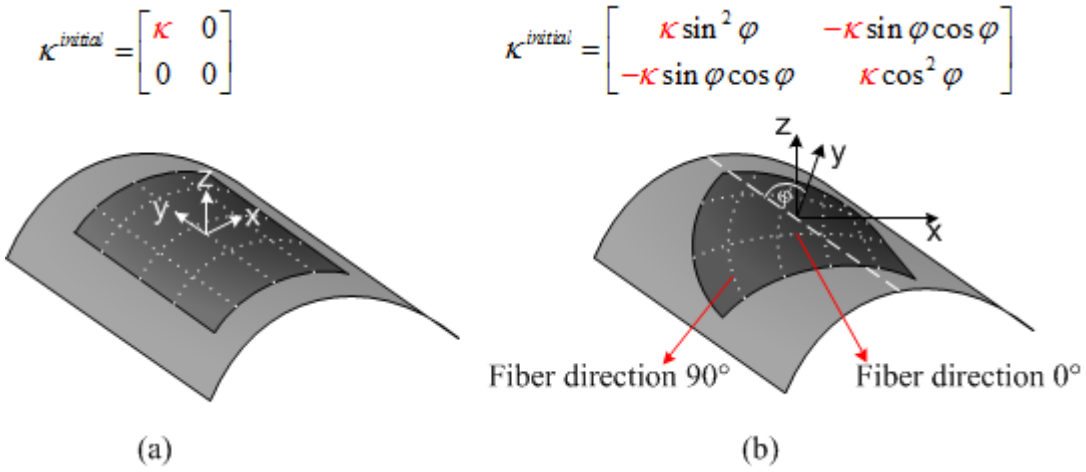

Figure 2.2 Initial curvature change by misalignment :

(a) Fiber direction coincides with the principal curvature direction of the tool-plate

(b) Fiber direction is misaligned with the principal curvature direction of the tool-plate

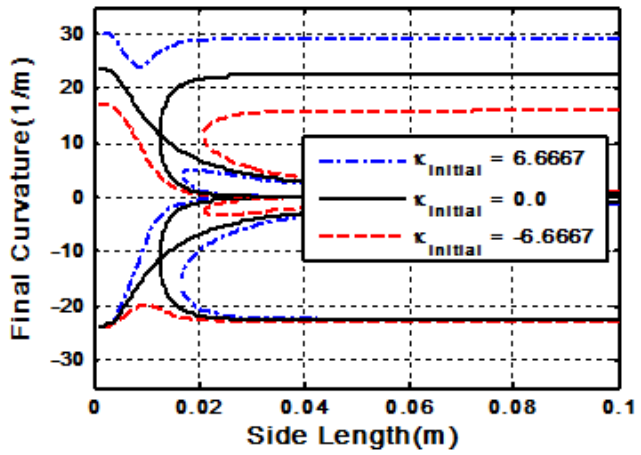

(a)

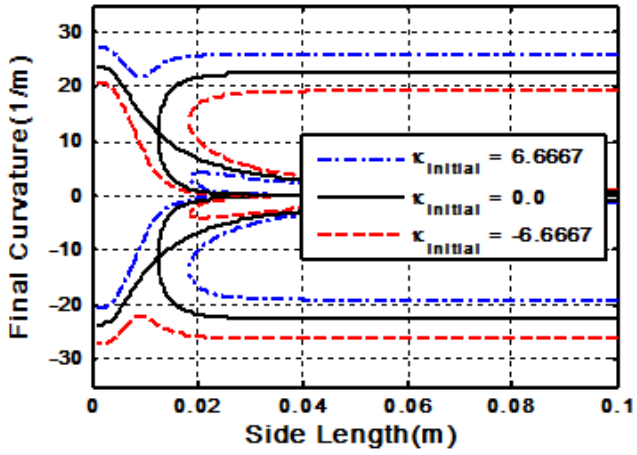

(b)

Figure 2.3 Final curvature of a bistable CFRP cross-ply laminate as a function of side length change

(a) The fiber direction coincides with the principal curvature direction of tool-plate

(b) The fiber direction is misaligned with the principal curvature direction of the tool-plate (45°)

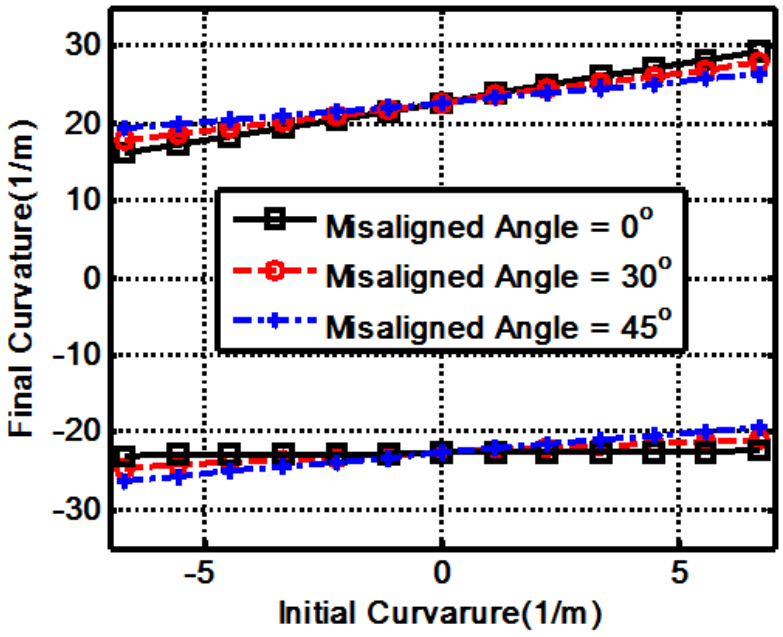

Figure 2.4 Predicted final curvature of a bistable CFRP cross-ply laminate as a function of misaligned angle ($R^{initial}$ =150 mm)

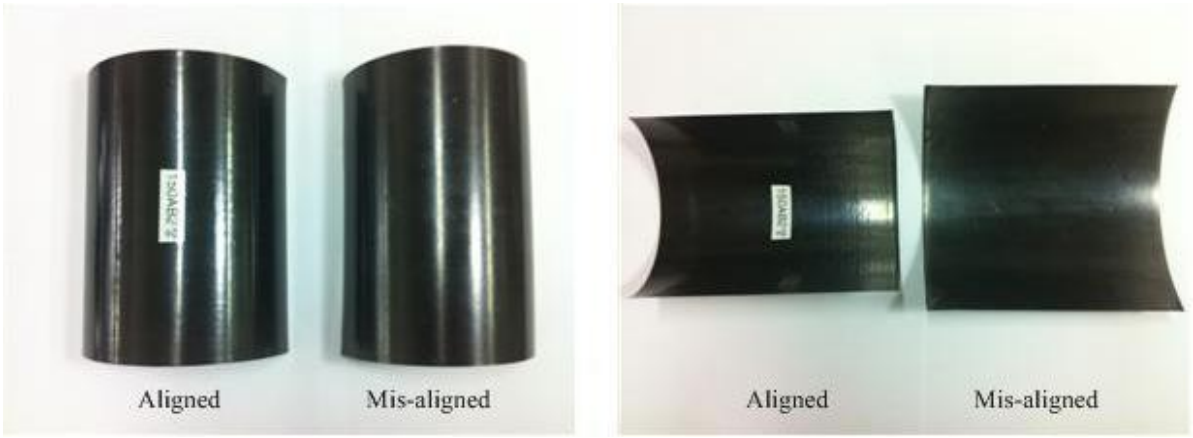

Figure 2.5 Deformation behavior of bistable composite with and without misalignment angle ($R^{initial}$ =200mm, φ=45°)

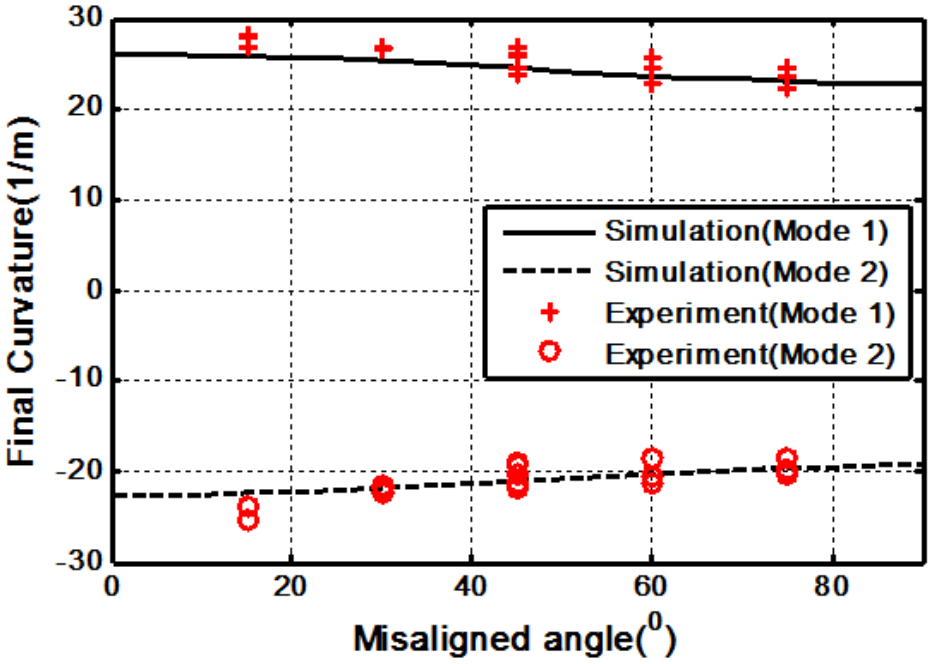

Figure 2.6 Final curvature changes as a function of misalignment angle ($R^{initial}$ =300mm)

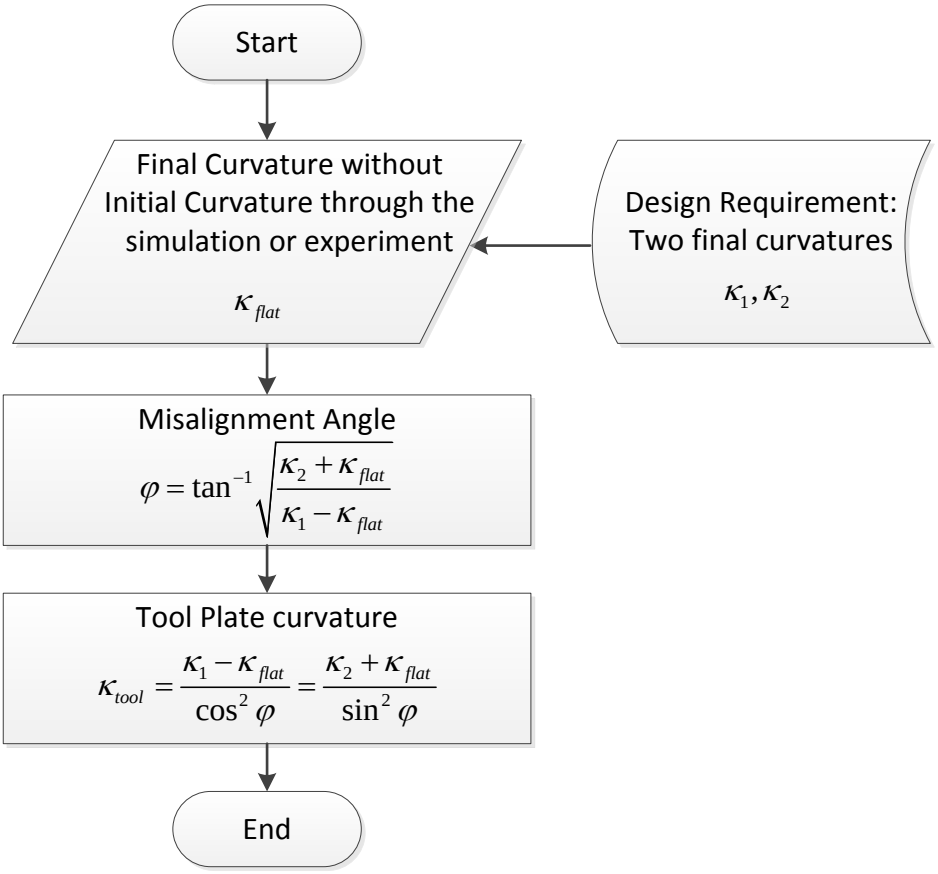

Figure 2.7 Schematic diagram of the procedure to determine the misalignment angle and initial tool plate curvature in order to meet the required final laminate curvatures κ_1 and κ_2.

Table 2.1 Material Properties of CFRP

Quantity		Unit	Value
Axial tensile modulus	E_1	GPa	160
Transverse tensile modulus	E_2	GPa	12
Shear modulus	G_{12}	GPa	8
Major Poisson's ratio			0.3
Mass per unit length		g/cm^3	800
Density		g/mm^2	1.8
Carbon fiber weight		g/mm^2	54
Resin weight		g/mm^2	38
Scrim weight		g/mm^2	34
Thickness		mm	0.085
Thermal expansion coefficient parallel to fiber direction	α_1	$°C^{-1}$	0.19×10^{-6}
Thermal expansion coefficient perpendicular to fiber direction	α_2	$°C^{-1}$	0.32×10^{-4}
Temperature change	ΔT	°C	–145

Chapter 3

Effect of initial curvature on the snap-through load

3.1 Introduction

In this chapter, the effect of the initial curvature of a tool plate on the snap-through load of square cross-ply bistable composites is analyzed. The snap-through load is a function of the cured curvature and residual moment. In the curing process, both these physical quantities are affected by the initial tool-plate curvature. As a result, the snap-through load can also be changed by adjusting the initial tool-plate curvature. Then, for evaluating its effect on the snap-through load, a snap-through process is simulated by minimizing the total potential energy of the bistable composites through the Rayleigh–Ritz approximation method. The simulation results show that the snap-through load changes linearly with the initial tool-plate curvature. The simulation results are compared with those obtained experimentally and by a finite element analysis (FEA) in order to verify the pre-identified effect of the initial tool-plate curvature.

3.2 Snap-through and its driving mechanism

Two stable shapes of the square cross-ply bistable composite are defined as Mode 1 and Mode 2 depending on the orientation of the curvature of the bistable composite with respect to the initial tool-plate curvature, as illustrated in Figure 1.1. Specifically, Mode 1 is defined as a cylindrical shape in which the dominant curvature is parallel to the initial tool-plate curvature, i.e., the x-directional curvature κ_{xx}. On the other hand, Mode 2 is defined as a cylindrical shape in which the dominant curvature is perpendicular to the initial tool-plate curvature, i.e., the y-directional curvature κ_{yy}.

The snap-through process is separately categorized into a snap-forth process and a snap-back process depending on the sequence of mode change. Specifically, snap-forth refers to snap-through from Mode 1 to Mode 2, and snap-back refers to snap-through from Mode 2 to Mode 1, as illustrated in Figure 1.2.

In order to induce snap-through, a mechanical load should be applied with the aim of unrolling the bistable composite. For example, if an x-directional moment is applied to the bistable composite in Mode 1, it will just unroll while maintaining the x-directionally curved cylindrical shape at the beginning of deformation. However, when the dominant curvature of the bistable composite reaches a certain x-directional deformation curvature (henceforth referred to as the “snap-forth starting curvature”), the composite starts transforming from

Mode 1 to Mode 2 (i.e., snap-forth) by itself. In other words, at the snap-forth starting curvature, the direction of the dominant curvature starts changing from the x-direction to the y-direction, which is perpendicular to the direction of the external moment and direction of the dominant curvature.

In order to explain the above phenomenon, we make the following two assumptions:

1. A driving mechanism exists that is acting perpendicular to the direction of the dominant curvature of each mode.

2. The snap-through starting curvature is the minimum or critical curvature at which the driving mechanism is sustained.

In fact, in the case of Mode 1, the internal residual moment is induced in the y-direction, which is perpendicular to the direction of the dominant curvature. This y-directional internal residual moment (${}_{Mode1}M_y^{residual}$) is distributed along the x-directional edge, as shown in Figure 3.1. The internal residual moment becomes zero at the free edge ($y = \pm L/2$) in order to satisfy the stress-free boundary condition. However, it rapidly recovers to a constant value when it approaches

the interior region of the cylindrical panel. In this study, we focus only on the constant internal residual moment away from the free edges.

The constant internal residual moment (hereafter simply called “residual moment”) acts in a direction perpendicular to the direction of the dominant curvature of each mode. Therefore, this residual moment might be one of the important factors that trigger the snap-through mechanism. Consequently, the snap-forth starting curvature mentioned in the second assumption above can be reinterpreted as being the minimum curvature at which the residual moment can be sustained. According to the second assumption, the snap-forth load would also be affected by the change in the snap-forth starting curvature with a change in the y-directional residual moment. Contrary to the case of snap-forth, in the case of snap-back, the snap-back load would be affected by the x-directional residual moment.

Therefore, the residual moment, in addition to the cured curvature, is an important factor in the design of the snap-through load. For example, in the prediction of the snap-forth load, both the x-directional cured curvature and the y-directional residual moment should be considered. Similarly, in the prediction of the snap-back load, both the y-directional cured curvature and the x-directional residual moment should be considered.

For these reasons, changes in the residual moment and cured curvature with the initial tool-plate curvature need to be examined prior to predicting the change in

the snap-through load induced by the initial tool-plate curvature. First, the cured curvature, as well as the mid-plane strain fields, can be easily estimated by using the explicit model of Ryu et al. [41]. Next, the residual moment can be estimated from the definition of moment resultant in the classical laminate theory. The material properties and stacking sequence of the laminated composites were adopted from the study of Ryu et al. [41].

As an example, the cured curvature and residual moment were estimated under increasing x-directional initial tool-plate curvature. When the bistable composite is in Mode 1, the x-directional initial tool-plate curvature affects only the x-directional cured curvature of Mode 1, as shown in Figure 3.2(a). However, when the bistable composite is in Mode 2, the x-directional initial tool-plate curvature affects only the x-directional residual moment of Mode 2, as shown in Figure 3.2 (b). In addition, both quantities (i.e. the x-directional cured curvature of Mode 1 and the x-directional residual moment of Mode 2) are increased with increasing initial curvature.

If the two abovementioned assumptions are correct and when the abovementioned known relation between the cured curvature and the x-directional initial tool-plate curvature is considered, application of the x-directional initial tool-plate curvature will have the following effects.

1. In the case of snap-forth, the snap-through starting curvature should not be changed, because the y-directional residual moment of Mode 1, which is the driving mechanism for the snap-forth process, is not affected by the x-directional initial tool-plate curvature.

2. In the case of snap-back, the snap-through starting curvature should be increased because the x-directional residual moment of Mode 2, which is the driving mechanism for the snap-back process, increases with increasing x-directional initial tool-plate curvature.

Considering the two assumptions and the known relation between the cured curvature and the x-directional initial tool-plate curvature, the snap-forth load should be increased with increasing the x-directional initial tool-plate curvature. In contrast to the snap-forth load, the snap-back load should be decreased with increasing the x-directional initial tool-plate curvature.

3.3 Snap-through of bistable composites subjected to line-edge moment

In this section, we estimate the snap-forth and snap-back loads (moments) by the Rayleigh–Ritz approximation method to determine the relationship between the snap-through load and the initial tool-plate curvature

3.3.1 Simple analytical model

The simple analytical model is derived by minimizing the total potential energy including a moment equilibrium condition. The minimization is performed using the Rayleigh–Ritz approximation method as follows:

$$\delta\Pi^{*} = \delta\Pi + \delta\left\{\Lambda\left(\int_{-\frac{L}{2}}^{\frac{L}{2}} M^{external}\,dl - \int_{-\frac{L}{2}}^{\frac{L}{2}} M^{internal}\,dl\right)\right\} \tag{3.1}$$

where $\delta\Pi^{*}$ is the first variation of the total potential energy and $\delta\Pi$ is the first variation of the strain energy of the bistable composite. The difference between the internal moment $M_{internal}$ and the external moment $M_{external}$ acts as the moment equilibrium constraint that conjugates to the Lagrange multiplier Λ.

3.3.2 Strain energy of bistable composites

Assuming a plane stress state, the strain energy of unsymmetric cross-ply laminated composites with initial tool-plate curvature is expressed as

$$\Pi = \sum_{i=1}^{n}\int_{-\frac{L}{2}}^{\frac{L}{2}}\int_{\frac{L}{2}}^{\frac{L}{2}}\int_{z_i^{low}}^{z_i^{up}} \frac{1}{2}\bar{Q}_{11}^{i}\varepsilon_{xx}^{2} + \frac{1}{2}\bar{Q}_{22}^{i}\varepsilon_{yy}^{2} + \bar{Q}_{12}^{i}\varepsilon_{xx}\varepsilon_{yy} + \frac{1}{2}\bar{Q}_{66}^{i}\gamma_{xy}^{2}\,dzdxdy \tag{3.2}$$

where $\bar{Q}^i_{\alpha\beta}$ is the transformed plane-stress reduced stiffness of the i-th layer; L is the side length of the composites; and z_i^{up} and z_i^{low} denote the positions of the upper surface and lower surface, respectively, corresponding to the i-th layer. The elastic strains $\varepsilon_{xx}, \varepsilon_{yy}, \gamma_{xy}$ are given by the difference between the total strains and the inelastic strains, as expressed in Eq. (3.3):

$$\begin{Bmatrix} \varepsilon_{xx} \\ \varepsilon_{xx} \\ \gamma_{xy} \end{Bmatrix} = \begin{Bmatrix} \varepsilon_{xx}^{total} \\ \varepsilon_{xx}^{total} \\ \gamma_{xy}^{total} \end{Bmatrix} - \begin{Bmatrix} \varepsilon_{xx}^{in-elastic} \\ \varepsilon_{xx}^{in-elastic} \\ \gamma_{xy}^{in-elastic} \end{Bmatrix} = \left\{ \begin{bmatrix} \xi_{xx} + \lambda_{xx} y^2 \\ \xi_{yy} + \lambda_{yy} x^2 \\ \left(\kappa_{xx}\kappa_{yy} + 2\lambda_{xx} + 2\lambda_{yy}\right) xy \end{bmatrix} + \begin{bmatrix} -\kappa_{xx} \\ -\kappa_{yy} \\ 0 \end{bmatrix} z \right\} - \left\{ \begin{bmatrix} \alpha_{xx}\Delta T \\ \alpha_{yy}\Delta T \\ \alpha_{xy}\Delta T \end{bmatrix} + \begin{bmatrix} \kappa_{xx}^{initial} \\ 0 \\ 0 \end{bmatrix} z \right\} \quad (3.3)$$

Inelastic strains are defined as the sum of the thermal strains and the strain induced by the initial tool-plate curvature. Thermal strains are defined as the product of the thermal coefficients $\alpha_{xx}, \alpha_{yy}, \alpha_{xy}$ and the change in temperature, ΔT. The tool-plate-induced strains are expressed as the product of the initial tool-plate curvature $\kappa_{xx}^{initial}$ and the distance from the mid-plane axis, z. The total strains $\varepsilon_{xx}^{total}, \varepsilon_{yy}^{total}, \gamma_{xy}^{total}$ are represented by a quadratic form that has six undetermined Ritz coefficients: the constant mid-plane strain terms ξ_{xx}, ξ_{yy}, the quadratic mid-plane strain terms $\lambda_{xx}, \lambda_{yy}$, and the constant curvatures κ_{xx}, κ_{yy} of the bistable composite. The total strains are derived by making three assumptions—assumption of an infinitesimal strain, assumption of a Kirchhoff–Love thin plate/shell, and assumption of a constant curvature shape [41].

3.3.3 Moment equilibrium

The internal and external moments must be compared to determine whether or not the moment equilibrium condition has been satisfied. For this comparison, the internal moment should be calculated by considering the neutral axis.

Generally, the moment resultant is defined on the basis of the mid-plane axis in the classical laminate theory. However, in the case of unsymmetric cross-ply laminated composites, the mid-plane axis does not coincide with the neutral axis. Therefore, the internal moment resultant should be recalculated on the basis of the neutral axis.

In the case of snap-forth, since the external moment is applied along the edge (i.e., $x = \pm L/2$), the corresponding internal moment is recalculated as follows:

$$\int_{-\frac{L}{2}}^{\frac{L}{2}} M_x^{internal}\, dy = \left(\sum_{i=1}^{n} \int_{-\frac{L}{2}}^{\frac{L}{2}} \int_{z_i^{btm}}^{z_i^{top}} \left(Q_{11}^i \varepsilon_{11} + Q_{12}^i \varepsilon_{22} \right) (z - d)\, dz dy \right) \Bigg|_{x=\pm\frac{L}{2}} \tag{3.4}$$

where d is the distance from the mid-plane axis to the neutral axis, as illustrated in Figure 3.3.

Further, in the case of snap-back, since the external moment is applied to the edge (i.e., $y = \pm L/2$), the corresponding internal moment is recalculated as

$$\int_{-\frac{L}{2}}^{\frac{L}{2}} M_y^{internal}\, dx = \left(\sum_{i=1}^{n} \int_{-\frac{L}{2}}^{\frac{L}{2}} \int_{z_i^{btm}}^{z_i^{top}} \left(Q_{21}^i \varepsilon_{11} + Q_{22}^i \varepsilon_{22} \right) (z + d)\, dz dx \right) \Bigg|_{y=\pm\frac{L}{2}} \tag{3.5}$$

3.3.4 Minimization of total potential energy

The first variation of the total potential energy, $\delta\Pi^*$, should be equal to zero to ensure the existence of a solution. The requirement for the existence of a solution is given as follows:

$$\delta\Pi^* = \left(\frac{\partial\Pi^*}{\partial\xi_{xx}}\right)\delta\xi_{xx} + \left(\frac{\partial\Pi^*}{\partial\xi_{yy}}\right)\delta\xi_{yy} + \left(\frac{\partial\Pi^*}{\partial\lambda_{xx}}\right)\delta\lambda_{xx} + \left(\frac{\partial\Pi^*}{\partial\lambda_{yy}}\right)\delta\lambda_{yy} + \left(\frac{\partial\Pi^*}{\partial\kappa_{xx}}\right)\delta\kappa_{xx} + \left(\frac{\partial\Pi^*}{\partial\kappa_{yy}}\right)\delta\kappa_{yy} + \left(\frac{\partial\Pi^*}{\partial\Lambda}\right)\delta\Lambda = 0 \qquad (3.6)$$

Eq. (3.6) is a compilation of nonlinear algebraic equations that have seven unknowns: $\xi_{xx}, \xi_{yy}, \lambda_{xx}, \lambda_{yy}, \kappa_{xx}, \kappa_{yy}, \zeta$. In order to solve these nonlinear algebraic equations, the Newton–Raphson iterative method is used. The cylindrical shape of Mode 1 for snap-forth and the cylindrical shape of Mode 2 for snap-back is assumed as an initial solution. In each subsequent step (i.e., loading step), an initial solution uses the calculation result obtained in the previous step.

3.3.5 Analysis result

Cross-ply [0/90] bistable composites with x-directional initial tool-plate curvatures of 0, 4, 5, 6.66, and 8.33 m^{-1} are considered in this study. Properties of the material of the lamina, i.e., carbon fiber prepreg, are summarized in Table 3.1; these properties are also considered in the experiments described later in the paper. The lamina material used in the study is CU 0503 carbon fiber reinforced plastic (Hankuk Carbon). The prepreg is cut into squares with a side length of 150 *mm*.

In the snap-through analysis, the moment is applied along the edge (i.e., $x = \pm L/2$ for snap-forth and $y = \pm L/2$ for snap-back), as illustrated in Figure 3.4. During the application of the moment, the deformation curvatures are estimated at regular intervals, as shown in Figure 3.5. The snap-through moment is the value at which the strain energy of the bistable composites attains a maximum.

As is clear from the results of the snap-through analysis shown in Figure 3.5, the snap-forth moment increases linearly with the initial tool-plate curvature. However, the snap-back moment decreases linearly with increasing initial tool-plate curvature.

The snap-through moment can be predicted easily but quite accurately if the cured curvature and snap-through starting curvature are both known. This is because the bending rigidity of the bistable composite is nearly constant before the snap-through process starts but it decreases rapidly after snap-through occurs. As a result, the snap-through moment can be approximated as a product of the bending rigidity and the difference between the cured curvature and the snap-through starting curvature. Hence, the snap-through moment is closely related to the cured curvature and the snap-through starting curvature.

First, in the case of snap-forth, the cured curvatures of Mode 1 (i.e., the starting deformation curvatures of the linear region of the $M_x - {}_1\kappa_{xx}$ curve) increase linearly with the initial tool-plate curvature. However, the snap-forth starting curvatures (i.e., the ending deformation curvatures of the linear region

of the $M_x - {}_1\kappa_{xx}$ curve, which are indicated by the dots in Figure 3.5(a)) are identical to each other regardless of the initial tool-plate curvature. For this reason, the difference between the cured curvature and the snap-forth starting curvature increases linearly with the initial tool-plate curvature. As a result, the snap-forth moment also increases linearly with increasing initial tool-plate curvature. The variation trend of the snap-forth moment with a change in the initial tool-plate curvature agrees well with the predicted result as presented earlier.

Additionally, the relation between the y-directional residual moment ${}_{Mode1}m_{yy}^{Residual}$ and the snap-forth starting curvature supports the second assumption. As mentioned earlier, the y-directional residual-moment and the snap-forth starting curvature remain constant regardless of the initial tool-plate curvature. In other words, there is one-to-one correspondence between the y-directional residual moment and the snap-forth starting curvature, as expected earlier.

Second, in the case of snap-back, the cured curvatures of Mode 2 (i.e., the starting deformation curvatures of the linear region of the $M_y - {}_2\kappa_{yy}$ curve) change very slightly with the initial tool-plate curvature. However, the snap-back starting curvatures (i.e., the ending deformation curvatures of the linear region of the $M_y - {}_2\kappa_{yy}$ curve, which are indicated by the dots in Figure 3.5(b)) decrease linearly with increasing initial tool-plate curvature. For this reason, the difference between the cured curvature and the snap-back starting curvature also

decreases linearly with increasing initial tool-plate curvature. As a result, the snap-back moment also decreases linearly with increasing initial tool-plate curvature. The variation trend of the snap-back moment with a change in the initial tool-plate curvature agrees well with the predicted result as presented earlier.

Additionally, the relation between the x-directional residual moment ${}_{Mode\,2}m_{xx}^{Residual}$ and the snap-back starting curvature supports the second assumption. As mentioned earlier, the x-directional residual-moment and the snap-back starting curvature change with changing initial tool-plate curvature. Therefore, one-to-one correspondence also exists between the y-directional residual moment and the snap-forth starting curvature. The interpretation of this result is that the increased residual moment makes it difficult to sustain a cylindrical shape with a relatively small curvature. For this reason, the snap-back of the bistable composite with an initial tool-plate curvature starts earlier than that of the bistable composite with a zero initial tool-plate curvature.

3.4 Verification of pre-identified effect of initial curvature

3.4.1 FE analysis of snap-through moment of bistable composites

FE analysis was performed for obtaining results that are more accurate and for verifying the analysis results obtained by the present simple analytical model.

Commercial FE software ABAQUS was used for the static analysis of the snap-though induced by an external moment [51]. The selected element was a four-node doubly curved thin shell element (S4). The mesh density was chosen as 20 × 20 elements in consideration of the convergence property and computation time. To reduce the computation time further, one quarter of the entire system was simulated on the basis of the symmetry of this problem [34].

The FE analysis was divided into two main processes—the curing process and the loading process—explained as follows.

1. In the curing process, the evaluation temperature (170 ℃) is reduced to the service temperature (25 ℃), as shown in Figure 3.6(a). Following the curing process, the bistable composite takes the cylindrical stable shape of Mode 1 or that of Mode 2, as illustrated in Figure 3.6(b).

2. In the loading process, a moment is applied to the flat edge of the bistable composite to induce snap-through, as shown in Figure 3.6(b).

1) During the loading process, the strain energy of the bistable composite increases with increasing moment. Snap-through eventually occurs at the maximum strain energy, the moment at which instant is taken as the snap-through moment in this case. After snap-through, the moment is removed to check the stability of the snapped cylindrical shape.

2) Following the relaxation, the moment is reapplied to the flat edge of the snapped bistable composites in the opposite direction to induce snap-through, as illustrated in Figure 3.6(c). After snap-through has occurred, the corresponding moment is also removed.

As shown in Figures 3.7 and 3.8, the results of the FE analysis demonstrate that the snap-forth moment and the snap-back moment respectively increase and decrease linearly with the initial tool-plate curvature, as was the trend in the pre-analysis. The magnitude of the overall snap-through moments in the FE analysis is smaller than those in the pre-analysis. Nonetheless, the effects of the initial tool-plate curvature on the snap-through moment are identical in both the FE analysis and the pre-analysis.

The difference between these two results is attributed to the assumption of a constant curvature in the analytical model. In the case of thin bistable composites, snap-through occurs under complex deformations (e.g., noncylindrical bending or warpage) [52]. However, this assumption cannot represent local complex warpage deformations. For this reason, the snap-through load in the analytical model is overestimated compared to the result obtained by three-dimensional FE Analysis.

3.4.2 Experiment and FE analysis of snap-through vertical load of bistable composites

In the previously presented analyses in this paper, the effect of the initial tool-plate curvature on the snap-through moment was studied. In the practical experiment of this study, a vertical load was considered instead of a distributed edge moment. Then, experiments and FE analysis were performed for evaluating the snap-through load of bistable composites subjected to a vertical load, where an experimentally realizable boundary condition was considered.

The experimental setup is shown in Figure 3.9. An indenter is aligned parallel to the direction of the dominant curvature of the bistable composites. The indenter is fixed to the tensile machine. Therefore, the indenter is movable only in the vertical direction. The bistable composites are placed on two glass plates, which are lubricated by oil to minimize the friction between the edge of the bistable composites and the surface of the glass plate. The two glass plates are placed parallel to each other on the testing table at a constant distance. The distance is kept longer than the width of the indenter to prevent collision between the indenter and the glass plate.

Before the vertical load test, square cross-ply bistable composites with an initial curvature were manufactured. First, two laminae were cut into squares with a side length of 150 *mm*. The lamina with a 0° direction was placed on the tool plate, and its fiber was aligned in a direction parallel to the curvature direction

of the tool plate. The lamina with a 90° direction was placed on the 0° direction lamina and its fiber was aligned in a direction perpendicular to the curvature direction of the tool plate. The cross-ply laminates were packaged in the same way as that done by Ryu et al. [41]. In the curing process, the temperature was elevated from room temperature (25 ℃) to the curing temperature (170 ℃). Then, the packaged laminates were cured in a curing oven for 2 *h*. The curing pressure was maintained at 1 *atm* by an external vacuum pump during the curing cycle.

The vertical load test was performed by the following procedure. First, the indenter and the bistable composites were separated from each other as shown in Figure 3.9(a). As the indenter moved downward, its bottom surface came into contact with the top surface of the bistable composites, as shown in Figure 3.9(b). At this instant, the vertical load was induced by surface-to-surface contact; following this, the deformation of the bistable composites was initiated (Figures 3.9 (c) and (d)). The vertical load was applied quasi-statically with downward motion of the indenter until snap-through occurred. The vertical load at which snap-through occurs is defined as the snap-through vertical load.

The FE analysis was performed in the same way as the vertical load test. The FE models used for FE analysis consisted of the bistable composites, a rigid indenter, and a rigid plate part, as illustrated in Figure 3.10. The four-node doubly curved thin shell element (S4) was selected for the simulation of the snap-through of the

bistable composites. The mesh density for the bistable composites was chosen as 1600 elements. In order to minimize mesh dependency of the snap-through vertical load, the analytical rigid surface in ABAQUS [51], which does not require meshes, was employed for generating the rigid components except for the bistable composites (i.e., the rigid indenter and the rigid plate part).

3.4.3 Comparison between experimental and FEA result

For the snap-through experiments, five different initial tool-plate curvatures—0, ±5, and ±6.667 m^{-1}—were considered. For each of these initial curvatures, three bistable composite specimens were manufactured. The vertical load tests were performed six times for each bistable composite specimen: three times for snap-forth and three times for snap-back.

From the experimental and FEA results presented in Figure 3.11, we found that the snap-through vertical loads were proportional to the initial tool-plate curvatures. As shown in Figure 3.8, the line moment acting on the square cross-ply bistable composite specimens also showed this linearity with the value of the initial tool-plate curvature. Further, as shown in Figure 3.11, the snap-through vertical load obtained by FE analysis was in excellent agreement with that obtained experimentally.

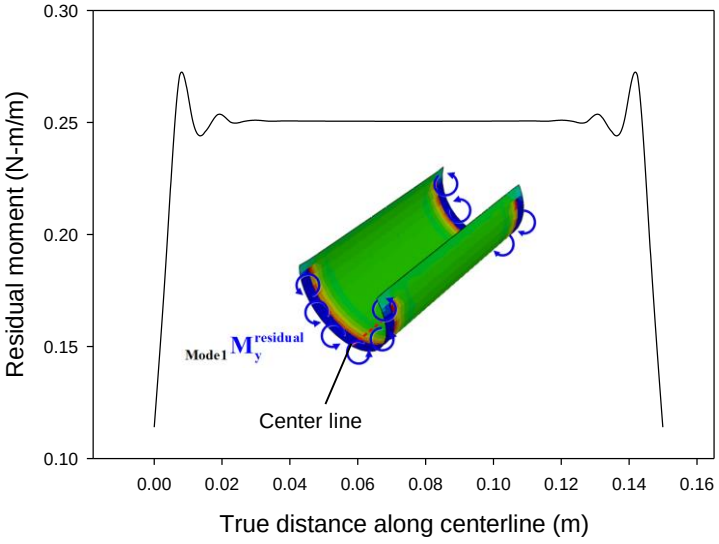

Figure 3.1 Distribution of internal residual moment along centerline of bistable composites

(FEA result of unsymmetrically laminated cross-ply bistable composite).

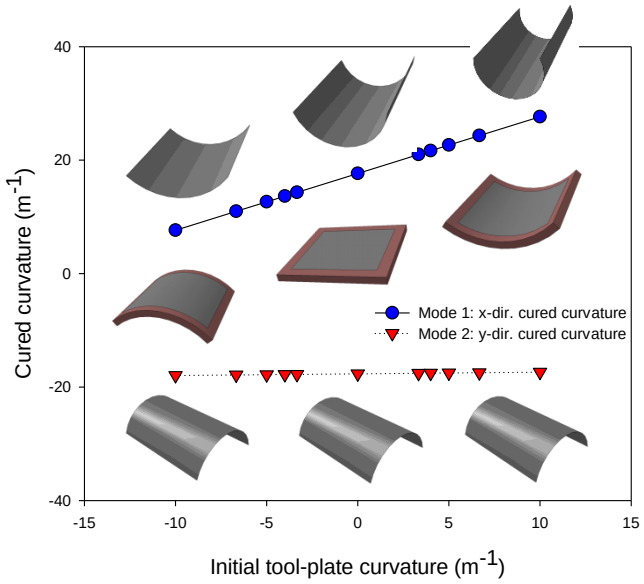

(a)

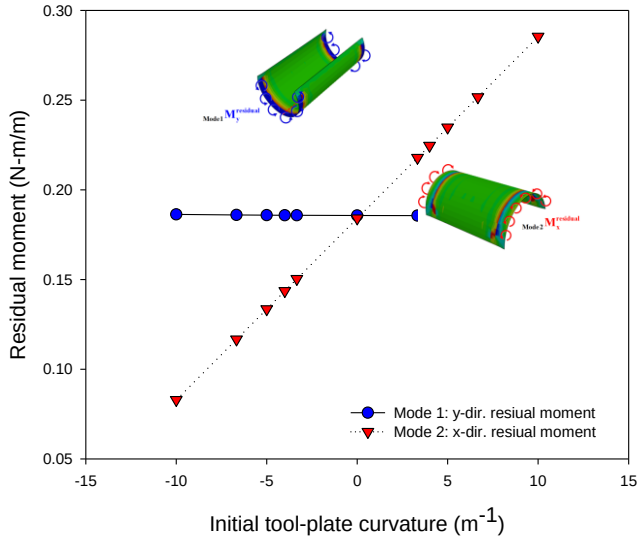

(b)

Figure 3.2 Cured curvature and residual moment as a function of x-directional initial tool-plate curvature (analysis results).

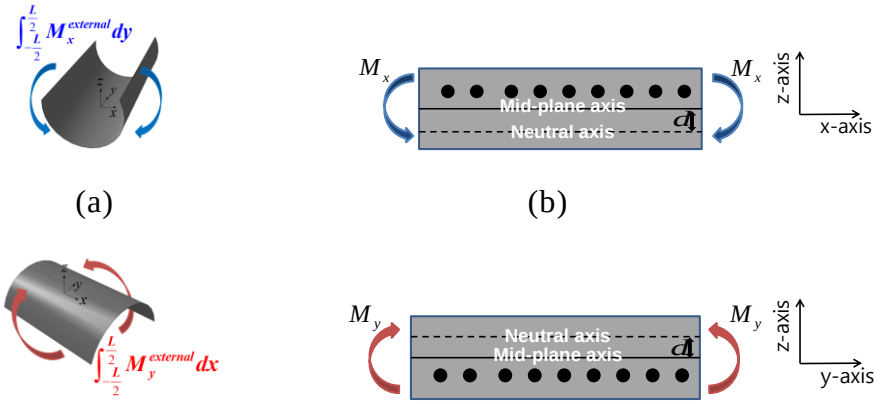

Figure 3.3 Schematics of loading conditions and positions of neutral axes: (a), (b) snap-forth and (c), (d) snap-back.

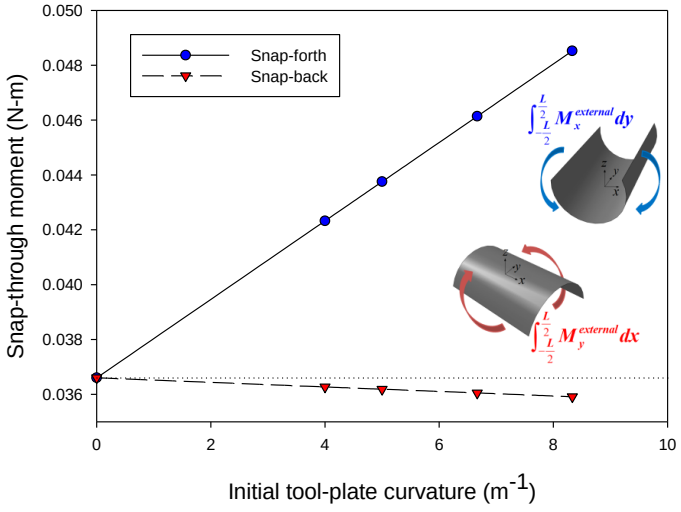

Figure 3.4 Change in snap-through moment with initial tool-plate curvature (analysis results).

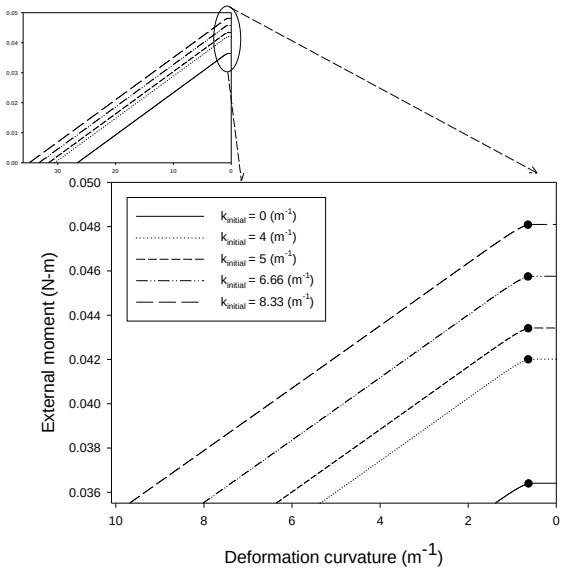

(a)

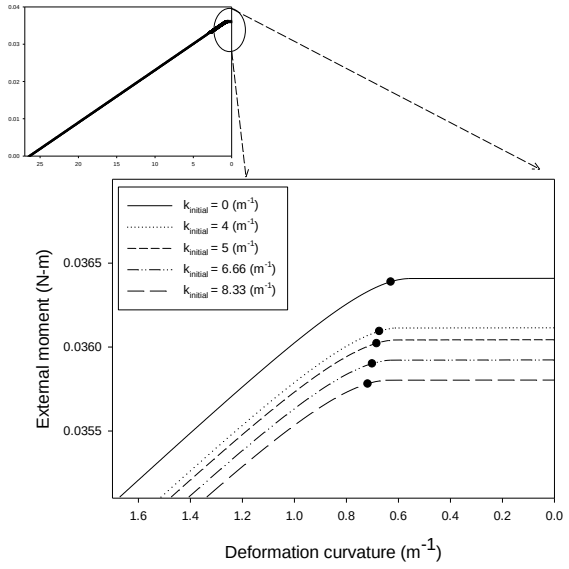

(b)

Figure 3.5 Curve of moment vs. deformation curvature for each initial tool-plate curvature (analysis results): (a) snap-forth and (b) snap-back.

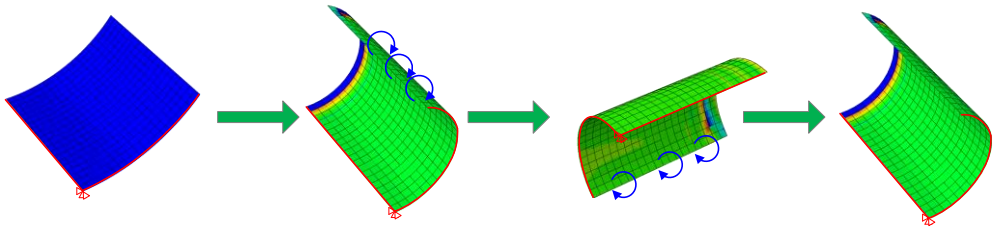

(a) (b) (c) (d)

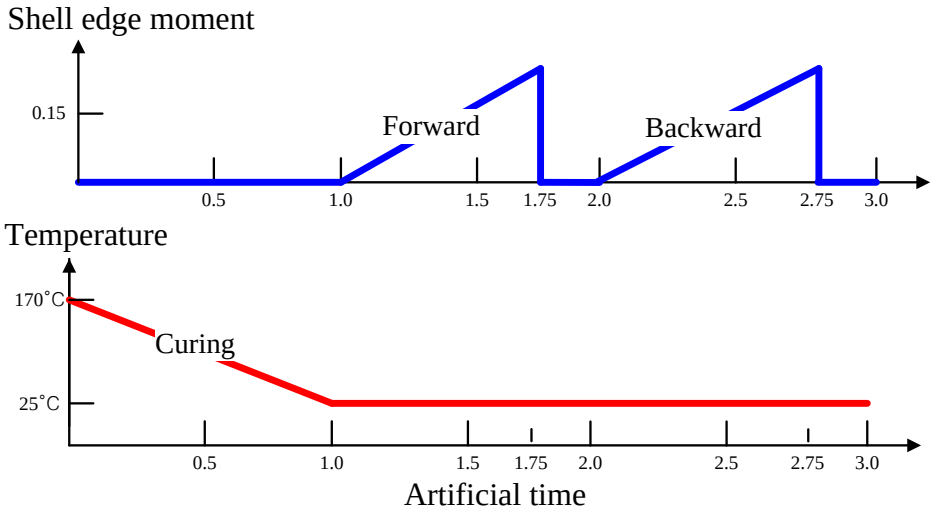

(e)

Figure 3.6 FE analysis of snap-through of bistable composite subjected to a moment: (a) before curing process, (b) after curing process and snap-forth, (c) after snap-forth and snap-back, (d) after snap-back, and (e) loading history of FE analysis.

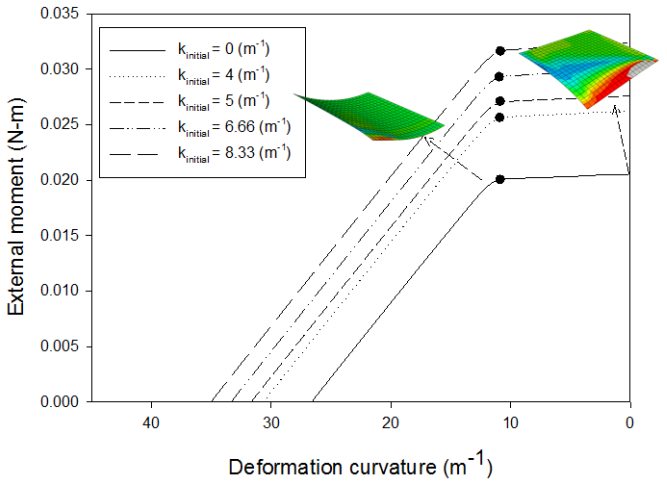

(a)

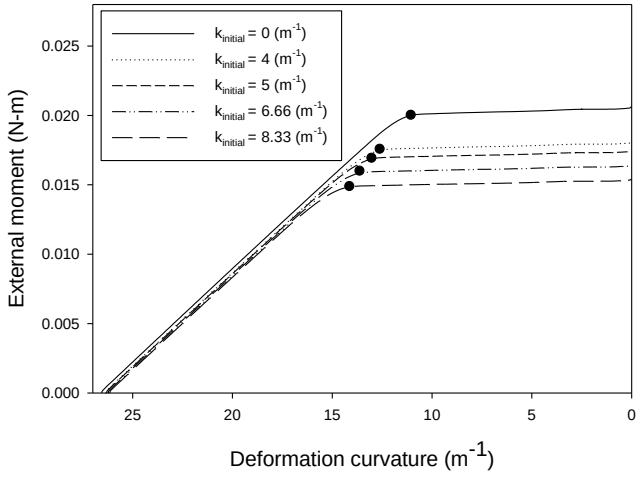

(b)

Figure 3.7 Curve of moment vs. deformation curvature for each initial tool-plate curvature (FEA results): (a) $M_x - {}_1\kappa_{xx}$ curve for snap-forth and (b) $M_y - {}_2\kappa_{yy}$ curve for snap-back.

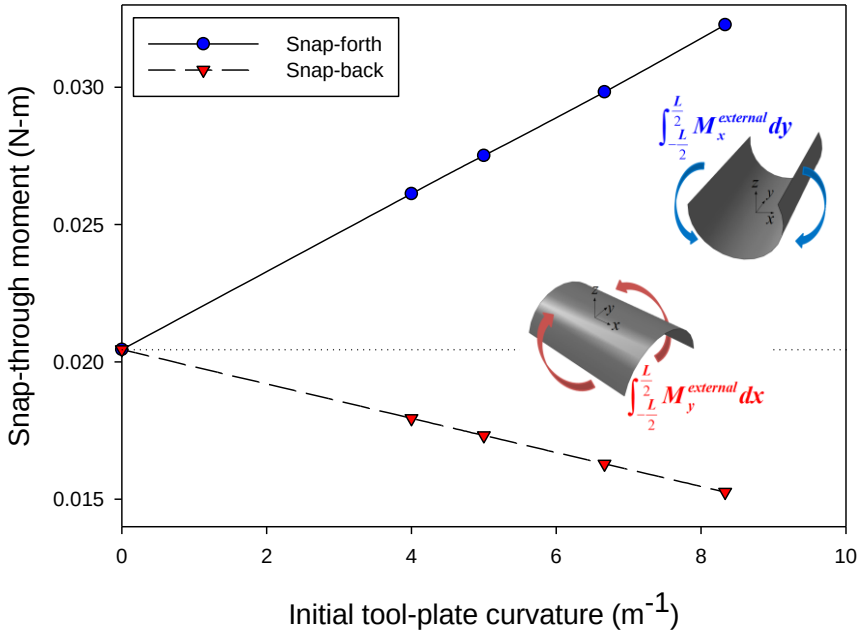

Figure 3.8 Change in snap-through moment with initial tool-plate curvature (FEA results).

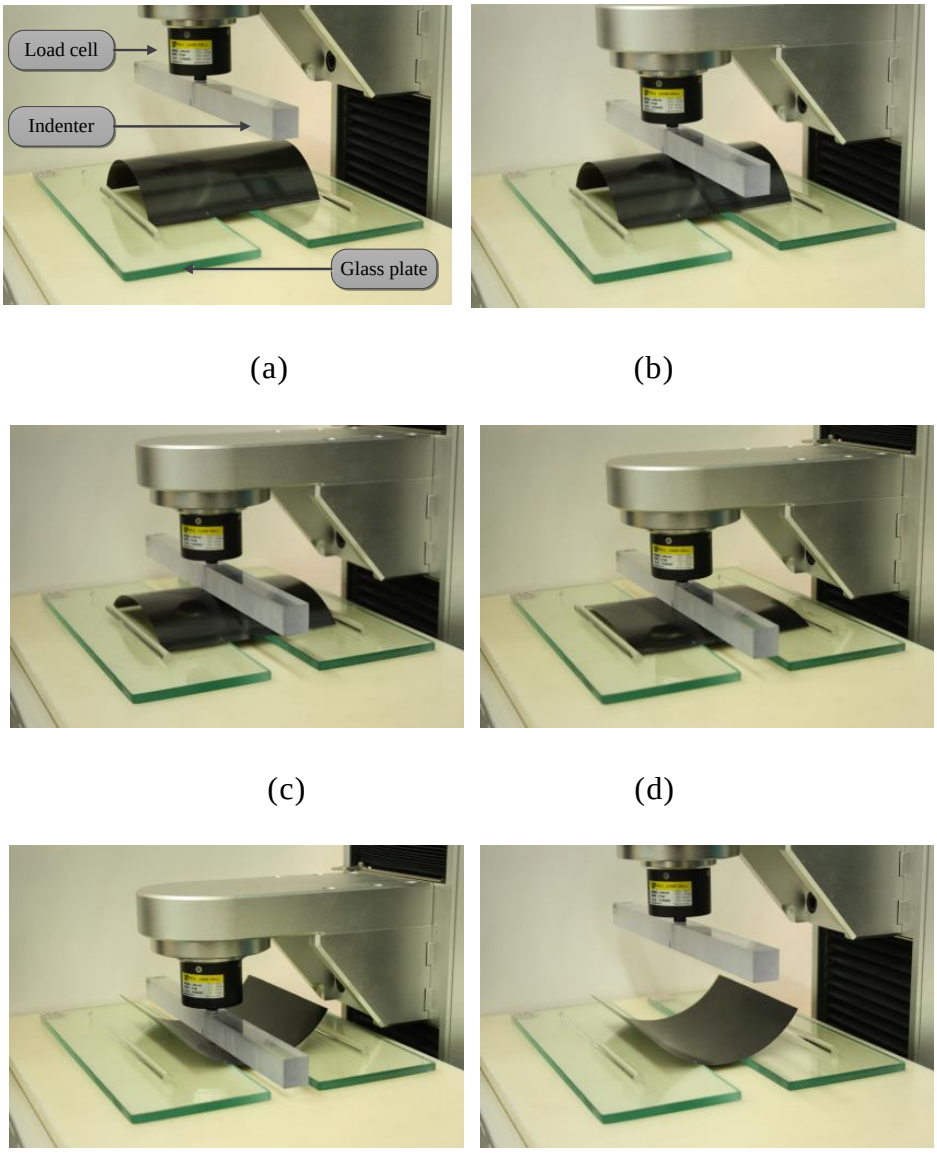

Figure 3.9 Experimental procedures for measuring snap-through load: (a) setup for vertical load test, (b) load induced by surface-to-surface contact, (c) continuous pressing, (d), (e) snap-through, and (f) unloading after snap-through.

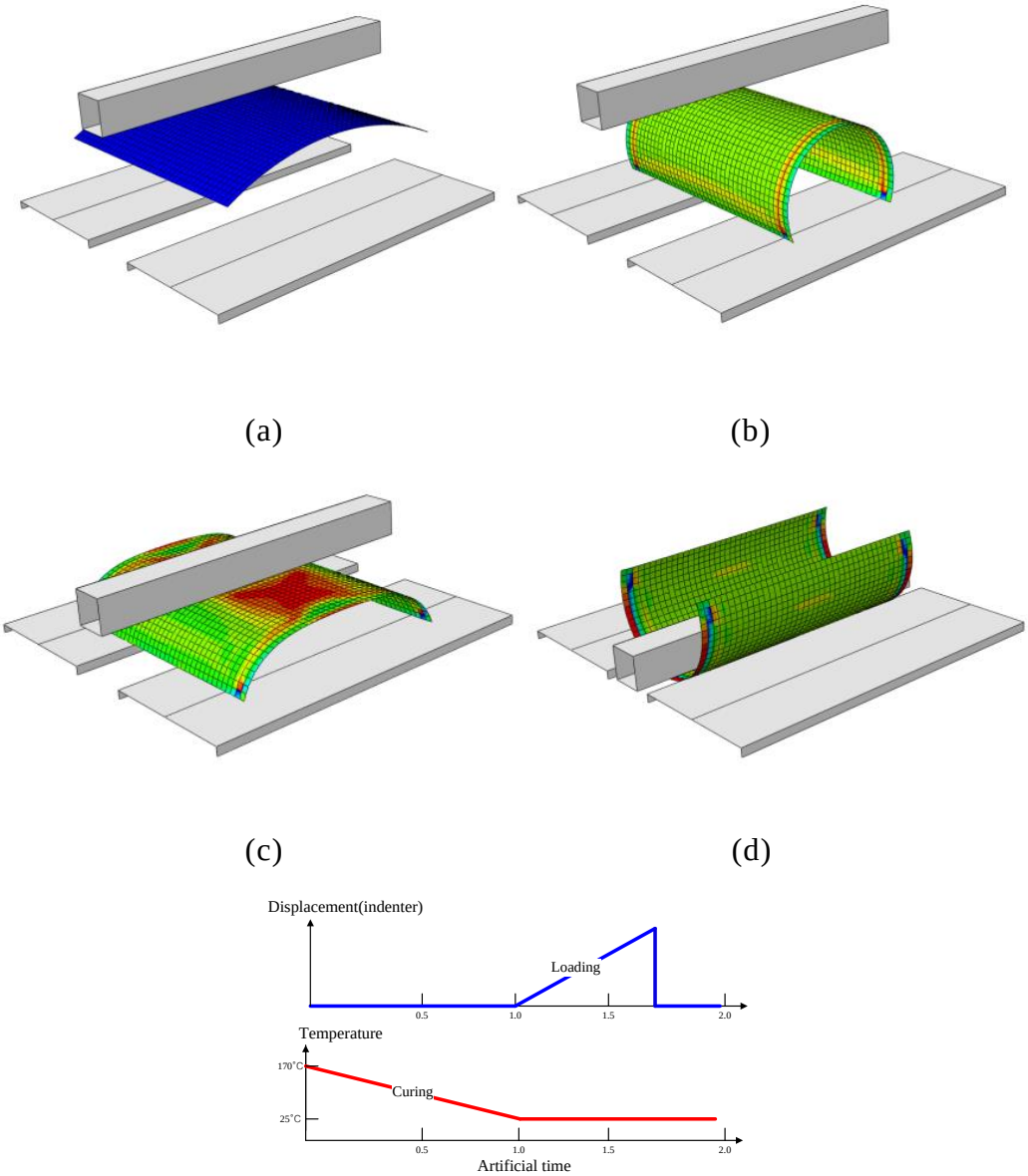

Figure 3.10 FE analysis of snap-through of bistable composite subjected to line-pressing load: (a) before curing process, (b) after curing process, (c) deformation before snap-through, (d) after snap-through, and (e) loading history of FE analysis.

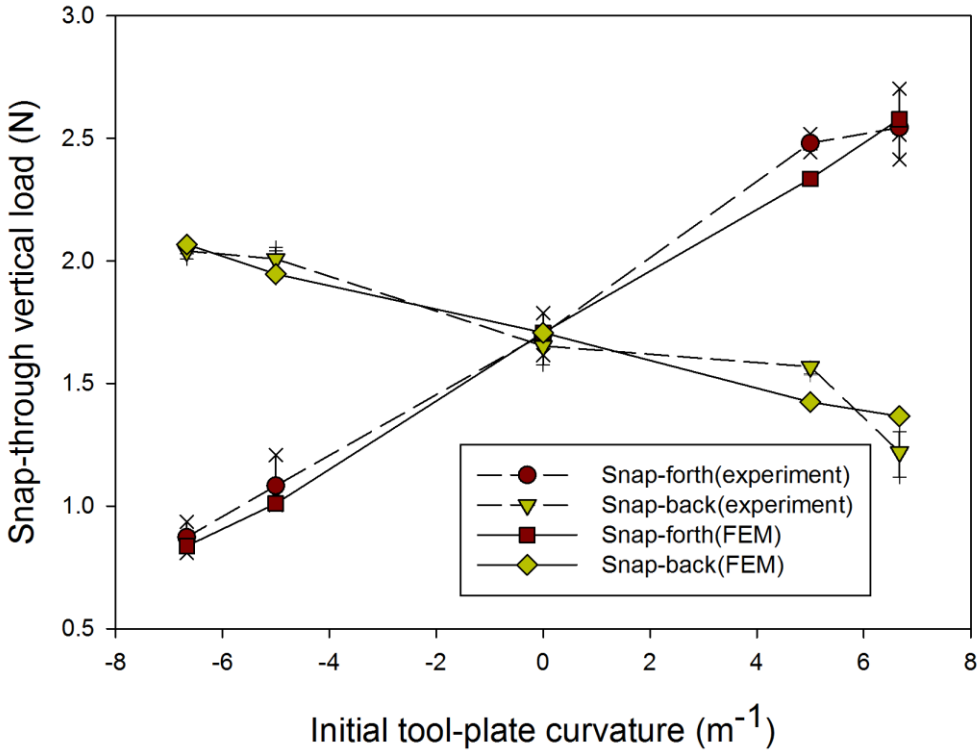

Figure 3.11 Change in snap-through load with initial tool-plate curvature.

Table 3.1 Material properties of carbon fiber prepreg

Parameter		Unit	
Axial tensile modulus	E_1	GPa	96
Transversal tensile modulus	E_2	GPa	6.9
Shear modulus	G_{12}	GPa	3.4
Poisson's ratio	ν_{12}		0.3
Thickness	t	Mm	0.085
Thermal expansion coefficient parallel to fiber direction	α_1	$°C^{-1}$	$0.19e^{-6}$
Thermal expansion coefficient perpendicular to fiber direction	α_2	$°C^{-1}$	$38e^{-6}$
Temperature change	ΔT	°C	-145

Chapter 4

FE model of bistable shell structure with SMA coil spring

4.1 Introduction

SMA spring is proper actuator in order to trigger the snap-through action of bistable structure because SMA spring generate the large recovery force and large recovery displacement during phase transformation which is induced by mechanical load or thermal load. However, in order to trigger the snap-through successfully by using SMA spring, a proper design of SMA spring must be accompanied. Even if design guide line of SMA spring is obtained, actual test (i.e. experiment) is also need to be performed to verify the design of SMA spring. At here, one thing that needs to be mentioned is the cost and effort of experiment test. If the snap-through load of bistable structure is not well predicted, there is high probability of failure of triggering the snap-through action with SMA spring even if SMA spring is designed properly. For this reason, before performing the experiment of snap-through with SMA spring, full

analysis of bistable structure with SMA spring is need to be performed in order to reduce probability of failure of triggering the snap-through action with SMA spring. For this reason, in this chapter, full FE model of bistable shell structure with SMA (Shape Memory Alloy) spring is developed. Firstly, in order to simulate the behavior of SMA, Lagoudas model, most well-known SMA model, is utilized by writing ABAQUS user subroutine (UMAT) with FORTRAN. Secondly, FE model of SMA spring is integrated over bistable composite and then the snap-through of bistable composite is induced by using shape memory effect of SMA spring.

4.2 FE analysis of SMA spring

4.2.1 FE model of SMA spring and constitutive equation of SMA

FEA was performed to predict the behavior of the single- and double-coil SMA springs. First, the FE models of both springs were discretized by 8-node isoparametric quadrilateral elements, and the cross section of the FE model consisted of 16 elements, as shown in Figure 4.1(a). The cross sections faced each other at regular intervals along the trajectory of the single- and double-coil spring (i.e. the center axis of the SMA wire, as shown in Figure 4.1(b)). The trajectories of the single-coil, φ_t^s, were expressed in a Cartesian coordinate system by Eq. (4.1). In the FEA simulation, the number of assembled elements in the FE model was approximately 32,000.

$$\vec{\varphi}_t^s = \vec{\varphi}_t^s\left(x(t),\ y(t),\ z(t)\right), \quad \text{where} \begin{bmatrix} x(t) = \dfrac{D+d}{2}\cos\left(\dfrac{D+d}{2n}t\right) \\ y(t) = \dfrac{D+d}{2}\sin\left(\dfrac{D+d}{2n}t\right) \\ z(t) = \dfrac{d\left(D+d\right)}{4n\pi}t \end{bmatrix} \tag{4.1}$$

where d indicate the wire diameter, D is the spring diameter, a is the pitch angle and n indicate the number of coils.

To reflect the behavior of the SMA in FE analysis, the Lagoudas model, which is a three-dimensional (3-D) SMA model [53], was implemented in ABAQUS, a commercial FEA package. Initially, a transformation function Φ had to be defined because the transformation function specifies the criteria of the phase transformation of the SMA. The transformation function was divided into two criteria with respect to the forward transformation and reverse transformation as follows:

$$\Phi = \begin{cases} \Pi^f - Y^* > 0, & \dot{\xi}_s > 0\text{: forward transformation} \\ -\Pi^b - Y^* < 0, & \dot{\xi}_s < 0\text{: reverse transformation} \end{cases} \tag{4.2}$$

where

$$\begin{cases} \Pi^f = \sigma_{ij}\Lambda_{ij} + \dfrac{1}{2}\Delta S_{ijkl}\sigma_{ij}\sigma_{kl} + \Delta\alpha_{ij}\sigma_{ij}\Delta T + \rho\left[\Delta c\left(\Delta T - T\ln\dfrac{T}{T_0}\right) + \Delta s_0 T - \Delta u_0 - b^M\xi_s - \left(\mu_1 + \mu_2\right)\right] \\ \quad \cong Y^* \\ \Pi^b = \sigma_{ij}\Lambda_{ij} + \dfrac{1}{2}\Delta S_{ijkl}\sigma_{ij}\sigma_{kl} + \Delta\alpha_{ij}\sigma_{ij}\Delta T + \rho\left[\Delta c\left(\Delta T - T\ln\dfrac{T}{T_0}\right) + \Delta s_0 T - \Delta u_0 - b^A\xi_s - \left(\mu_1 - \mu_2\right)\right] \\ \quad \cong -Y^* \end{cases} \tag{4.3}$$

where

$$\begin{aligned}
\Delta S_{ijkl} &= S^{M}_{ijkl} - S^{A}_{ijkl} \\
\Delta \alpha_{ij} &= \alpha^{M}_{ij} - \alpha^{A}_{ij} \\
\Delta c &= c^{M} - c^{A} \\
\Delta s_0 &= s^{M}_0 - s^{A}_0 \\
\Delta u_0 &= u^{M}_0 - u^{A}_0
\end{aligned} \tag{4.4}$$

The forward transformation is a phase transformation from the parent phase (twinned martensite or austenite phase) to the detwinned martensite phase, and the reverse transformation is a phase transformation from the detwinned martensite phase to the austenite phase. The variables σ_{ij}, Λ_{ij}, S^{λ}_{ijkl}, and α^{λ}_{ij} are the stress tensor, transformation tensor, elastic compliance tensor, and thermal expansion tensor, respectively. The superscript M and A denotes the reference state of the phase (i.e., *M* is for the martensite state and *A* is for the austenite state). Additionally, T, ρ, s_0, c, u_0, and ξ_s are the temperature, mass density, specific entropy, specific heat, specific internal energy, and detwinned martensite volume fraction, respectively. The detwinned martensite volume fraction, ξ_s, is distinguished from twinned martensite volume fraction, ξ_t. Total martensite volume fraction, ξ is defined by sum of the detwinned martensite volume fraction and twinned martensite volume fraction (i.e. $\xi = \xi_s + \xi_t$). The variables b^{λ}, μ_1, and μ_2 are hardening parameters. Among the hardening parameters, the parameters b^A and b^M represent the isotropic hardening moduli for the forward and reverse transformations, and the parameter μ_2 is determined

from the continuity condition of the polynomial-form hardening function [53]. Although the parameter μ_1 physically denotes the accumulation of elastic strain energy when the forward transformation begins, it is omitted for simplicity. These hardening parameters are expressed as follows:

$$\begin{aligned} b^A &= -\Delta s_0 \left(A^f - A^s \right) \\ b^M &= -\Delta s_0 \left(M^s - M^f \right) \\ \mu_2 &= \frac{1}{4} \rho \left(b^A - b^M \right) \end{aligned} \tag{4.5}$$

Finally, Y^* denotes the threshold of thermodynamic force Π at the onset of phase transformation.

The role of the thermodynamics force is similar to the yield surface in the theory of plasticity. Therefore, the numerical scheme is also simply applied for the evaluation of the transformation strain. When the strain and temperature are given, the increment of the detwinned martensite volume fraction and the transformation strain and stress can be calculated using a return mapping algorithm [53]. The distributions of the detwinned martensite volume fraction and transformation stress are illustrated in Figures 4.2 and 4.3, respectively.

To obtain material constants such as the Young's modulus, the tensile test of 0.25-1 spring was performed at 200 ℃ for 100% austenite state and 20 ℃ for 100% twinned martensite state, respectively. From this tensile test, the obtained displacement-to-force curve of the single-coil SMA spring can be transformed to

the shear stress-shear strain curve. To do this mapping procedure, a relation between the axial force and the final pitch angle of the single coil spring after deformation, and a relation between the shear stress and the axial force are utilized as follows [54].

$$F = \frac{\pi d^4}{8\left(D_1 + 2d\right)^2} G \frac{\cos^2 \alpha_i \left(\sin \alpha_f - \sin \alpha_i\right)}{\cos^2 \alpha_f \left(\cos^2 \alpha_f + \sin^2 \alpha_f / \left(1+\nu\right)\right)} \tag{4.6}$$

where α_i and α_f are the initial pitch angle of single coil spring before deformation and the final pitch angle of single coil spring after deformation which have to be estimated by deflection and the final pitch angle relation. The derivation Eq. (4.6) is explained in further details by An *et al* [54] .

$$\tau = \frac{T\left(d/2\right)}{J} = \frac{F\left(\frac{D_1 + 2d}{2}\right)\left(\frac{d}{2}\right)}{\left(\pi d^4 / 32\right)} = \frac{8\left(D_1 + 2d\right)F}{\pi d^3} = \frac{8CF}{\pi d^2} \tag{4.7}$$

where J denotes the polar moment of inertia and C denotes the spring index (i.e. $\mathrm{C} = (D_1 + d)/d$); T is the torsional moment applied to the cross-section of the single spring and F is the force applied to the axial deflection of spring.

By substituting the axial force, F of Eq. (4.6) into the shear stress of Eq. (4.7), and then rearranging the results into a shear stress-shear strain relation form, $\tau = G\gamma(\mathrm{C}, \mathrm{v}, \alpha_i, \alpha_f)$, the shear strain, $\gamma(\mathrm{C}, \mathrm{v}, \alpha_i, \alpha_f)$ can be derived as follows:

$$\gamma = \frac{1}{C} \frac{\cos^2 \alpha_i \left(\sin \alpha_f - \sin \alpha_i\right)}{\cos^2 \alpha_f \left(\cos^2 \alpha_f + \sin^2 \alpha_f / \left(1+\nu\right)\right)} = \frac{\tau}{G} \tag{4.8}$$

From these procedures, the transformed shear stress and shear strain curve was obtained, which is similar to displacement-to-force curve. The transformed shear stress-shear strain curve shows a nonlinear relation due to the phase transformation of the SMA. However, below a 1% shear strain, this curve shows an almost linear relation. Therefore, the shear moduli G_A and G_M were easily estimated using the linear fitting of the shear stress-shear strain curve with respect to the 100% austenite state and the 100% twinned martensite state, respectively, below a 1% shear strain. Furthermore, it can be considered as isotropic material in the case of polycrystalline material, which is the SMA wire in this study. So, these shear moduli can be easily converted into the Young's modulus by $2(1+\nu)G$, where ν is the Poisson's ratio. A Poisson's ratio of 0.33 is used based on the data sheet from the manufacturer. The maximum transformation shear strain γ_t was defined by estimating the unrecovered shear strain after unloading from the end of the detwinning. The maximum transformation strain, H, was calculated by $\gamma_t/\sqrt{3}$, which relation is equivalent to the effective strain of pure strain in the plasticity.

The four transformation temperatures, A^s, A^f, M^s, and M^f are obtained from DSC as explained in section 3.2.1. The difference of specific entropy between the martensite and austenite, Δs, is estimated by dividing the mean values of the exchanged heat during transformation, ΔH, by the phase equilibrium temperature, T_{eq} [55]. The phase equilibrium temperature can be approximately obtained by

calculating, $T_{eq} = \frac{1}{2}(M^s + A^f)$ [56]. The Difference of specific internal energy between martensite and austenite, Δu, can be obtained by calculating, $\Delta u = T_{eq}\Delta s$ [53]. It is assumed that there is no difference in specific heat between the martensite and austenite phase, Δc, because the specific heats are almost equal to each other (i.e. during forward transformation and reverse transformation) [53]. The isotropic hardening modulus for forward transformation, b^A, and the isotropic hardening modulus for reverse transformation, b^M, are obtained respectively by using $b^A = \Delta s(A^f - A^s)$ and $b^M = \Delta s(M^s - M^f)$. The threshold of thermodynamic force at the onset of phase transformation, Y^*, is calculated by $Y^* = -\frac{1}{2}\rho\Delta s(A^f - M^s) - \frac{1}{4}\rho\Delta s(M^s - M^f - A^f + A^s)$. The material constants of SMA used in the simulation are listed in Table 4.1.

4.2.2 The snap-through load of bistable composite without SMA spring

To design the SMA spring which can trigger the snap-through of bistable composite, the snap-through load of bistable composite must be estimated without installing SMA spring at bistable composite.

The snap-through action is induced by using Bending-Propagation-Actuation method [5]. Unlike common unbending actuation method which applies the force or moment along the curve of bistable structure, BPA applies the force or moment perpendicular to the curve of bistable structure. The corresponding

actuation method can trigger the snap-through action of curved bistable structure successfully without unexpected local bucking because BPA induce the bending deformation which keep a developable surface locally.

For the snap-through of the bistable composite under BPA, FE analysis was performed. Commercial FEM software, ABAQUS was used for FE analysis. FE model consist of three rigid washers and bistable composite, illustrated in Figure 4.4 (a). The simulation of BPA was performed with equivalent to Ref. [5]. The material property of the bistable composite is listed in Table 4.2.

The result of snap-through simulation is shown in Figure 4.4 (b). Based on the load-displacement profile, the snap-through load and stroke can be estimated. In the result, minimum snap-through load and stroke are 3.93N and 109mm respectively, in order to trigger of snap-through on the BPA.

4.2.3 Simple design of SMA spring for snap-through

In the load-displacement profile, there is two peaks before snap-through occur. In order to trigger snap-through with SMA spring, the SMA spring must exceed the two loads corresponding to the two peaks during backward phase transformation (i.e. contraction of SMA spring). Based on this result, the stiffness and stroke of SMA spring need to be designed. For design of SMA spring, there are several methods [5, 54]. In this thesis, the linear fitting method

is utilized [5]. This method defines the design constraint by linear fitting of two peak points. The slope of fitted line is related to the stiffness of SMA spring. The minimum stroke is related to the stroke performance and coil number of SMA spring. In order to satisfy the above design requirement of SMA spring, SMA spring is designed based on the framework of SMA spring design [54], as shown in Table 4.3.

4.3 Snap-through analysis of bistable composite with SMA spring

For the snap-through of the bistable composite with SMA spring, FE analysis was performed. Commercial FEM software, ABAQUS was used for FE analysis. FE model consist of three rigid washers, bistable composite and SMA spring on 100% austenite state initially. The first, second and third washers are located over the lower left, center and right corner of bistable composite, respectively. Initially, the center point of SMA spring is located over the second washer, as illustrated in Figure 4.5.

The linear hexahedron element (C3D8), the 4-node doubly curved thin shell element (S4) and the linear quadrilateral element (R3D4) were used for the mesh of the SMA spring, the bistable composite and the washer parts, respectively. The mesh density of the bistable composite part was chosen as 30 × 30(900 elements, element size of ~5 mm). The washer was represented by choosing 28

elements with element size of 4–5 mm. The interaction between the washer and the surface of bistable structure is considered by applying perfect bonding at the initial step of FE analysis.

FE analysis is divided into four main processes as follow: the curing process of bistable composite; the loading process of SMA spring in order to induce the phase transformation from twinned martensite phase to detwinned martensite phase; the unloading process of SMA spring to install it at the first and third washers; and finally, the heating process of SMA spring to trigger of snap-through of bistable composite.

1. In the curing process, the evaluation temperature (170 ℃) of bistable composite is reduced to the service temperature (25 ℃). Following the curing process, the bistable composite takes the cylindrical stable shape of Mode 1 as illustrated in Figure 4.6. And at the same time, SMA spring is stretched at both end point of spring while generating martensite volume fraction as shown in Figure 4.7. The SMA spring is stretched from initial point to the specified point which is located in parallel to the stretching-line of the SMA spring. During stretching, SMA spring experience the phase transformation from the twined martensite phase to the detwinned martensite phase Figure 4.7 (b).
2. In the unloading process, SMA spring is relaxed by removing the boundary constraint which was applied to stretch the SMA spring at the both end point of spring. At the first time of unloading process, the both end point

SMA spring is not contacted with the first and third washers. However, as the relaxation process progresses, the both end point of SMA spring is contacted with the first and third washer. Although SMA spring is unloaded, SMA spring dose not experience the backward phase transformation from detwinned martensite phase to the austenite phase because the current temperature of SMA spring is lower than the austenite starting temperature (52 ℃)

3. At the heating process, The SMA spring is heated from the service temperature (25 ℃) to the high temperature (180℃) which is higher than austenite finish temperature (63.9 ℃). As the SMA spring is more and more heated, SMA spring experience the backward phase transformation from detwinned martensite phase to the austenite phase as shown in Figure 4.8 (b). Due to this backward transformation accompanied with shape recovery and large recovery force of SMA spring, the SMA spring induce the bending deformation of bistable structure on Mode 1 state as shown in Figure 4.8. At here, the aspect of bending deformation of bistable structure keeps a globally developable surface because the corresponding surface can minimize the strain energy based on the Gauss's Theorema Egregium [50]. Following a continuous heating process accompanied by this recovery of SMA spring and bending deformation of bistable structure, the bending deformation is more and more propagated and the corresponding strain energy is also increased progressively. Finally, if the strain energy reaches

the critical point, the snap-through, from Mode 1 state to Mode 2 state, occurs instantaneously, as shown in Figure 4.9.

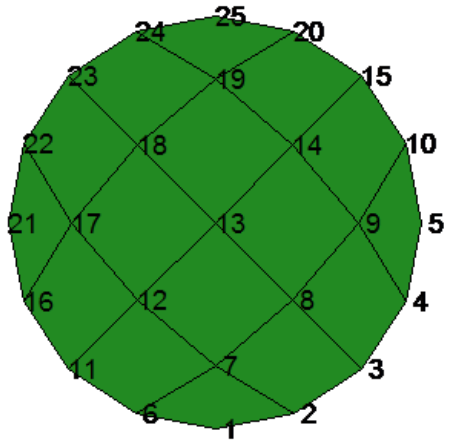

(a)

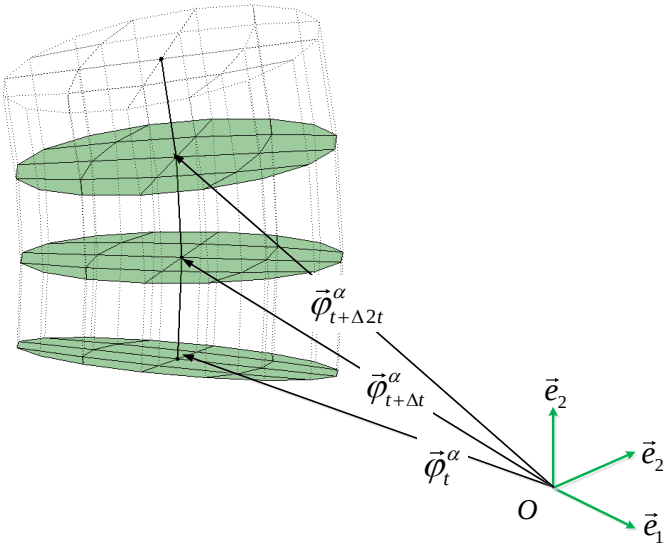

(b)

Figure 4.1 Cross section of SMA wire.

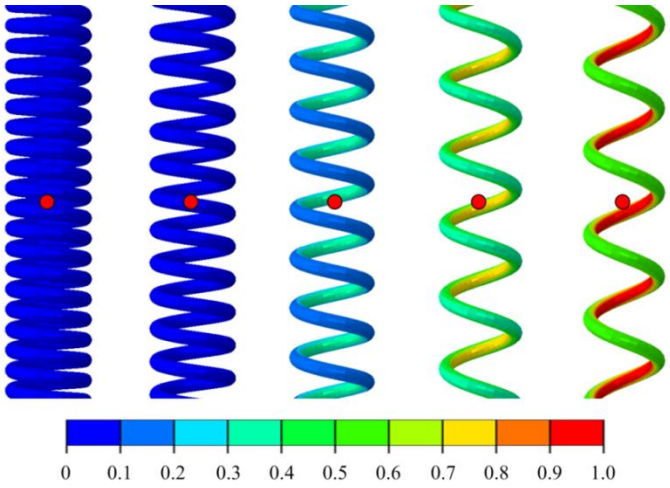

Figure 4.2 Distribution of martensite volume fraction in FEA model of 0.25-1 spring at 20 ℃. Red dot is a reference point.

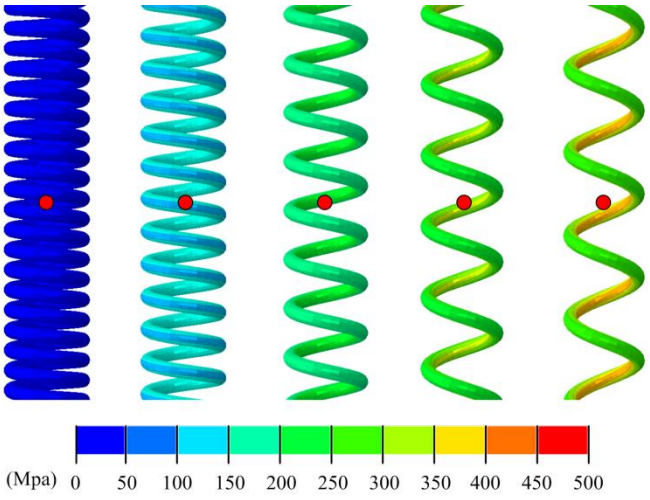

Figure 4.3 Distribution of von Mises stress in FEA model of 0.25-1 spring at 20 ℃. Red dot at the first left figure is a reference point.

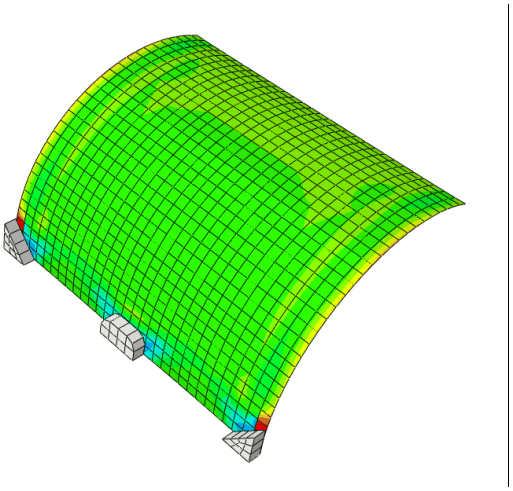

(a)

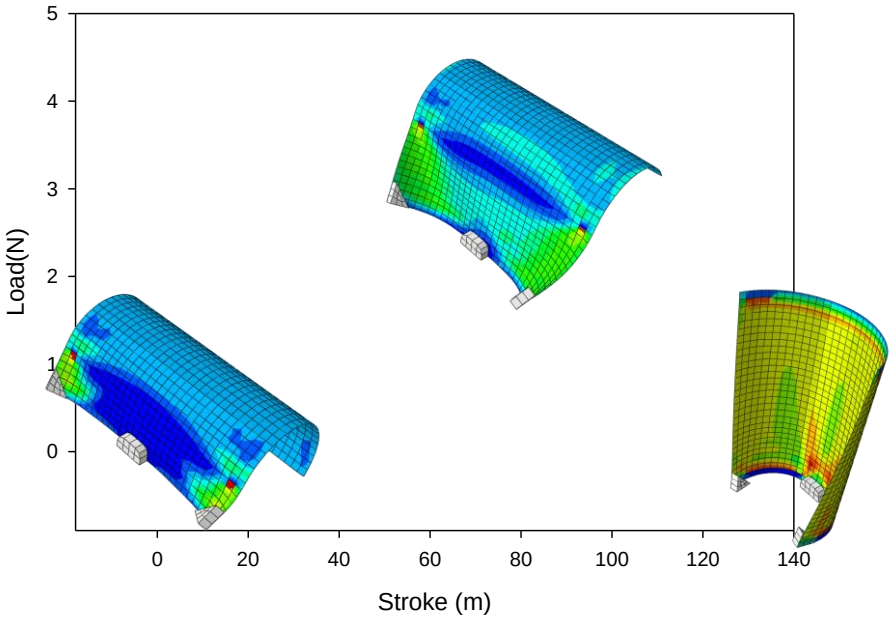

(b)

Figure 4.4 The snap-though analysis of bi-stable composite under BPA: (a) FE model of bi-stable composite and (b) load-stroke curve during BPA

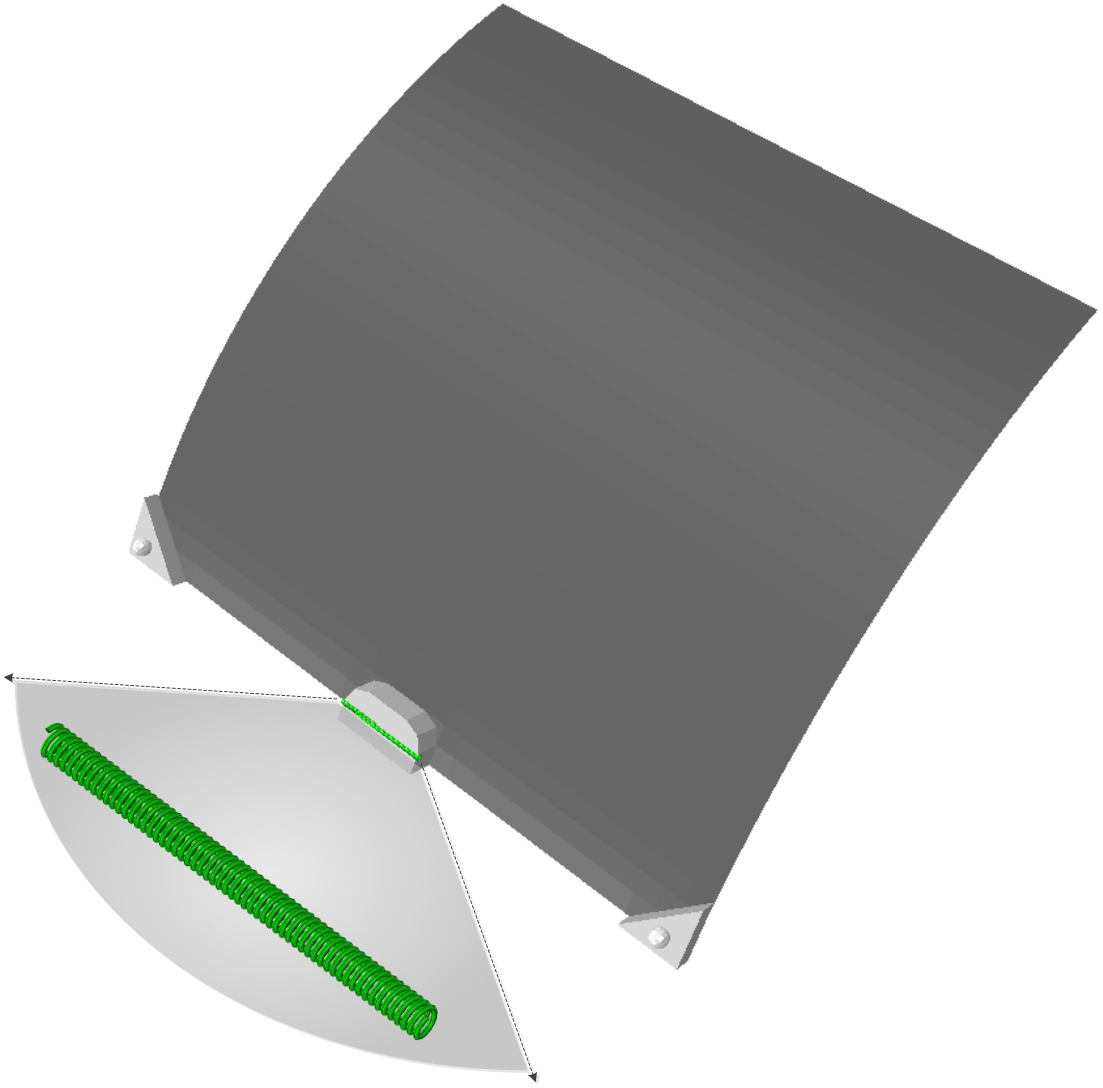

Figure 4.5 FE model of bi-stable composite with SMA spring: (a) Zoom-out at the position of SMA spring (b) zoom-in at the position of SMA spring

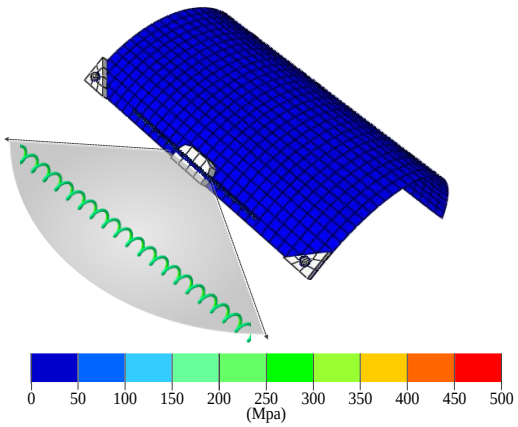

(a)

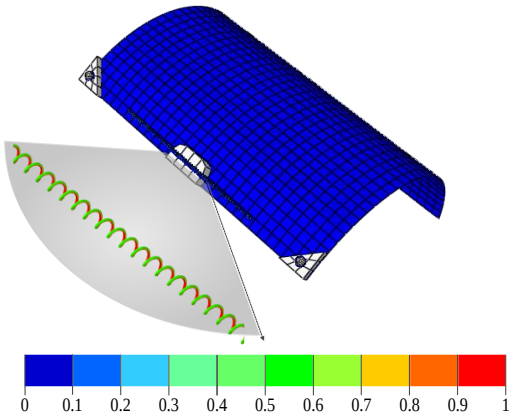

(b)

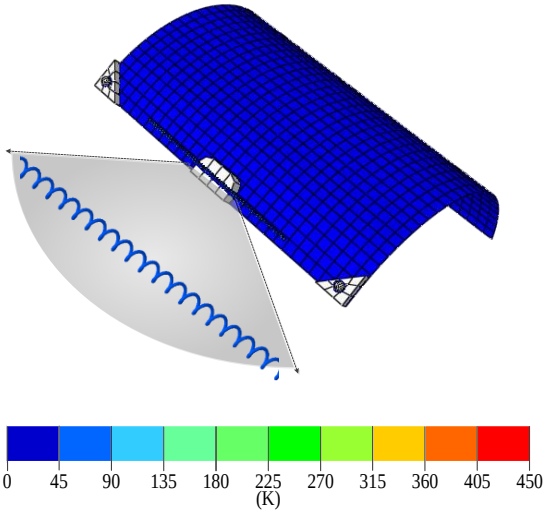

(c)

Figure 4.6 Curing process of bi-stable composite and shape memorizing process of SMA spring by stretching (a) stress contour (b) MVF contour and (c) temperature contour of SMA spring

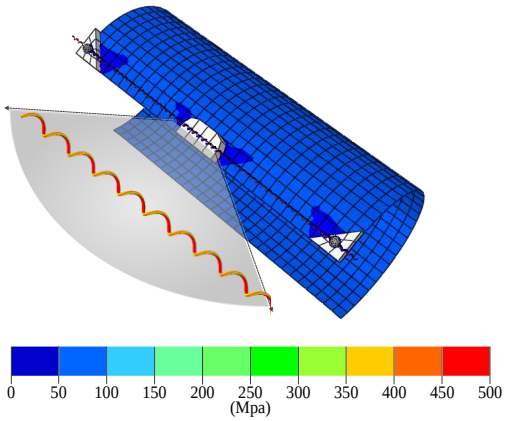

(a)

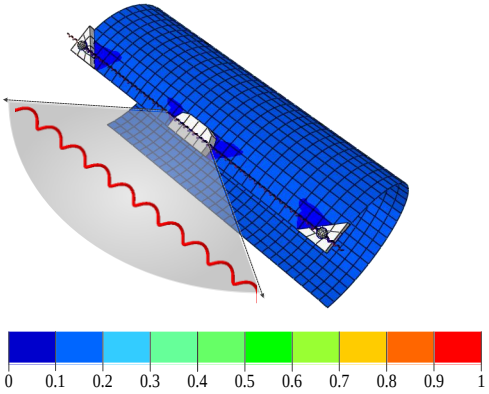

(b)

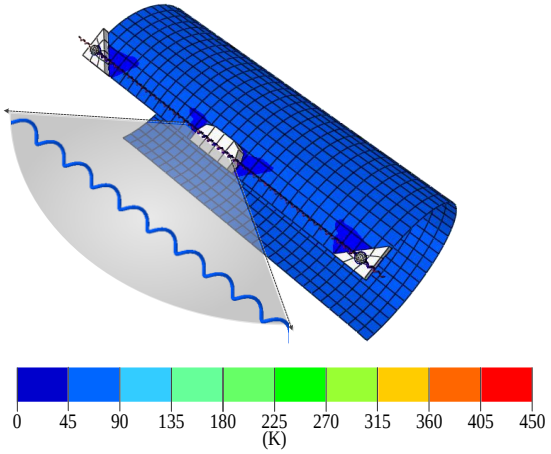

(c)

Figure 4.7 After curing of bi-stable composite (Mode 1) and after shape memorizing of SMA spring by stretching: (a) stress contour (b) MVF contour and (c) temperature contour of SMA spring

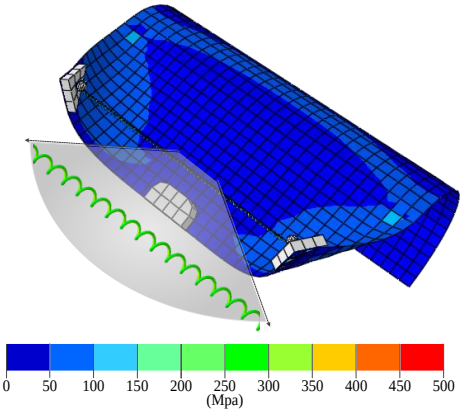

(a)

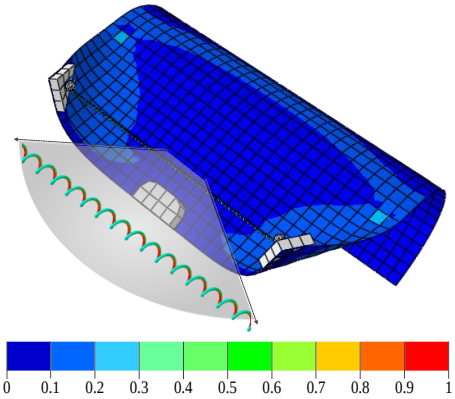

(b)

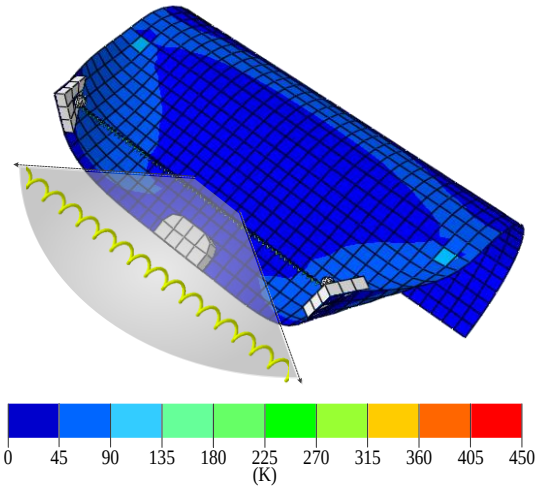

(c)

Figure 4.8 Snap-through process of bi-stable composite by heating the stretched SMA spring: (a) stress contour (b) MVF contour and (c) temperature contour of SMA spring

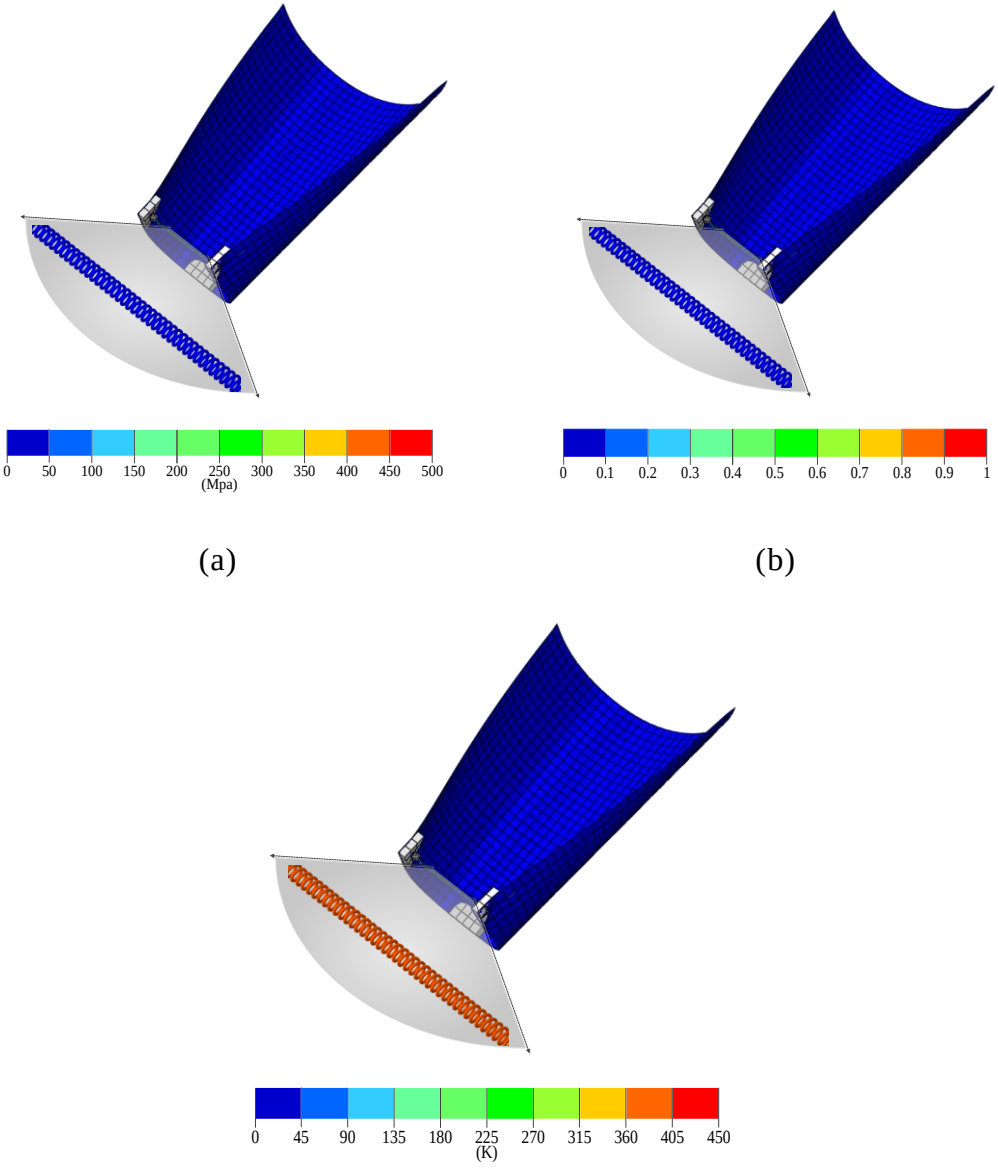

(a) (b)

(c)

Figure 4.9 After snap-through of bi-stable composite (Mode 2) by heating the stretched SMA spring: (a) stress contour (b) MVF contour and (c) temperature contour of SMA spring

Table 4.1 Material constants of SMA wire.

Parameter	Specification	Unit	Value	Note
E^M	Young's modulus of martensite	GPa	21.07	Estimated
E^A	Young's modulus of austenite	GPa	54.796	Estimated
ν^M	Poisson's ratio of martensite	—	0.33	†From data sheet
ν^A	Poisson's ratio of austenite	—	0.33	†From data sheet
α^M	Thermal expansion coefficient of martensite	1/K	6.6×10^{-6}	†From data sheet
α^A	Thermal expansion coefficient of austenite	1/K	11.0×10^{-6}	†From data sheet
H	Maximum transformation strain	—	0.0288	Measured
ρ	Mass density	kg/m^3	6,450	†From data sheet
A^s	Austenite start temperature	K	325.2	Measured
A^f	Austenite finish temperature	K	337.1	Measured
M^s	Martensite start temperature	K	274.6	Measured
M^f	Martensite finish temperature	K	243.4	Measured
Δc	Difference of specific heat between martensite and austenite	—	0	Refer from [29]
Δu	Difference of specific internal energy between martensite and austenite	J/kg	−10,474	Estimated
Δs	Difference of specific entropy between martensite and austenite	J/kg	−34.26	Estimated
b^A	Isotopic hardening moduli for forward transformation	J/kg	407.73	Estimated
b^M	Isotopic hardening moduli for reverse transformation	J/kg	107.24	Estimated
Y^*	Threshold of thermodynamic force Π at onset of phase transformation	MPa	7.967	Estimated

† Data sheet is from Dynalloy, Inc.

Table 4.2 Material properties of carbon fiber prepreg

Parameter		Unit	
Axial tensile modulus	E_1	GPa	160
Transversal tensile modulus	E_2	GPa	12
Shear modulus	G_{12}	GPa	8
Poisson's ratio	ν_{12}		0.3
Thickness	t	Mm	0.09
Thermal expansion coefficient parallel to fiber direction	α_1	$°C^{-1}$	$0.19e^{-6}$
Thermal expansion coefficient perpendicular to fiber direction	α_2	$°C^{-1}$	$31.8e^{-6}$
Temperature change	ΔT	°C	-145

Table 4.3 Specification of designed SMA spring

Parameter		Unit	
Wire diamter	d	mm	0.125
Spring diameter	D	mm	1.5
Pitch angle	*a*		0
Number of coils	n		60

Chapter 5

Saddle shape bistable structure with constant curvature

5.1 Introduction

Bistable structures are a very attractive morphing component, because it can be snapped from one stable state to the other stable state just by a small applied force or moment, and each state remains stable without additional energy supply. However, its availability is quite limited because most of bistable composites (unsymmetric laminated bistable composites) have a restrictive final configuration (cylindrical shape) to be applied in soft-morphing fields. This paper presents a saddle-shaped bistable plate to satisfy the more different needs in soft-morphing fields. Firstly, its bistability and final shapes are investigated by means of the Rayleigh-Ritz approximation method and FEM. The results obtained by analytical method and by FEM shows a good agreement quantitatively. Furthermore, for the practical application of saddle-shaped bistable plate, a snap-through process is simulated by FEM, and then a simple

design guideline of an actuator, such as a shape memory alloy spring, is suggested based on the result obtained by FE analysis of snap-through.

5.2 Strain fields of the saddle-shaped bistable structure

The saddle-shaped bistable structure is realized by perfect bonding between face-to-face surfaces of two saddle-shaped plates on stress-free state. To get a mechanical intuition about why the saddle-shaped bistable plate is realizable by aforementioned method, the strain energy of the saddle-shaped bistable plate need to be defined mathematically. For this, it is also necessary to define strain fields of the saddle-shaped bistable plate preferentially.

From the assumption of small and elastic strain, the total strain field of the saddle-shaped bistable plate can be defined by sum of an initial strain (a restrained-strain into flat shape), $E_{ij}^{(1)}$ and a final strain (a relaxed-strain from flat shape), $E_{ij}^{(2)}$.

$$E_{ij} = E_{ij}^{(1)} + E_{ij}^{(2)} \tag{5.1}$$

At here, if a fictitious reference state is introduced as a flat shape as illustrated in Figure 5.1, each strain can be described in the Cartesian coordinate system, not in the complicated curvilinear coordinate system, From on the basis of the

reference state, the restrained strain is defined by difference between the metric tensor of the reference state and the metric tensor of the initial state, namely,.

$$E_{ij}^{(1)} = \frac{1}{2}\left(\delta_{ij} - G_{ij}\right) \tag{5.2}$$

In similar way, the relaxed strain is also defined by difference between the metric tensor of final state and the metric tensor of the reference state in Eq. (5.3).

$$E_{ij}^{(2)} = \frac{1}{2}\left(g_{ij} - \delta_{ij}\right) \tag{5.3}$$

In other words, each strain can be described from the artificial displacement field defined on the basis of the reference state and the total strain field can be represented by the change of metric as depicted in Eq. (5.4).

$$\begin{aligned} E_{ij} &= \underbrace{\frac{1}{2}\left(\delta_{ij} - G_{ij}\right)}_{E_{ij}^{(1)}} + \underbrace{\frac{1}{2}\left(g_{ij} - \delta_{ij}\right)}_{E_{ij}^{(2)}} \\ &= \frac{1}{2}\left(g_{ij} - G_{ij}\right) \end{aligned} \tag{5.4}$$

By assuming the shape of the initial and final state as a saddle shape with constant curvature, an artificial displacement field is can be described by the trigonometric function as follow [41].

$$\begin{aligned} u &= \left(R_{xx} - z\right)\sin\kappa_{xx}x - x \\ v &= \left(R_{yy} - z\right)\sin\kappa_{yy}y - y \\ w &= \left(R_{xx} - z\right)\left(1 - \cos\kappa_{xx}x\right) + \left(R_{yy} - z\right)\left(1 - \cos\kappa_{yy}y\right) \end{aligned} \tag{5.5}$$

By using the assumption of a plane stress state, a small strain assumption and a thin plate/shell assumption, the relaxed strain can be reduced to a following simple form.

$$\begin{Bmatrix} \varepsilon_{xx}^{relax} \\ \varepsilon_{xx}^{relax} \\ \gamma_{xy}^{relax} \end{Bmatrix} = \begin{bmatrix} a_1^{relax} + a_2 y^2 \\ b_1^{relax} + b_2 x^2 \\ \left(\kappa_{xx}^{relax} \kappa_{yy}^{relax} + 2a_1^{relax} + 2b_1^{relax} \right) xy \end{bmatrix} - \begin{bmatrix} \kappa_{xx}^{relax} \\ \kappa_{yy}^{relax} \\ 0 \end{bmatrix} z \tag{5.6}$$

At here, a mid-plane normal and a shear strain term (a_1^{relax} , b_1^{relax} , $\kappa_{xx}^{relax} \kappa_{yy}^{relax} xy$) was partially derived from the Green-Lagrangian strain based on the trigonometric displacement functions which can exactly express cylindrical and saddle shape with a constant curvature. The rest mid-plane strain term($a_2 y^2$, $b_2 x^2$) was introduced to satisfy global force and global moment equilibrium at the edge of the bistable structure; and the rest mid-plane shear strain term($2a_1^{relax} xy$, $2b_1^{relax} xy$) was derived from the compatibility condition.

The restrained strain is defined similar with the relaxed strain. However, it should be noted that the restrained strain is divided into a part of upper plate and a part of lower plate, according to the position of plate on the basis of z-axis (i.e., $z = 0$) because the saddle-shaped bistable plate is realized by perfect bonding between face-to-face surfaces of two saddle-shaped plates on stress-free state. The restrained strain are thus given by

$$\begin{Bmatrix} \varepsilon_{xx}^{restrain} \\ \varepsilon_{yy}^{restrain} \\ \gamma_{xy}^{restrain} \end{Bmatrix}^{(upper)} = -\left(\begin{bmatrix} a_1^{restrain} + a_2^{restrain} y^2 \\ b_1^{restrain} + b_2^{restrain} x^2 \\ \left(-\kappa_{xx}^{restrain} \kappa_{yy}^{restrain} + 2a_1^{restrain} + 2b_1^{restrain} \right) xy \end{bmatrix} - \begin{bmatrix} (+)\kappa_{xx}^{restrain} \\ (-)\kappa_{yy}^{restrain} \\ 0 \end{bmatrix} z \right)^{(upper)} \tag{5.7}$$

$$\begin{Bmatrix} \varepsilon_{xx}^{restrain} \\ \varepsilon_{yy}^{restrain} \\ \gamma_{xy}^{restrain} \end{Bmatrix}^{(lower)} = -\left(\begin{bmatrix} a_1^{restrain} + a_2^{restrain} y^2 \\ b_1^{restrain} + b_2^{restrain} x^2 \\ \left(-\kappa_{xx}^{restrain} \kappa_{yy}^{restrain} + 2a_1^{restrain} + 2b_1^{restrain} \right) xy \end{bmatrix} - \begin{bmatrix} (-)\kappa_{xx}^{restrain} \\ (+)\kappa_{yy}^{restrain} \\ 0 \end{bmatrix} z \right)^{(lower)} \tag{5.8}$$

Two saddle-shaped plates on stress-free state are identical in shape to each other but the principal curvature direction of those is opposite to each other.

As mentioned before, the total strain field of the saddle-shaped bistable plate is represented by sum of the restrained strain and the relaxed strain as follow.

$$\begin{Bmatrix} \varepsilon_{xx} \\ \varepsilon_{yy} \\ \gamma_{xy} \end{Bmatrix} = \begin{bmatrix} a_1 + a_2 y^2 \\ b_1 + b_2 x^2 \\ \left(\kappa_{xx}^{relax} \kappa_{yy}^{relax} - \kappa_{xx}^{restrain} \kappa_{yy}^{restrain} + 2a_1 + 2b_1 \right) xy \end{bmatrix} - \begin{bmatrix} \kappa_{xx}^{relax} - (\pm)\kappa_{xx}^{restrain} \\ \kappa_{yy}^{relax} - (\mp)\kappa_{yy}^{restrain} \\ 0 \end{bmatrix} z \tag{5.9}$$

, where the upper sign of the restrained curvature is corresponding to the total strain of the upper plate and the lower sign of the restrained curvature is corresponding to the total strain of the lower plate. Note that a constant mid-plane normal strain, a_1 is the unknown variable defined by difference between the constant in-plane normal relaxed strain and the constant in-plane normal restrained strain. The rest mid-plane strain term, a_2, b_1, b_2 is also the unknown variable and is defined in a similar way.

The in-plane shear strain term in Eq. (5.9) explain why saddle shape ($\kappa_{xx}^{relax} \neq 0$,

$\kappa_{yy}^{relax} \neq 0$) is possible, not a cylindrical shape or flat shape. If the side-length of plate is sufficiently long and the final shape is cylindrical shape ($\kappa_{xx}^{relax} = 0$, $\kappa_{yy}^{relax} \neq 0$ or $\kappa_{xx}^{relax} \neq 0, \kappa_{yy}^{relax} = 0$) or flat shape ($\kappa_{xx}^{relax} = 0$ and $\kappa_{yy}^{relax} = 0$), the in-plane shear strain, γ_{xy} have a non-zero value and increase as the side-length increase. Consequently, the strain energy of a cylindrical shape or flat shape exceeds the that of a saddle shape as the side-length increase. For this reason, the saddle shape is more stable than the cylindrical shape or flat shape in terms of the strain energy when the side-length is long enough. These mechanical backgrounds lead the shape of final state to the saddle shape.

5.3 Analytical model to predict the final shape of the saddle-shaped bistable structure

In this section, an analytical model is developed to predict the final shape of the saddle-shaped bistable structure. The solution (i.e., the final shape) is obtained by minimizing the total potential energy of the bistable structure. This minimization is achieved by equating the first variation of the total potential energy, $\delta\Pi$.

Using the aforementioned total strain field and assuming a plane stress state, the total potential energy is expressed as following form.

$$\Pi = \sum_{i=1}^{n} \int_{-\frac{L}{2}}^{\frac{L}{2}} \int_{-\frac{L}{2}}^{\frac{L}{2}} \int_{z_i^{btm}}^{z_i^{top}} \frac{1}{2} \overline{Q_{11}^i} \varepsilon_{xx}^2 + \frac{1}{2} \overline{Q_{22}^i} \varepsilon_{yy}^2 + \overline{Q_{12}^i} \varepsilon_{xx} \varepsilon_{yy} + \frac{1}{2} \overline{Q_{66}^i} \gamma_{xy}^2 \, dz dx dy \tag{5.10}$$

, where $\overline{Q_{\alpha\beta}^i}$ is the transformed plane stress reduced stiffnesses of i-th plate and L is the side length of the bistable plate. Symbols z_i^{top}, z_i^{btm} refer to the position of the upper surface and the lower surface corresponding to i-th plate, respectively.

The first variation of total potential energy, $\delta\Pi$ should be equal to zero to guarantee the existence of solution. The requirement for the existence of solution is as follow.

$$\delta\Pi = \left(\frac{\partial \Pi}{\partial a_1}\right)\delta a_1 + \left(\frac{\partial \Pi}{\partial b_1}\right)\delta b_1 + \left(\frac{\partial \Pi}{\partial a_2}\right)\delta a_2 + \left(\frac{\partial \Pi}{\partial b_2}\right)\delta b_2 + \left(\frac{\partial \Pi}{\partial \kappa_{xx}^{relax}}\right)\delta \kappa_{xx}^{relax} + \left(\frac{\partial \Pi}{\partial \kappa_{yy}^{relax}}\right)\delta \kappa_{yy}^{relax} = 0 \tag{5.11}$$

Eq. (5.11) is the nonlinear algebraic equations which have six-unknowns: $a_1, a_2, b_1, b_2, \kappa_{xx}^{relax}, \kappa_{yy}^{relax}$. In order to solve these nonlinear algebraic equations, The Newton-Raphson iterative method was used. At first iteration, an initial solution was assumed as a saddle shape. At next iteration, a subsequent solution was considered as the initial solution. The second variation of total potential energy (i.e., jacobian) was estimated to identify the stability of the system in each iteration.

5.4 FE model to predict the final shape of the saddle-shaped bistable structure

For the verification of the analytical model, FE analysis was performed. Commercial FEM software, ABAQUS was used for prediction of the final shape of saddle-shaped bistable plate. FE model consist of two rigid plates and two saddle-shaped plates on stress-free state, as illustrated in Figure 5.2. The two plates are identical in shape to each other, but one of the two plates is flipped over and located under the other. These two plates are aligned parallel to each other in principal direction of curvature. The two rigid plates are spaced apart at regular interval with the two saddle-shaped plates on stress-free state.

FE analysis is divided into two main processes; the pre-stressing process for generation of residual stress and the relaxation process for the energy minimization of the bistable plates.

1. At pre-stressing process, the residual stress is generated by pressing the two saddle-shaped plates flat. With this in mind, the upper rigid plate, the upper plate and the lower plate are only allowed to move in vertical dir. (i.e., z-dir.), but every movement of the lower rigid plate is fixed entirely.

1) Initially, the two rigid plate and the two plates are separated each other, as shown in Figure 5.2, but as the upper rigid plate move downward in the

vertical dir., the bottom surface of the upper rigid plate is contacted with the top surface of the upper plate.

2) After this contact, the upper rigid plate and the upper plate move downward together without any deformation. But at some point, the bottom surface of the upper plate is contacted with the top surface of the lower plate as depicted in Figure 5.3(a).

3) After this surface-to-surface contact between the upper plate and the lower plate, even the lower plate move downward together with the upper rigid plate and the upper plate. Then, finally, the bottom surface of the lower plate is contacted with top surface of lower rigid plate, and then the deformation and contact of the two plates is initiated and propagated, as illustrated in Figure 5.3 (b). In this step, the slip between the upper plate and the lower plate is allowed in tangential dir.

4) As the upper rigid plate move more downward, the two plates become more and more flat and a residual stress is generated at the same time. Until the two plates are flattened entirely, as shown in Figure 5.3(c), the upper rigid plate keeps moving downward.

2. At relaxation process, the strain energy of the two plates, which are constrained to flat shape, is minimized by separating the two rigid plates from the two plates.

1) Before separating the two rigid plates, the perfect bonding condition between face-to-face surfaces of the two plates is achieved by restrain the separation and slip between the upper plate and the lower plate, as opposed to pressing process.

2) After assigning the perfect bonding condition, the two rigid plates are separated from the two plates in which a residual stress exist in order to minimize the strain energy of two plates.

3) As the stain energy is minimized, one stable saddle shape is generated as shown in Figure 5.3(d). Following this analysis step, the other stable saddle shape is induced by mechanical load (line-moment or concentration force) as illustrated in Figure 5.3(e).

In this FE static analysis, the selected elements for this analysis were the 4-node doubly curved thin shell element S4, and a mesh density was chosen as 360 elements in consideration of a convergence property and computation time. In simulating contact, 'Surface-to-Surface' discretization method and 'Finite sliding' sliding formulation were used.

5.5 The comparison between the analytical result and FE result

In order to verify the analytical model, two stable configuration of the saddle-shaped bistable plate with different side-length were studied by using the

analytical model and FE model. These two stable shapes are divided into Mode 1 and Mode 2 for the convenience of understanding. Mode 1 is defined as a saddle shape with plus x-dir. curvature and minus y-dir. curvature. On the contrary, Mode 2 is defined as a saddle shape with minus x-dir. curvature and plus y-dir. curvature as shown in Figure 5.4.

Material properties of plate used in analysis are summarized in Table 5.1. In this analysis, one thing to note here is that both principal curvature of the two saddle plate on stress-free state, however, is initially fixed in a constant absolute value ($6.667\,m^{-1}$) before perfect bonding between face-to-face surfaces of the two saddle plates. In other word, the initial curvature is one of the control variables. The side-length varied from 1 mm to 160mm to check a bistability and estimate the corresponding final curvature.

The results of the analytical model and FE model are shown in Figures 5.5 and 5.6. Line with diamond marker is corresponding to the Mode 1 final curvature of the saddle shaped bistable plate and Line with circle maker is corresponding to the Mode 2 final curvature of the saddle-shaped bistable plate. The final curvature obtained by the analytical model show a good agreement with the result obtained by FE model.

In the range of 0 mm to 50mm side-length, both final curvatures are restrained to zero curvature; the bistability is not identified in this range. However, as the side-length pass a bifurcation point, the final curvature is divided into two

curvatures which have a different principal direction, but a same absolute value, that is to say, the bistability is identified at specific side-length which is over the bifurcation point. Additionally, it is interesting that the final curvature of the saddle shaped bistable become almost same with the absolute value of initial curvature as the side-length increase.

Additionally, the effect of the thickness change and initial curvature change are analyzed as shown in Figures 5.5, 5.6, 5.7 and 5.8. As the thickness of saddle plate on stress-free state increase, the bifurcation point, which starts recovering the bistability, become delayed. On the contrary to this, as the initial curvature of saddle plate on stress-free state increase, the bifurcation point becomes moved forward.

This result suggests the guideline on how to obtain the bistability of structure easily. More specifically, in order to obtain the bistability stably, the ratio of side length to thickness of saddle plate on stress-free state needs to be small sufficiently. In addition to the ratio, the initial curvature of saddle plate on stress-free state needs need to be large sufficiently.

5.6 Snap-through analysis of the saddle-shaped bistable structure with an actuator and its simple design guideline

The feasibility and the final shape of the saddle bistable structure are identified and estimated by means of the developed analytical model and FE model in advance. In this section, by going one step further, snap-through process of saddle-shaped bistable plate with an actuator is simulated by FEM for the practical application of that and then a simple design guideline of an actuator, such as a Shape Memory Alloy spring, is suggested based on the result obtained by FE analysis.

FE model for snap-through analysis consist of two wires, three rigid poles, and the saddle-shaped bistable plate, which is analyzed in advance, as illustrated in Figure 5.9(a). The snap-through of the saddle shaped bistable plate is induced by thermal contraction of the wire which is installed on the three rigid poles which play a role of moment arm. The three rigid poles are located in normal direction to the top surface of the saddle-shaped bistable plate and each pole is uniformly spaced in circumferential direction of that. Both side of wire is kinematically coupled with one end of the rigid pole. Similarly, the other end of that is also kinematically coupled with the saddle-shaped bistable plate.

The selected elements for each wire were a 2-node beam element B31 and a size of the elements was about 6mm. For each rigid pole, a 2-node 3-D rigid

beam element is used and the elements size is about 5mm. Material properties of wire are summarized in Table 5.2. Although the wire properties below are an artificial quantity, not an experimental quantity, there is no problem in estimating a stroke and a force, which is need to induce the snap-through.

In both Mode state of the saddle-shaped bistable plate (i.e., Mode 1 and Mode 2), since the final curvature are identical to each other, the snap-through load from Mode 1 to Mode 2 cannot help but be same with the snap-through load from Mode 2 to Mode 1. On this basis, one-way snap-through from Mode 1 to Mode 2 was simulated.

For this snap-through analysis, the two wires, which are installed on the three rigid pole, is uniformly heated to 180℃ from room temperature(25℃). As the temperature increase, two wires become more and more contracted as depicted in Figure 5.9(b). Simultaneously, the principal curvature of the saddle-shaped bistable plate decreases. At a certain temperature and at a specific contracted-length of wires, the direction of the principal curvature of the saddle-shaped bistable plate is suddenly changed as shown in Figure 5.9(c). At this snap-through point, the length change of the wire and the reaction force of the wire are measured and these measured quantities are treated as the snap-through stroke and the snap-through force respectively, which are needed to induce the snap-through of the saddle-shaped bistable plate. The results are summarized in Table 5.3.

In this result, the snap-through stoke is relatively large compared with the initial length of the wire (i.e. 81.6mm). In this snap-thorough method, an actuator, which can satisfy the corresponding snap-through stroke and snap-through force, is a SMA spring, not a SMA wire and a piezo material due to the relatively small recovery strain and displacement [54]. For this reason, in this study, SMA spring was selected as the actuator to induce the snap-through of the saddle-shaped bistable plate.

To achieve the snap-through of the saddle-shaped bistable plate by using SMA spring, the recovery force and recovery displacement of SMA spring must satisfy the snap-through force, $F_{\text{snap-thorugh}}$ and the critical length, L'. If spring constant of SMA spring at pure Austenite/Martensite state is known, we can achieve the snap-through of saddle-shaped bistable plate by selecting a proper initial length of SMA spring

It should be noted that if the initial length of SMA spring, L_{M0} which is installed on the saddle-shaped bistable plate is too short, the reaction force of SMA spring could exceed the snap-through load, and overall system might become unstable state although initial state of the saddle-shaped bistable plate lies on stable state. To avoid this, following stable condition must be satisfied, which is represented by in Eq. (5.12). On the other hand, if the initial length of SMA spring, L_{M0} is too long, recovery force of SMA spring could be lower than the snap-through load or the length of fully transformed SMA spring, L_A

could be lower than critical length. As a result, the snap-through could become impossible. To induce the snap-through, following actuation condition must be satisfied, which is represented by in Eq. (5.12).

$$F_{\text{snap-thorugh}} > K_M \left[L_{M0} - L' \right] \tag{5.12}$$

, where, K_M refer to the spring constant at pure Martensite state.

$$F_{\text{snap-thorugh}} < K_A \left[L' - L_{A0} \right] = K_A \left[L' - L(1-\varepsilon) L_{M0} \right], \quad 0 < \left[L' - L_{A0} \right] \tag{5.13}$$

, where, K_A refer to the spring constant at pure Austenite state and ε is the equivalent maximum transformation strain of SMA spring.

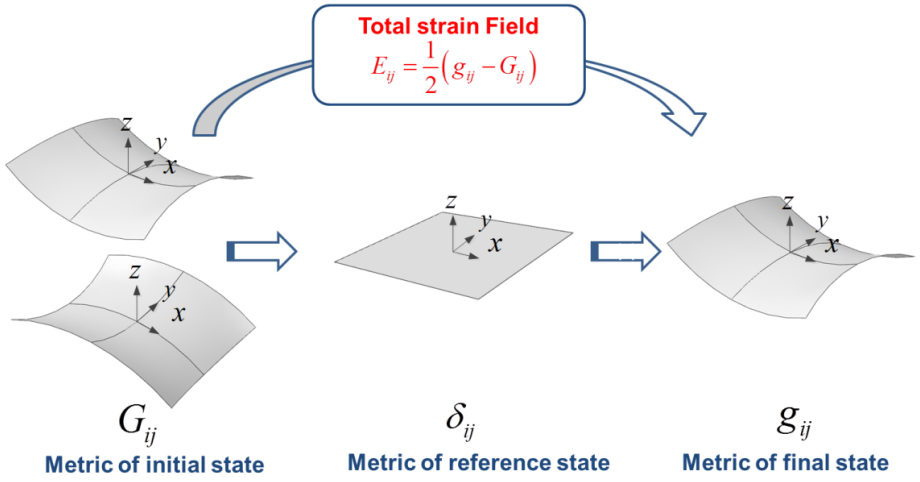

Figure 5.1 Definition of reference state to handle the strain of saddle-shaped bi-stable panel

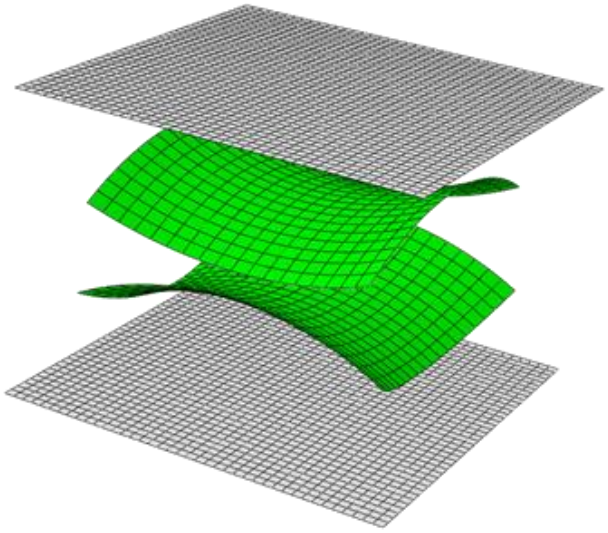

Figure 5.2 Strategic constitution of FE model for inducing the saddle-shaped bi-stable panel

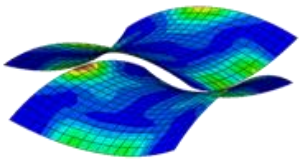

(a) Pressing

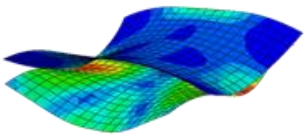

(b) Contact propagation

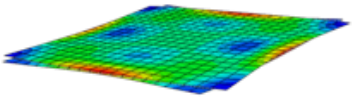

(c) Flattening and bonding

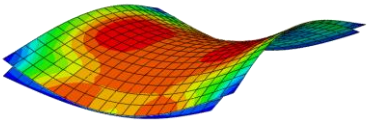

(d) After relaxation:1st stable state

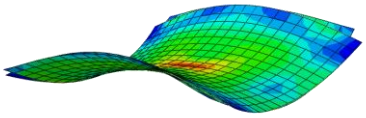

(e) After snap-through:2st stable state

Figure 5.3 The generation process of saddle-shaped bi-stable panel and the simulated snap-through process of 150mm x 150mm saddle panel: (a), (b) and (c) pre-stressing process, (d) after relaxation process, (e) after snap-through process

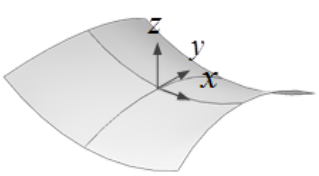

(a)

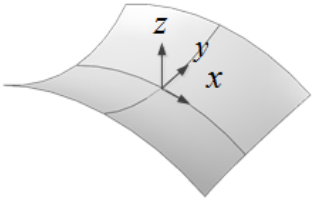

(b)

Figure 5.4 Two possible configurations of the saddle shaped bi-stable panel: (a) Mode 1: $\kappa_{xx} > 0, \kappa_{yy} < 0$, (b) Mode 2: $\kappa_{xx} < 0, \kappa_{yy} > 0$

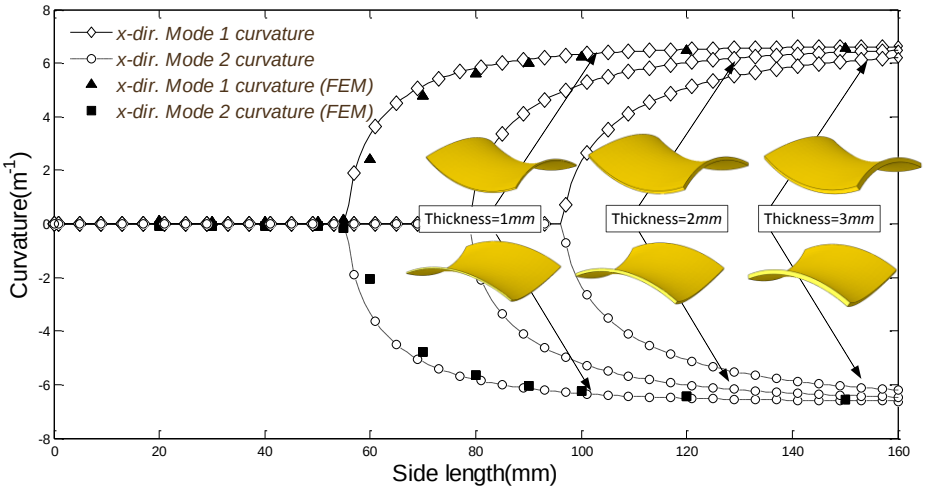

Figure 5.5 Change of x-dir. curvature change with respect to the side-length and thickness for saddle-shaped bi-stable panel with initial curvature, 6.667 m^{-1}

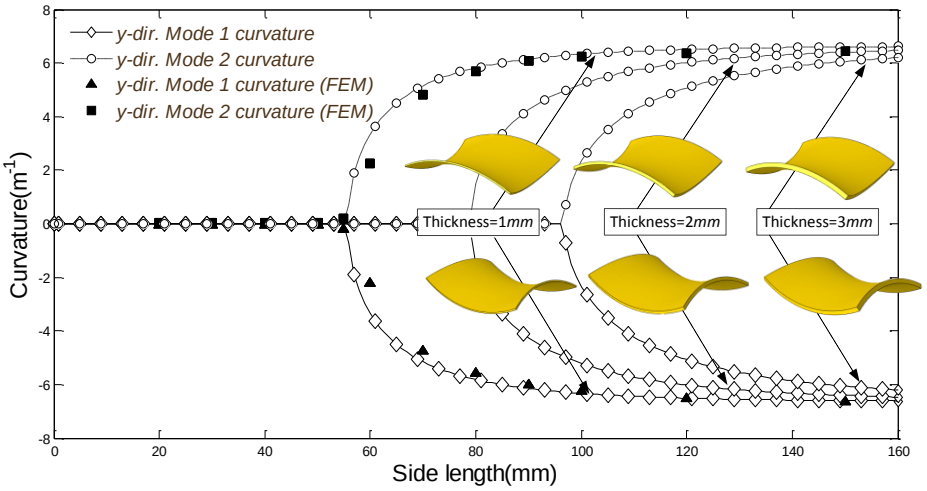

Figure 5.6 Change of y-dir. curvature change with respect to the side-length and thickness for saddle-shaped bi-stable panel with initial curvature, 6.667 m^{-1}

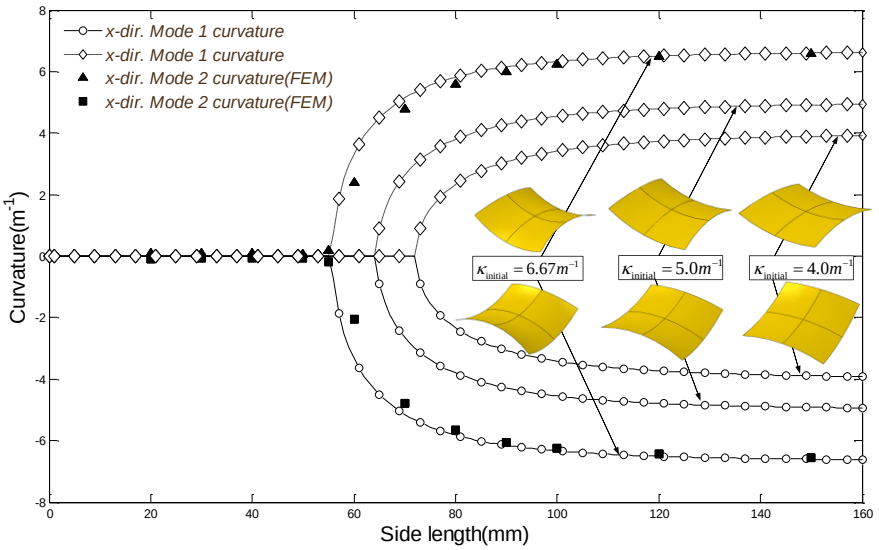

Figure 5.7 Change of x-dir. curvature change with respect to the side-length for saddle-shaped bi-stable panel with different initial curvature

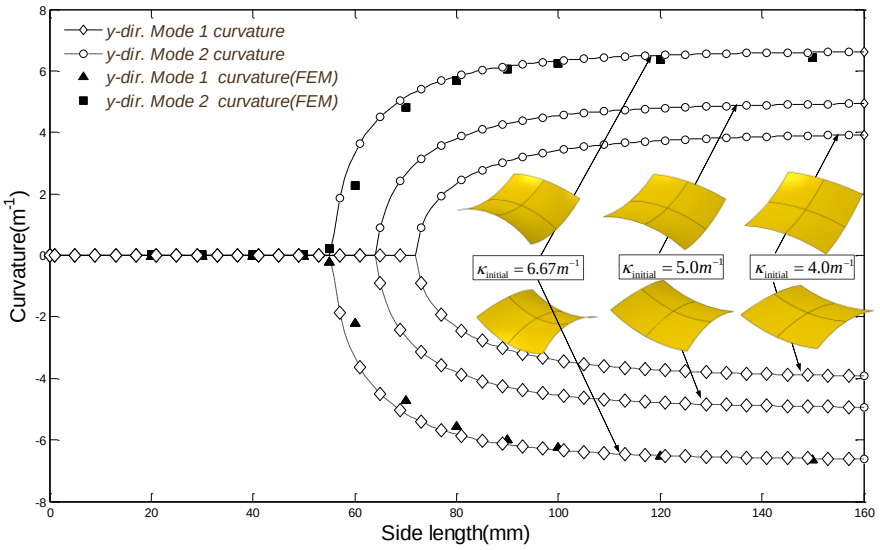

Figure 5.8 Change of y-dir. curvature change with respect to the side-length for saddle-shaped bi-stable panel with different initial curvature

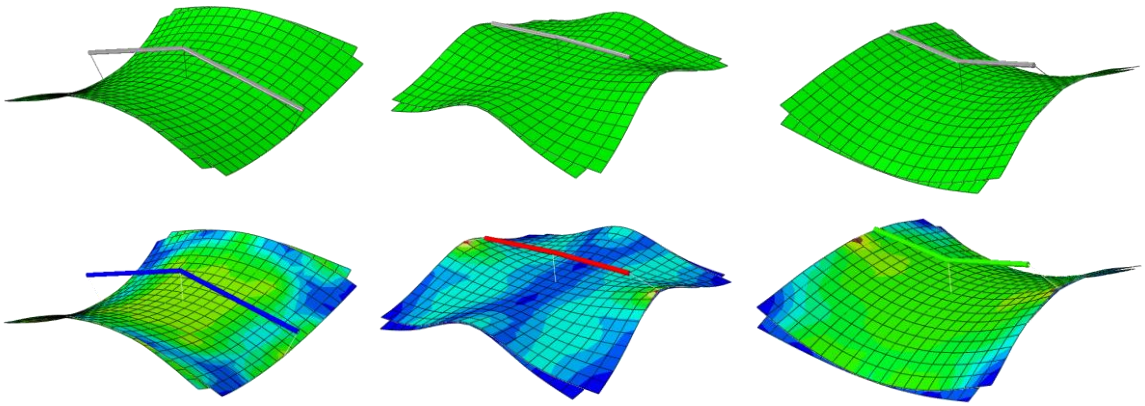

(a) Before snap-through (b) During snap-through (c) After snap-through

Figure 5.9 Simulated snap-through process of saddle-shaped bi-stable panel by thermal contraction of wire

Table 5.1 Material properties of plate

Property	Value
Elastic modulus (MPa)	1.8
Poisson's Ratio (v)	0.3
Thickness (mm)	1

Table 5.2 SMA Wire Material Properties

Property	Value
Elastic modulus (GPa)	35
Thermal expansion coefficient ($℃^{-1}$)	-0.005
Poisson's Ratio (v)	0.3
Diameter (mm)	0.6

Table 5.3 Necessary condition for the snap-through action of the saddle-shaped bi-stable panel

Critical quantity	Value
Snap-through load (N)	0.0965
Snap-through stroke (mm)	27.5

Chapter 6

Analysis of saddle shape bistable structure with arbitrary strain field

6.1 Introduction

In previous chapter 5, the final curvature is assumed only by constant value. However, the real curvature field of bistable structure dose not only involves the constant value. Moreover, in order to analyze and design bistable structure with more complex shape, not merely cylindrical shape or saddle shape, high order strain or curvature field is needed. For this reason, in this chapter, analysis of saddle shape bistable is performed by high order approximation of strain field. The assumed strain field must satisfy the compatibility condition to guarantee the unique solution (i.e. displacement field). Generally, mid-plane normal strains ε_x^o and ε_y^o can be easily assumed without specific constraint, however, mid-plane shear strain γ_{xy}^o must be consistent with the mi-plane normal strains to satisfy the compatibility condition. To keep consistency, the mid-plane shear strain is determined from mid-plane shear strain-displacement relation. This

assumption process of strain field involves other tiresome works, i.e. integration of assumed mid-plane strain field and re-differentiation of the integrated stain field to substitute mid-plane shear strain-displacement relation. Due to this tiresome works, the analyses based on the strain field have not taken center stage under the spotlight of mechanical field. In order to overcome the drawback of classical analysis method based on the strain field, compatibility condition is added to the arbitrary assumed strains implicitly by using Lagrange multiplier without the tiresome work. Firstly, its bistability and final shapes are investigated by means of the Rayleigh-Ritz approximation method. The results obtained by analytical method are compared with increasing the order of strain field.

6.2 Compatibility equation in large deflection

In linear elastic plane stress problem, stain is defined by linear strain-displacement relation [57], as denoted by Eq. (6.1).

$$\varepsilon_{xx}^{o} = \frac{\partial u}{\partial x}, \quad \varepsilon_{yy}^{o} = \frac{\partial v}{\partial y}, \quad \gamma_{xy}^{o} = \frac{\partial u}{\partial y} + \frac{\partial v}{\partial x} \tag{6.1}$$

This linear strain-displacement relation satisfies the following compatibility condition:

$$\frac{\partial^2 \varepsilon_{xx}^{o}}{\partial y^2} + \frac{\partial^2 \varepsilon_{yy}^{o}}{\partial x^2} - \frac{\partial^2 \gamma_{xy}^{o}}{\partial x \partial y} = 0 \tag{6.2}$$

However, for the analysis of bistable structure, mid-plane strain part of von Karman nonlinear strain measures are utilized as denoted by Eq. (6.3).

$$\varepsilon_{xx}^{o}=\frac{\partial u}{\partial x}+\frac{1}{2}\left(\frac{\partial w}{\partial x}\right)^{2},\quad \varepsilon_{yy}^{o}=\frac{\partial v}{\partial y}+\frac{1}{2}\left(\frac{\partial w}{\partial y}\right)^{2},\quad \gamma_{xy}^{o}=\frac{\partial u}{\partial y}+\frac{\partial v}{\partial x}+\frac{\partial w}{\partial x}\frac{\partial w}{\partial y} \tag{6.3}$$

The compatibility corresponding to mid-plane strain part of the von-Karman nonlinear strain can be obtained by substituting the strain components into Eq. (6.2). Accordingly, the compatibility equation can be expressed as Eq. (6.4) [57].

$$\begin{aligned}\frac{\partial^2}{\partial y^2}\left(\frac{\partial u}{\partial x}+\frac{1}{2}\left(\frac{\partial w}{\partial x}\right)^2\right)+\frac{\partial^2}{\partial x^2}\left(\frac{\partial v}{\partial y}+\frac{1}{2}\left(\frac{\partial w}{\partial y}\right)^2\right)-\frac{\partial^2}{\partial x\partial y}\left(\frac{\partial u}{\partial y}+\frac{\partial v}{\partial x}+\frac{\partial w}{\partial x}\frac{\partial w}{\partial y}\right)\\ =\left(\frac{\partial^2 w}{\partial x\partial y}\right)^2-\frac{\partial^2 w}{\partial x^2}\frac{\partial^2 w}{\partial y^2}\end{aligned} \tag{6.4}$$

This compatibility equation can re-expressed from definition of curvature as follow:

$$\frac{\partial^2 \varepsilon_{xx}^{o}}{\partial y^2}+\frac{\partial^2 \varepsilon_{yy}^{o}}{\partial x^2}-\frac{\partial^2 \gamma_{xy}^{o}}{\partial x\partial y}=\left(\kappa_{xy}\right)^2-\kappa_{xx}\kappa_{yy} \tag{6.5}$$

In the work of Dano and Hyer (2002), mid-plane normal strains $\varepsilon_x^o, \varepsilon_y^o$ and deflection w are assumed. Mid-plane shear strain γ_{xy}^o is determined from mid-plane shear strain-displacement relation to satisfy the compatibility condition. This assumption process of strain field involves other tiresome works, i.e. integration of assumed mid-plane strain field and re-differentiation of the integrated stain field to substitute mid-plane shear strain-displacement relation.

However, in this work, among of the non-linear strain-displacement, linear mid-plane strain part, $\varepsilon_{xx}^{u} = \frac{\partial u}{\partial x}$, $\varepsilon_{yy}^{v} = \frac{\partial v}{\partial y}$ and $\gamma_{xy}^{u,v} = \frac{\partial u}{\partial y} + \frac{\partial v}{\partial x}$, and deflection, w, are independently assumed. In addition to linear mid-plane strain, deflection w is also assumed independently.

If displacement field, u,v and w, are assumed independently, the compatibility equation automatically holds. However, as mentioned above, if strain field and deflection field are assumed independently, there is no guarantee that the strain field and deflection field satisfy the compatibility equation (i.e. Eq. (6.4)). In other words, in order to assure the unique solution, the assumed strain field and deflection field must satisfy the compatibility equation. For this, if the strain and deflection is treated as independent variable; and is substituted into the compatibility equation, reduced compatibility equation can be reduced as simple form as expressed in Eq. (6.6), where the detail derivation procedure is listed in Appendix C.

$$\frac{\partial^2 \varepsilon_{xx}^{u}}{\partial y^2} + \frac{\partial^2 \varepsilon_{yy}^{v}}{\partial x^2} - \frac{\partial^2 \gamma_{xy}^{u,v}}{\partial x \partial y} = 0 \tag{6.6}$$

The strain field and deflection field is assumed as polynomial function with two variable x and y. If maximum approximated polynomial orders, p, is selected, the approximated polynomial function of strains and deflection can be expressed as follow:

$$
\begin{aligned}
\varepsilon_{xx}^{u}(x,y) &= \frac{\partial u}{\partial x} = \sum_{i=0}^{p}\sum_{j=0}^{i} e_m x^{i-j} y^{j} \\
\varepsilon_{yy}^{v}(x,y) &= \frac{\partial v}{\partial y} = \sum_{i=0}^{p}\sum_{j=0}^{i} g_m x^{i-j} y^{j} \\
\gamma_{xy}^{u,v}(x,y) &= \frac{\partial u}{\partial y} + \frac{\partial v}{\partial x} = \sum_{i=0}^{p}\sum_{j=0}^{i} f_m x^{i-j} y^{j} \\
w(x,y) &= \sum_{i=0}^{p}\sum_{j=0}^{i} w_m x^{i-j} y^{j}
\end{aligned}
\tag{6.7}
$$

where, $m = \frac{i(i+1)}{2} + j$ and its maximum value is $\frac{p^2+3p}{2} + j$.

If the assumed polynomial strain field function is substituted into the reduced compatibility equation (i.e. Eq. (6.6)). The compatibility equation can be expressed as polynomial form as denoted in re-expressed as Eq. (6.8).

$$
\left(\sum_{i=0}^{p-2}\sum_{j=0}^{i} A^{yy} e_{a^{yy}} x^{i-j} y^{j}\right) + \left(\sum_{i=0}^{p-2}\sum_{j=0}^{i} A^{xx} g_{a^{xx}} x^{i-j} y^{j}\right) - \left(\sum_{i=0}^{p-2}\sum_{j=0}^{i} A^{xy} f_{a^{xy}} x^{i-j} y^{j}\right) = 0 \tag{6.8}
$$

where, A^{xx}, A^{yy}, A^{xy}, a^{xx}, a^{yy} and a^{xy} is defined as follow:

$$
\begin{aligned}
A^{yy} &= 2 + (j+3)\, j, & a^{yy} &= \frac{(i+3)(i+4)}{2} + (j-1) \\
A^{xx} &= 2 + (i+3) i - (j+3)\, j, & a^{xx} &= \frac{(i+3)(i+4)}{2} + (j-3) \\
A^{xy} &= (i+1-j)(j+1), & a^{xy} &= \frac{(i+3)(i+4)}{2} + (j-2)
\end{aligned}
\tag{6.9}
$$

6.3 Strain-based Rayleigh-Ritz analysis model considering compatibility condition

In this section, we develop the strain-based Rayleigh-Ritz analysis model considering compatibility condition. Strains field and deflection field is assumed as two variable polynomial function as denoted in Eq. (6.7).

6.3.1 Strain field of saddle-shaped bistable structure

Von-Karman nonlinear strain is defined as follow:

$$\begin{bmatrix} \varepsilon_{xx} \\ \varepsilon_{yy} \\ \gamma_{xy} \end{bmatrix} = \begin{bmatrix} \varepsilon_{xx}^{o} \\ \varepsilon_{yy}^{o} \\ \gamma_{xy}^{o} \end{bmatrix} + z \begin{bmatrix} \kappa_{xx}^{w} \\ \kappa_{yy}^{w} \\ 2\kappa_{xy}^{w} \end{bmatrix} = \begin{bmatrix} \underbrace{\frac{\partial u}{\partial x}}_{\varepsilon_{xx}^{u}} + \underbrace{\frac{1}{2}\left(\frac{\partial w}{\partial x}\right)^{2}}_{\varepsilon_{xx}^{w}} \\ \underbrace{\frac{\partial v}{\partial y}}_{\varepsilon_{yy}^{v}} + \underbrace{\frac{1}{2}\left(\frac{\partial w}{\partial y}\right)^{2}}_{\varepsilon_{yy}^{w}} \\ \underbrace{\frac{\partial u}{\partial y} + \frac{\partial v}{\partial x}}_{\gamma_{xy}^{u,v}} + \underbrace{\frac{\partial w}{\partial x}\frac{\partial w}{\partial y}}_{\gamma_{xy}^{w}} \end{bmatrix} - z \begin{bmatrix} \underbrace{\frac{\partial^2 w}{\partial x^2}}_{\kappa_{xx}^{w}} \\ \underbrace{\frac{\partial^2 w}{\partial y^2}}_{\kappa_{yy}^{w}} \\ \underbrace{2\frac{\partial^2 w}{\partial x \partial y}}_{2\kappa_{xy}^{w}} \end{bmatrix} \tag{6.10}$$

As mentioned in Chapter 5, the total strain field of the saddle-shaped bistable structure is represented by the sum of the restrained strain and relaxed strain under assumption of small strain. Firstly, the assumed relaxed strain can be expressed as Eq. (6.11), under the definition of Von-Karman nonlinear strain which based on the assumption of a plane stress state and a thin plate/shell assumption.

$$\begin{Bmatrix} \varepsilon_{xx}^{relax} \\ \varepsilon_{xx}^{relax} \\ \gamma_{xy}^{relax} \end{Bmatrix} = \begin{bmatrix} \sum_{i=0}^{p}\sum_{j=0}^{i} e_m x^{i-j} y^j + \frac{1}{2}\left(\sum_{i=0}^{p-1}\sum_{j=0}^{i} A^x w_{a^x} x^{i-j} y^j \right)^2 \\ \sum_{i=0}^{p}\sum_{j=0}^{i} g_m x^{i-j} y^j + \frac{1}{2}\left(\sum_{i=0}^{p-1}\sum_{j=0}^{i} A^y w_{a^y} x^{i-j} y^j \right)^2 \\ \sum_{i=0}^{p}\sum_{j=0}^{i} f_m x^{i-j} y^j + \left(\sum_{i=0}^{p-1}\sum_{j=0}^{i} A^x w_{a^x} x^{i-j} y^j \right)\left(\sum_{i=0}^{p-1}\sum_{j=0}^{i} A^y w_{a^y} x^{i-j} y^j \right) \end{bmatrix} - \begin{bmatrix} \sum_{i=0}^{p-2}\sum_{j=0}^{i} A^{xx} w_{a^{xx}} x^{i-j} y^j \\ \sum_{i=0}^{p-2}\sum_{j=0}^{i} A^{yy} w_{a^{yy}} x^{i-j} y^j \\ \sum_{i=0}^{p-2}\sum_{j=0}^{i} A^{xy} w_{a^{xy}} x^{i-j} y^j \end{bmatrix} z \quad (6.11)$$

where A^x, A^y, a^x and a^y are defined as follow:

$$\begin{aligned} A^x &= (i+1-j), & a^x &= \frac{(i+1)(i+2)}{2} + j \\ A^y &= (j+1), & a^y &= \frac{(i+1)(i+2)}{2} + 1 + j \end{aligned} \quad (6.12)$$

The restrained strain is defined similar with the relaxed strain. However, it should be noted that the restrained strain is divided into a part of upper plate and a part of lower plate, according to the position of plate on the basis of z-axis (i.e., z=0) because the saddle-shaped bistable structure is realized by perfect bonding between face-to-face surfaces of two saddle-shaped plates on stress-free state. The restrained strain are thus given by Eq. (6.13) and (6.14) if the initial saddle shape is represented as Eq. (6.15)

$$\begin{Bmatrix} \varepsilon_{xx}^{restrain} \\ \varepsilon_{yy}^{restrain} \\ \gamma_{xy}^{restrain} \end{Bmatrix}^{(upper)} = -\left(\begin{bmatrix} \\ -\kappa_{xx}^{restrain} \kappa_{yy}^{restrain} xy \end{bmatrix} + \begin{bmatrix} (+)\kappa_{xx}^{restrain} \\ (-)\kappa_{yy}^{restrain} \\ 0 \end{bmatrix} z \right)^{(upper)} \quad (6.13)$$

$$\begin{Bmatrix} \varepsilon_{xx}^{restrain} \\ \varepsilon_{yy}^{restrain} \\ \gamma_{xy}^{restrain} \end{Bmatrix}^{(lower)} = -\left(\begin{bmatrix} \\ -\kappa_{xx}^{restrain} \kappa_{yy}^{restrain} xy \end{bmatrix} + \begin{bmatrix} (-)\kappa_{xx}^{restrain} \\ (+)\kappa_{yy}^{restrain} \\ 0 \end{bmatrix} z \right)^{(lower)} \quad (6.14)$$

$$w^{\text{intial}} = \mp\frac{1}{2}\kappa_{xx}^{\text{restrain}}x^2 \pm \frac{1}{2}\kappa_{yy}^{\text{restrain}}y^2 \tag{6.15}$$

where upper initial saddle shape is corresponding to quadratic polynomial expression with upper sign (i.e., (-) and (+)) and lower initial saddle shape is corresponding to quadratic polynomial expression with lower sign (i.e., (+) and (-)).

Therefore, the total strain field of the saddle-shaped bistable structure is expressed as follow:

$$\begin{Bmatrix}\varepsilon_{xx}\\ \varepsilon_{yy}\\ \gamma_{xy}\end{Bmatrix} = \begin{Bmatrix}\varepsilon_{xx}^{relax}+\varepsilon_{xx}^{restrain}\\ \varepsilon_{yy}^{relax}+\varepsilon_{yy}^{restrain}\\ \gamma_{xy}^{relax}+\gamma_{xy}^{restrain}\end{Bmatrix} = \left\{\begin{bmatrix}\sum_{i=0}^{p}\sum_{j=0}^{i} e_m x^{i-j}y^j + \frac{1}{2}\left(\sum_{i=0}^{p-1}\sum_{j=0}^{i} A^x w_{a^x} x^{i-j}y^j\right)^2\\ \sum_{i=0}^{p}\sum_{j=0}^{i} g_m x^{i-j}y^j + \frac{1}{2}\left(\sum_{i=0}^{p-1}\sum_{j=0}^{i} A^y w_{a^y} x^{i-j}y^j\right)^2\\ \sum_{i=0}^{p}\sum_{j=0}^{i} f_m x^{i-j}y^j + \left(\sum_{i=0}^{p-1}\sum_{j=0}^{i} A^x w_{a^x} x^{i-j}y^j\right)\left(\sum_{i=0}^{p-1}\sum_{j=0}^{i} A^y w_{a^y} x^{i-j}y^j\right)\end{bmatrix} - \begin{bmatrix}\frac{1}{2}\left(\kappa_{xx}^{restrain}x\right)^2\\ \frac{1}{2}\left(\kappa_{yy}^{restrain}y\right)^2\\ -\kappa_{xx}^{restrain}\kappa_{yy}^{restrain}xy\end{bmatrix}\right.$$
$$\left. + \begin{bmatrix}\sum_{i=0}^{p-2}\sum_{j=0}^{i} A^{xx} w_{a^{xx}} x^{i-j}y^j - (\pm)\kappa_{xx}^{restrain}\\ \sum_{i=0}^{p-2}\sum_{j=0}^{i} A^{yy} w_{a^{yy}} x^{i-j}y^j - (\mp)\kappa_{yy}^{restrain}\\ \sum_{i=0}^{p-2}\sum_{j=0}^{i} A^{xy} w_{a^{xy}} x^{i-j}y^j\end{bmatrix} z \right\} \tag{6.16}$$

6.3.2 Total potential energy of saddle-shaped bistable structure

Assuming a plane stress state, the strain energy of saddle shaped bistable structure is expressed as

$$\Pi = \sum_{i=1}^{n} \int_{-\frac{L}{2}}^{\frac{L}{2}} \int_{\frac{L}{2}}^{\frac{L}{2}} \int_{z_i^{low}}^{z_i^{up}} \frac{1}{2} \bar{Q}_{11}^{i} \varepsilon_{xx}^{2} + \frac{1}{2} \bar{Q}_{22}^{i} \varepsilon_{yy}^{2} + \bar{Q}_{12}^{i} \varepsilon_{xx} \varepsilon_{yy} + \frac{1}{2} \bar{Q}_{66}^{i} \gamma_{xy}^{2} dz dx dy \tag{6.17}$$

where $\bar{Q}_{\alpha\beta}^{i}$ is the transformed plane-stress reduced stiffness of the i-th layer; L is the side length of the composites; and z_i^{up} and z_i^{low} denote the positions of the upper surface and lower surface, respectively, corresponding to the i-th layer. The strain energy function is derived from the assumed strain field. Therefore, the compatibility condition must be satisfied to assure the unique strain field. For this reason, compatibility condition is considered by treating as constrain condition which conjugates to the Lagrange multiplier Λ, as expressed in Eq. (6.18).

$$\Pi^{*} = \Pi + \Lambda \left\{ C_{p-2} \right\} \tag{6.18}$$

where Π^{*} is the total potential energy and Π is the strain energy of the bistable composite and $C_{\text{p-2}}$ is the polynomial form compatibility function which is expressed in Eq. (6.8) with p-2 polynomial order.

6.3.3 Minimization of total potential energy

The first variation of the total potential energy, $\delta\Pi^*$, should be equal to zero to ensure the existence of a solution. The requirement for the existence of a solution is given as follows:

$$\delta\Pi^* = \left(\frac{\partial\Pi^*}{\partial\varepsilon_{xx}^{u(relax)}}\right)\delta\varepsilon_{xx}^{u(relax)} + \left(\frac{\partial\Pi^*}{\partial\varepsilon_{yy}^{v(relax)}}\right)\delta\varepsilon_{yy}^{v(relax)} + \left(\frac{\partial\Pi^*}{\partial\gamma_{xy}^{u,v(relax)}}\right)\delta\gamma_{xy}^{u,v(relax)} + \left(\frac{\partial\Pi^*}{\partial w^{relax}}\right)\delta w^{relax} + \left(\frac{\partial\Pi^*}{\partial\Lambda}\right)\delta\Lambda = 0 \quad (6.19)$$

Eq. (6.19) is a compilation of nonlinear algebraic equations. In order to solve these nonlinear algebraic equations, The Newton-Raphson iterative method was used. At first iteration, an initial solution was assumed as a saddle shape. At next iteration, a subsequent solution was considered as the initial solution. The second variation of total potential energy (i.e., jacobian) was obtained by complex derivative method [58].

6.4 Verification and analysis results

In order to verify the developed analytical model, Rayleigh-Ritz analysis is performed by minimizing total potential energy of saddle shaped bistable structure with a different polynomial orders, *p* of strain field and deflection field. Since the deflection field dose not contribute the compatibility condition as shown in Eq. (6.6) and (6.8). The polynomial order of strain field can be selected differently with that of deflection field. For this reason, in the verification of the developed analytical model, the polynomial order of strain

field is considered independently with that of deflection. Firstly, analysis is performed based on the strain field of zero order polynomial approximation and the deflection field of from 2-nd to 6-th order polynomial approximation as shown in Figure 6.1. In the result, the bistability of structure is well obtained regardless of order of polynomial approximation. Afitinally, final shape of saddle-shape bistable structure on x-directional or y-directional is almost identical to the each other regardless of the polynomial approximation order. Similarly, final curvature is almost identical to the each other although the curve of final curvature is a little bit different at the both end of side-length. This trend of the result last through the 3-rd order polynomial approximation of strain field while keep the order polynomial approximation of deflection field from 2-nd to 6-th order as shown in Figure 6.2, 6.3 and 6.4. However, the final curvature dispersion dramatically changes into nearly quadratic curved line when the strain field is assumed as 4-th order polynomial function as shown in Figure 6.5. This quadratic curved line of curvature dispersion begins to appear when approximating the deflection field as 4-th order polynomial function. On the other hand, the curvature dispersion does not change any more from 4-th order polynomial function of deflection field. Similarly, as shown in Figure 6.6, the final curvature dispersion dramatically changes twice when the strain field is assumed as 6-th order polynomial function. When approximating the deflection field as 4-th order polynomial function, a quadratic curved line of curvature dispersion begins to appear. When approximating the deflection field

as 4-th order polynomial function, a quartic curved line of curvature dispersion begin to appear. On the other hand, the curvature dispersion does not change any more from 6-th order polynomial function of deflection field. This result means that the order of polynomial function of strain field and deflection field need to be identical to each other in other to obtain the optimized solution without redundant computational analysis. From this analysis with increasing the polynomial approximation order of strain field and deflection field, the developed model is verified and the proper usage guide-line of the developed model is suggested.

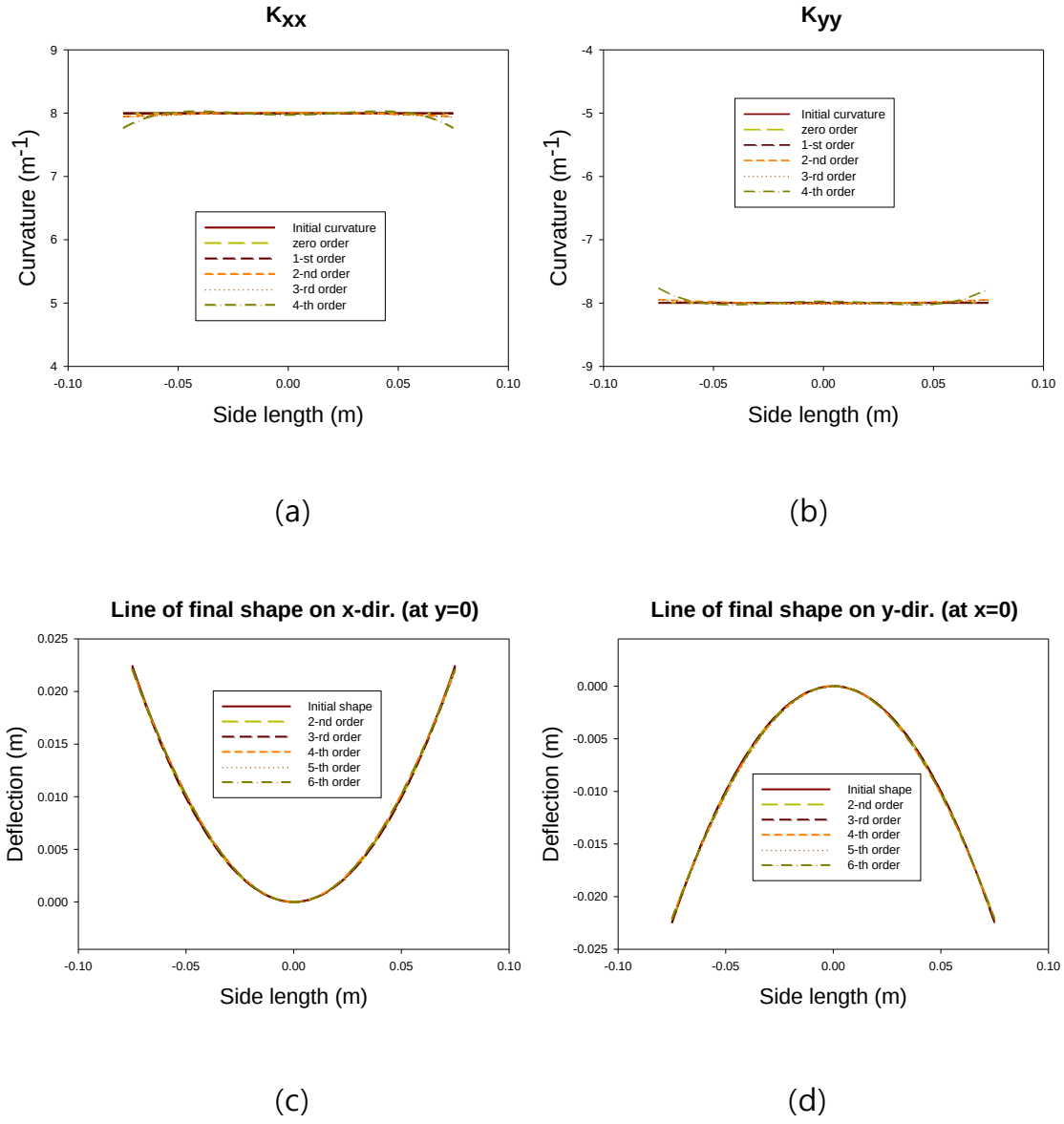

Figure 6.1 Simulation result based on the strain field of zero order polynomial approximation and the deflection field of 2-nd ~ 6-th order polynomial approximation: (a) x-directional curvature and (c) deflection along the side-length (at y=0); (b) y-directional curvature and (d) deflection along the side-length (at x=0)

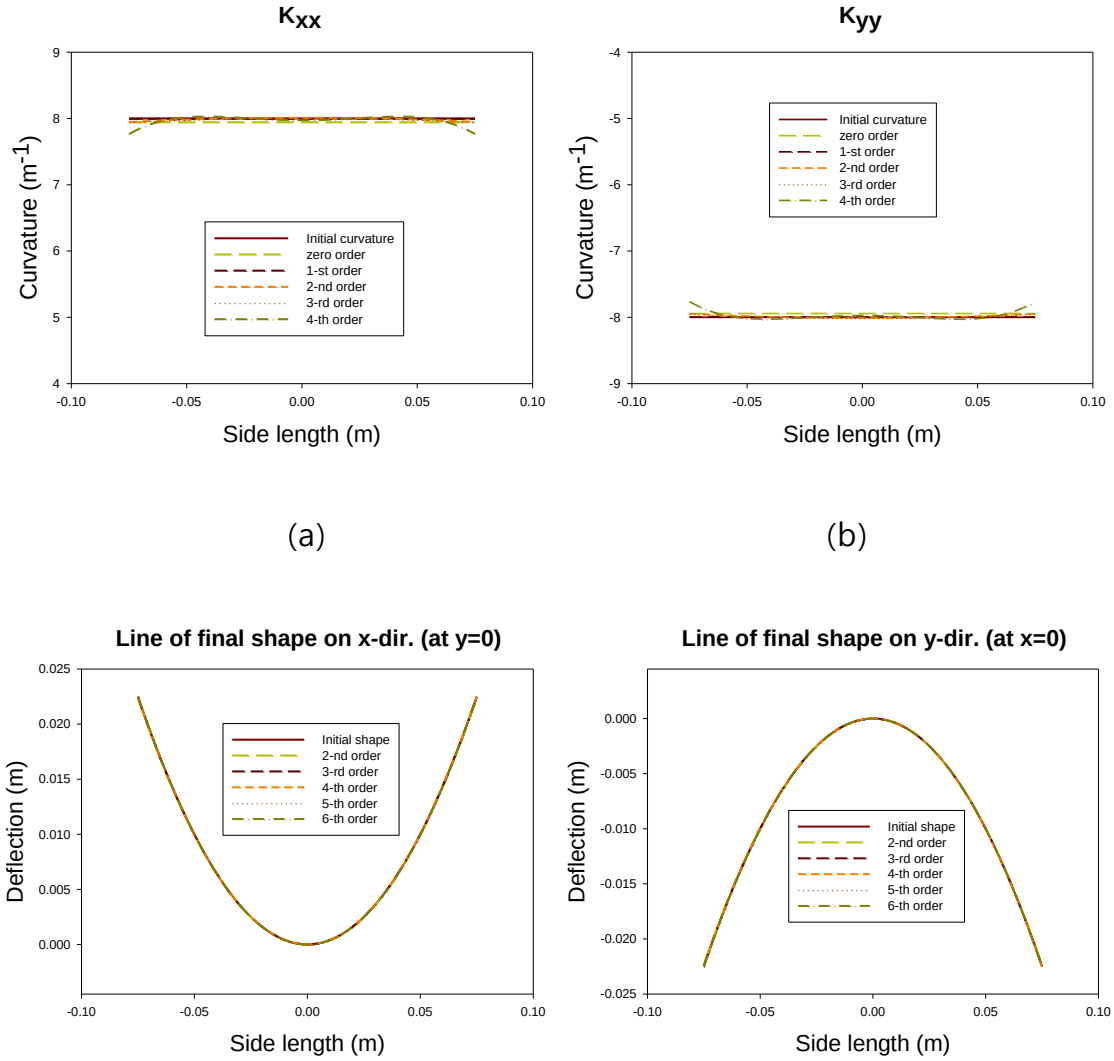

Figure 6.2 Simulation result based on the strain field of 1-st order polynomial approximation and the deflection field of 2-nd ~ 6-th order polynomial approximation: (a) x-directional curvature and (c) deflection along the side-length (at y=0); (b) y-directional curvature and (d) deflection along the side-length (at x=0)

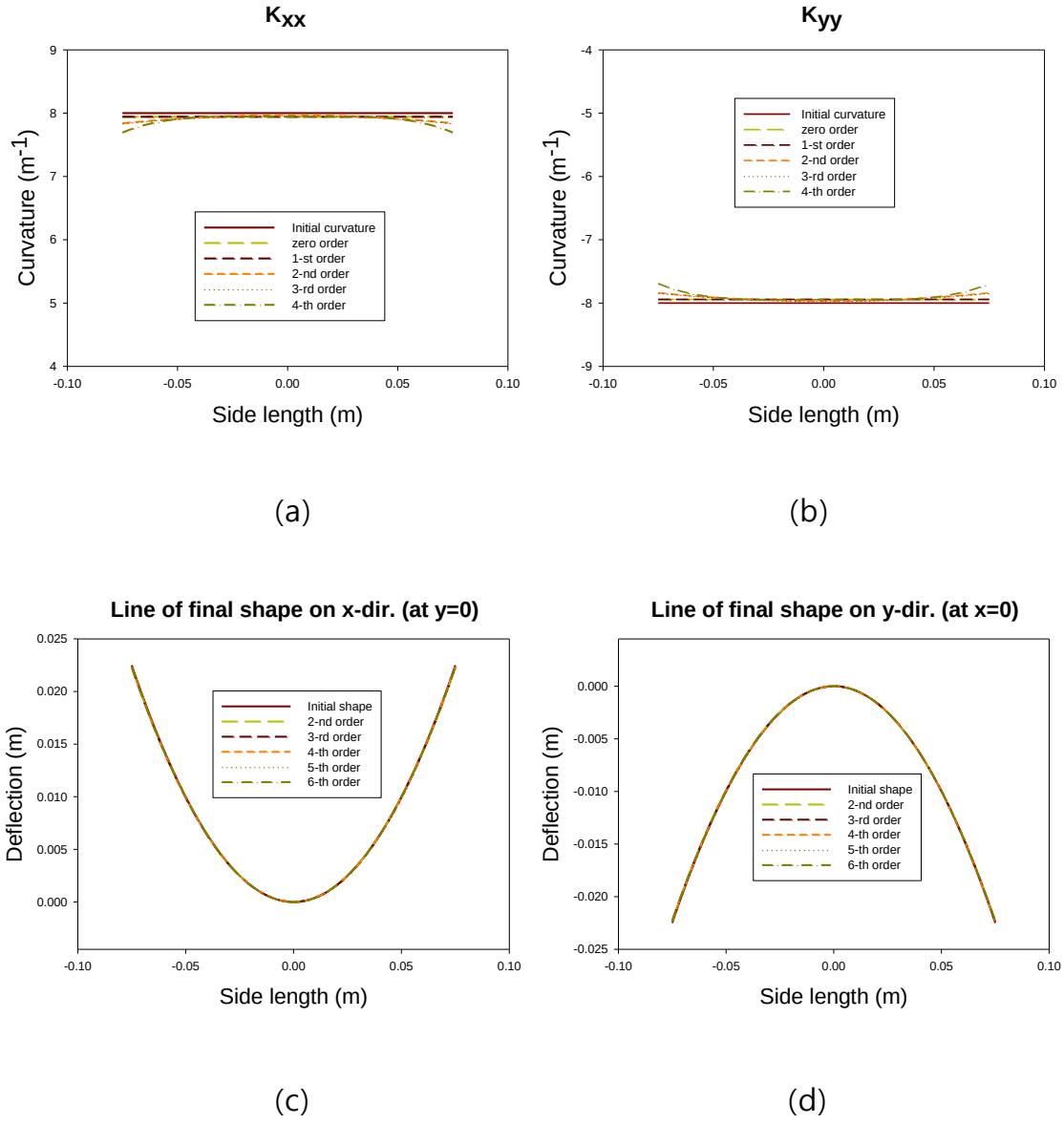

Figure 6.3 Simulation result based on the strain field of 2-nd order polynomial approximation and the deflection field of 2-nd ~ 6-th order polynomial approximation: (a) x-directional curvature and (c) deflection along the side-length (at y=0); (b) y-directional curvature and (d) deflection along the side-length (at x=0)

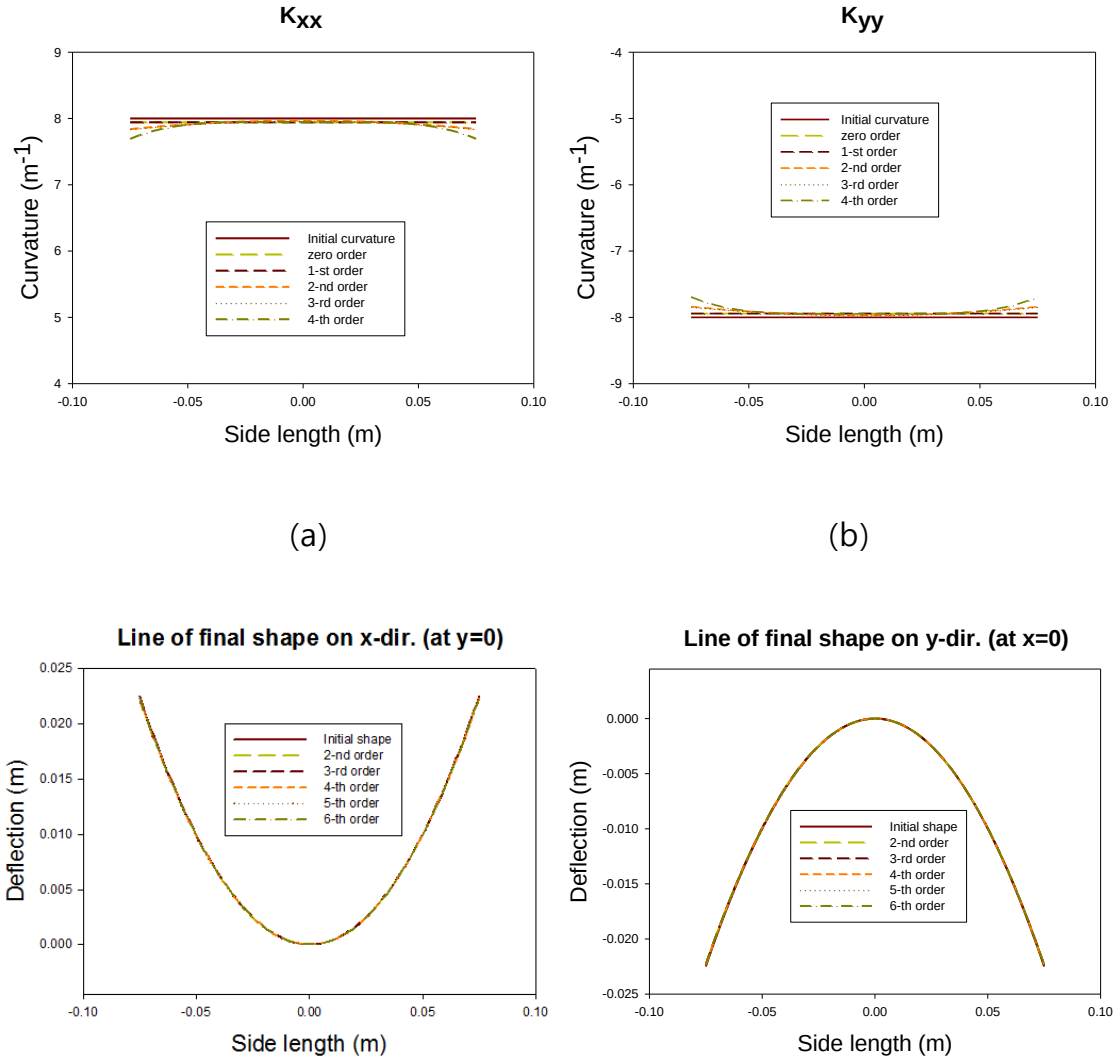

Figure 6.4 Simulation result based on the strain field of 3-rd order polynomial approximation and the deflection field of 2-nd ~ 6-th order polynomial approximation: (a) x-directional curvature and (c) deflection along the side-length (at y=0); (b) y-directional curvature and (d) deflection along the side-length (at x=0)

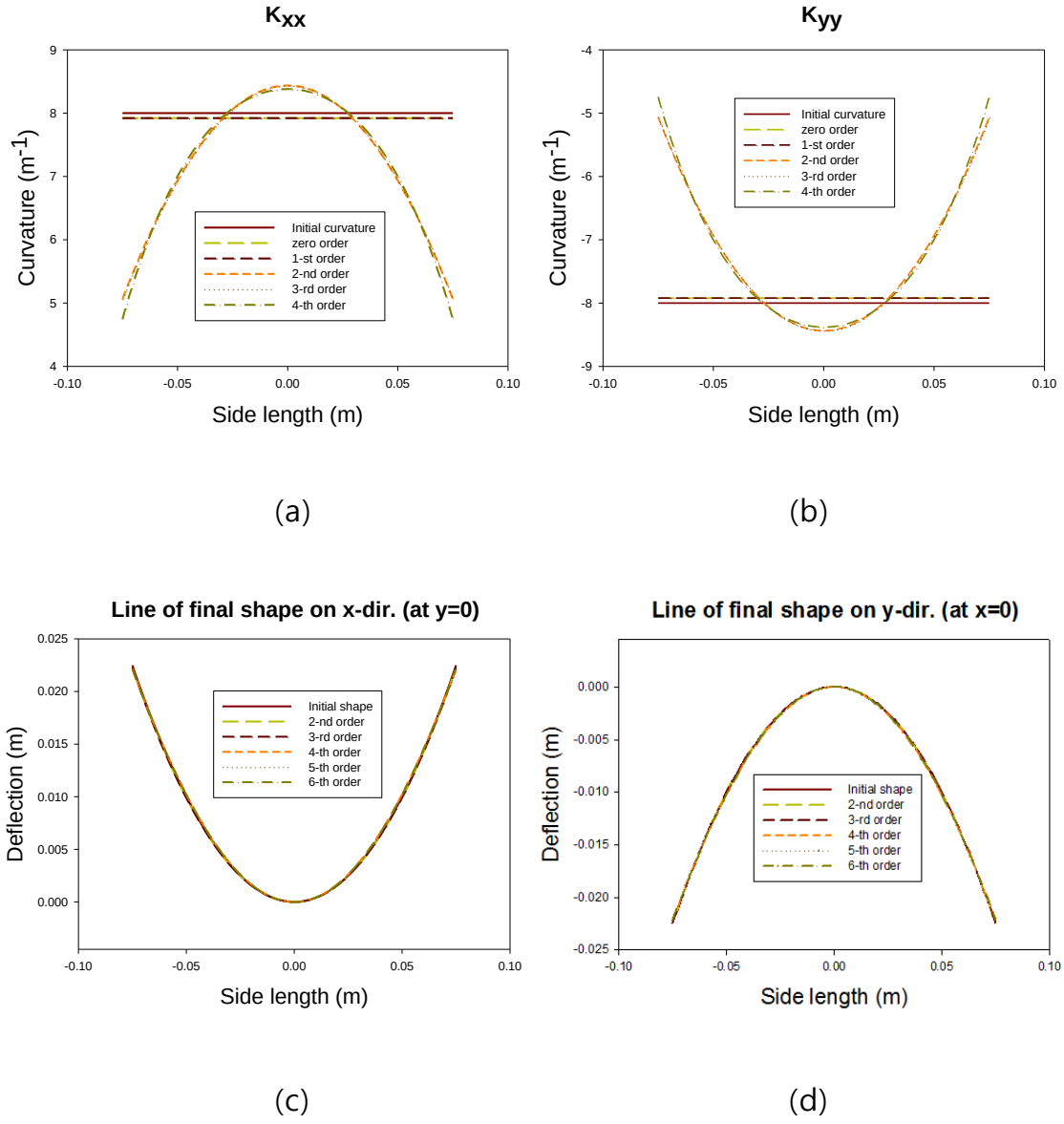

Figure 6.5 Simulation result based on the strain field of 4-th order polynomial approximation and the deflection field of 2-nd ~ 6-th order polynomial approximation: (a) x-directional curvature and (c) deflection along the side-length (at y=0); (b) y-directional curvature and (d) deflection along the side-length (at x=0)

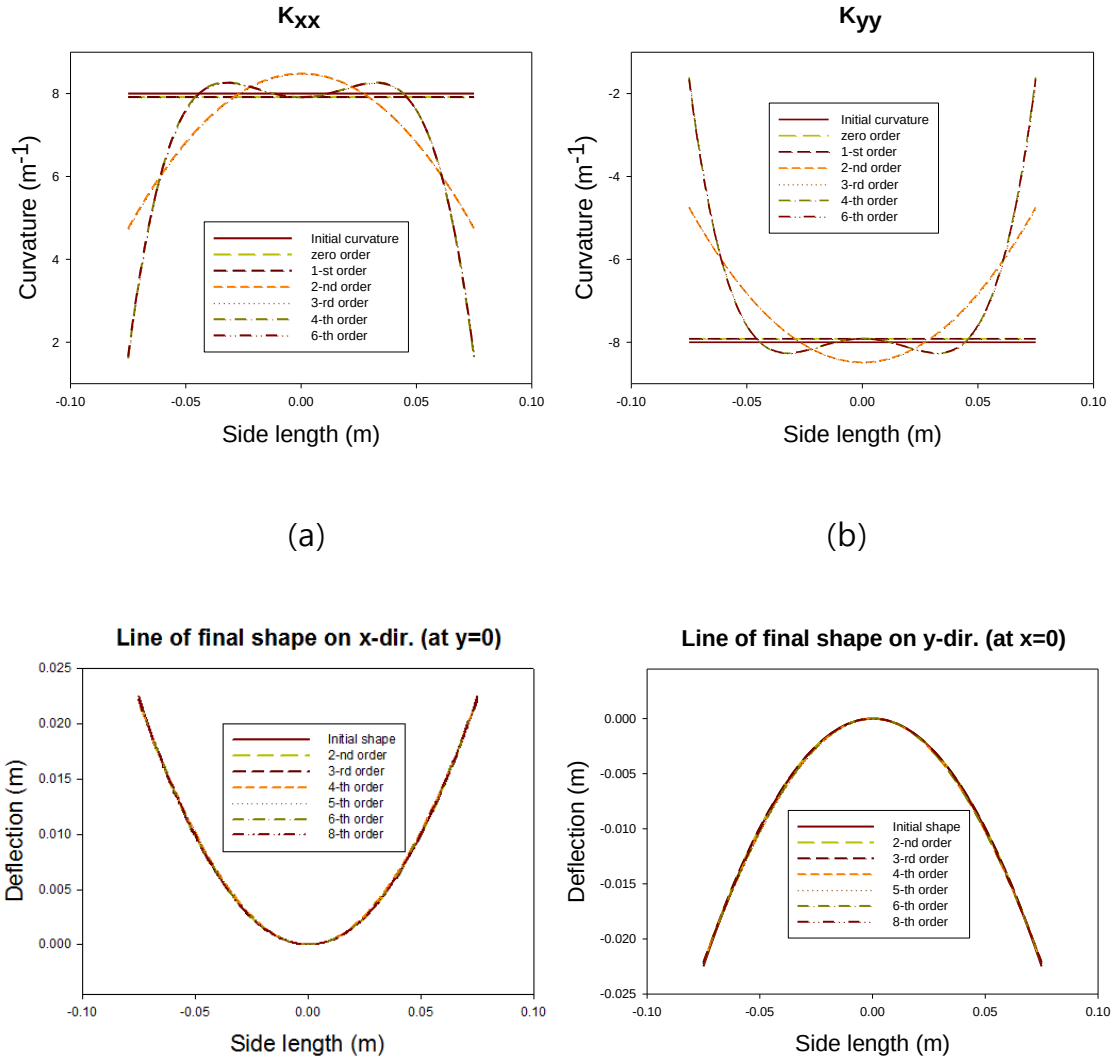

Figure 6.6 Simulation result based on the strain field of 6-th order polynomial approximation and the deflection field of 2-nd ~ 8-th order polynomial approximation: (a) x-directional curvature and (c) deflection along the side-length (at y=0); (b) y-directional curvature and (d) deflection along the side-length (at x=0)

Chapter 7

Saddle shape bistable structure with large curvature

7.1 Introduction

In previous chapter, the analysis of saddle shape bistable structure was performed. However, the previous model was developed based on the von Karman nonlinear strain measure. Specifically, the curvature of von Karman nonlinear strain is expressed as the second order derivative of deflection (i.e. $\kappa_{xx} = \frac{\partial^2 w}{\partial x^2}, \kappa_{yy} = \frac{\partial^2 w}{\partial y^2}$ and $\kappa_{xy} = \frac{\partial^2 w}{\partial xy}$). This curvature expression is only valid in the case of structure with small curvature. Therefore, if the bistable structure, which has a large curvature, is analyzed by using the previous model, we cannot guarantee an accuracy solution. In chapter 6, this model is advanced by changing the previous strain field to Lagrange strain which is defined in thin shell theory. Similar to the previous chapter, firstly, its bistability and final shapes are investigated by means of the Rayleigh-Ritz approximation method and FEM. The results obtained by analytical method and by FEM are compared to the each other.

7.2 Review of thin shell theory

In this section, the kinematic description of the thin shell is reviewed and then Lagrange strain is introduced for consisting of strain energy of saddle shape structure.

7.2.1 Curvilinear coordinate system

In the assumption of a shell with uniform thickness h, the domain of undeformed shell is represented as $\overline{\Omega} = \overline{\omega} \times \left(\frac{-h}{2}, \frac{h}{2}\right) \subset \mathbb{R}^3$ with the midplane$\overline{\omega} \subset \mathbb{R}^2$. Similarly, the domain of deformed shell is represented as $\Omega = \omega \times \left(\frac{-h}{2}, \frac{h}{2}\right) \subset \mathbb{R}^3$ with the mid-surface $\omega \subset \mathbb{R}^2$. If we introduce a curvilinear coordinate system (ξ_1, ξ_2), the position vector of material particle on the midplane of undeformed and deformed shell $\overline{\omega}$ and ω can be easily parameterized or denoted by $\bar{\mathbf{r}}(\xi_1, \xi_2)$ and $\mathbf{r}(\xi_1, \xi_2)$ respectively[59, 60], as shown in Figure 7.1.

In the the midplane of undeformed and deformed shell $\overline{\omega}$ and ω, the orientation of an arbitrary point are characterized as following three basis vectors $(\overline{\mathbf{m}}_1, \overline{\mathbf{m}}_2, \overline{\mathbf{m}}_3)$ and $(\mathbf{m}_1, \mathbf{m}_2, \mathbf{m}_3)$:

$$\bar{\mathbf{m}}_\alpha = \frac{\partial \bar{\mathbf{r}}}{\partial \xi_\alpha}, \qquad \bar{\mathbf{m}}_3 = \frac{\bar{\mathbf{m}}_1 \times \bar{\mathbf{m}}_2}{|\bar{\mathbf{m}}_1 \times \bar{\mathbf{m}}_2|}, \qquad \mathbf{m}_\alpha = \frac{\partial \mathbf{r}}{\partial \xi_\alpha}, \qquad \mathbf{m}_3 = \frac{\mathbf{m}_1 \times \mathbf{m}_2}{|\mathbf{m}_1 \times \mathbf{m}_2|} \tag{7.1}$$

Among of these basis vector, $(\overline{\mathbf{m}}_1, \overline{\mathbf{m}}_2)$ and $(\mathbf{m}_1, \mathbf{m}_2)$ are tangent vector of the undeformed and deformed mid-plane. Basis vectors $(\overline{\mathbf{m}}_3)$ and $(\mathbf{m}_3)$ are unit normal vector of the undeformed and deformed mid-plane. These basis vectors

($\overline{\mathbf{m}}_1, \overline{\mathbf{m}}_2, \overline{\mathbf{m}}_3$) and ($\mathbf{m}_1, \mathbf{m}_2, \mathbf{m}_3$) are called the covariant basis of coordinate system. Generally, basis vectors are not orthogonal.

For the convenience of vector analysis, it is needed to introduce a conjugate basis vector ($\overline{\mathbf{m}}^1, \overline{\mathbf{m}}^2, \overline{\mathbf{m}}^3$) and ($\mathbf{m}^1, \mathbf{m}^2, \mathbf{m}^3$) so that

$$\overline{\mathbf{m}}^i \cdot \overline{\mathbf{m}}_j = \delta^i_j, \qquad \mathbf{m}^i \cdot \mathbf{m}_j = \delta^i_j \tag{7.2}$$

where δ^i_j indicate the Kronecker delta symbol.

In curvilinear coordinate system, vectors and tensor can be expressed as various forms depend on the selected basis vector. For example, vector $\mathbf{a}$ and tensor $\mathbf{T}$ can be expressed as follow:

$$\mathbf{a} = \overline{a}^i \overline{\mathbf{m}}_i = \overline{a}_i \overline{\mathbf{m}}^i = a^i \mathbf{m}_i = a_i \mathbf{m}^i \tag{7.3}$$

$$\begin{aligned} \mathbf{T} &= T^{ij}\mathbf{m}_i \otimes \mathbf{m}_j = T^i_{.j}\mathbf{m}_i \otimes \mathbf{m}^j = T^{.i}_j \mathbf{m}^j \otimes \mathbf{m}_i = T_{ij}\mathbf{m}^i \otimes \mathbf{m}^j \\ &= \overline{T}^{ij}\overline{\mathbf{m}}_i \otimes \overline{\mathbf{m}}_j = \overline{T}^i_{.j}\overline{\mathbf{m}}_i \otimes \overline{\mathbf{m}}^j = \overline{T}^{.i}_j \overline{\mathbf{m}}^j \otimes \overline{\mathbf{m}}_i = \overline{T}_{ij}\overline{\mathbf{m}}^i \otimes \overline{\mathbf{m}}^j \end{aligned} \tag{7.4}$$

7.2.2 The deformation gradient and Lagrange strain tensor

The position vector $\overline{\mathbf{x}}$ of undeformed shell $\overline{\Omega}$ is expressed as follow:

$$\overline{\mathbf{x}}(\xi_1, \xi_2, \xi_3) = \overline{\mathbf{r}}(\xi_1, \xi_2) + \xi_3 \overline{\mathbf{m}}_3, \quad -\frac{h}{2} \le \xi_3 \le \frac{h}{2} \tag{7.5}$$

The position vector of deformed shell $\overline{\Omega}$ can be approximated by the following

kinematic assumption[61]:

1. The thickness of shell h is much smaller than in-plane dimension of shell.
2. The thickness of shell does not change during deformation
3. Shell director $\bar{\mathbf{m}}_3$ which are normal vector of undeformed midplane remain normal to the deformed midplane after deformation.
4. The straight line which normal to undeformed midplane remain straight after deformation

Through corresponding assumption, the approximated position vector $\mathbf{x}$ of deformed shell Ω is expressed as Eq. (7.6):

$$\mathbf{x}(\xi_1,\xi_2,\xi_3)=\mathbf{r}(\xi_1,\xi_2)+\xi_3\mathbf{m}_3, \quad -\frac{h}{2}\le\xi_3\le\frac{h}{2} \tag{7.6}$$

The deformation gradient $\mathbf{F}$ is defined by the gradient ∇ of deformation $\mathbf{dx}$. From this definition, the deformation gradient can be expressed as follow:

$$\mathbf{F}=\frac{d\mathbf{x}}{d\bar{\mathbf{x}}}=\frac{d\mathbf{x}}{d\xi_i}\frac{d\xi_i}{d\bar{\mathbf{x}}}=\mathbf{x}_{,i}\otimes\bar{\mathbf{m}}_i \tag{7.7}$$

From the definition of deformation gradient and the position vector $\mathbf{x}$ of deformed shell Ω, the deformation gradient can be approximated as follow:

$$\mathbf{F}\approx\mathbf{m}_\alpha\otimes\bar{\mathbf{m}}^\alpha+\xi_3\left(\kappa_\beta^\alpha-\bar{\kappa}_\beta^\alpha\right)\mathbf{m}_\alpha\otimes\bar{\mathbf{m}}^\beta+\mathbf{m}_3\otimes\bar{\mathbf{m}}^3, \qquad \kappa_\beta^\alpha=g^{\alpha\gamma}\kappa_{\gamma\beta} \tag{7.8}$$

where $g^{\alpha\beta}$ is contravariant component of metric tensor for the deformed midplane and $\kappa_{\alpha\beta}$ is covariant component of curvature tensor for the deformed midplane.

The components of metric tensor are calculated as the inner product on the tangent space of a surface (i.e. inner product on the covariant basis vectors of mid-plane surface.) Therefore, the components of metric tensor are calculated and denoted by Eq. (7.9).

$$\begin{aligned} &\bar{g}_{\alpha\beta} = \bar{\mathbf{m}}_\alpha \cdot \bar{\mathbf{m}}_\beta \quad \bar{g}^{\alpha\beta} = \bar{\mathbf{m}}^\alpha \cdot \bar{\mathbf{m}}^\beta \quad \bar{g}^{\alpha}_{.\beta} = \bar{\mathbf{m}}^\alpha \cdot \bar{\mathbf{m}}_\beta = \delta^\alpha_{.\beta} \quad \bar{g}^{.\alpha}_{\beta} = \mathbf{m}_\beta \cdot \mathbf{m}^\alpha = \delta^{.\alpha}_{\beta} \\ &g_{\alpha\beta} = \mathbf{m}_\alpha \cdot \mathbf{m}_\beta \quad g^{\alpha\beta} = \mathbf{m}^\alpha \cdot \mathbf{m}^\beta \quad g^{\alpha}_{.\beta} = \mathbf{m}^\alpha \cdot \mathbf{m}_\beta = \delta^\alpha_{.\beta} \quad g^{.\alpha}_{\beta} = \mathbf{m}_\beta \cdot \mathbf{m}^\alpha = \delta^{.\alpha}_{\beta} \end{aligned} \tag{7.9}$$

Specifically, in differential geometry, the inner products on the tangent space of a undeformed midplane surface $\bar{\mathbf{m}}_\alpha \cdot \bar{\mathbf{m}}_\beta$ are used to represented first fundamental form of a undeformed midplane surface as follow:

$$\begin{aligned} I &= \left(\bar{\mathbf{m}}_1 d\xi_1 + \bar{\mathbf{m}}_2 d\xi_2\right) \cdot \left(\bar{\mathbf{m}}_1 d\xi_1 + \bar{\mathbf{m}}_2 d\xi_2\right) \\ &= \left(\bar{\mathbf{m}}_1 \cdot \bar{\mathbf{m}}_1\right) d\xi_1^2 + \left(\bar{\mathbf{m}}_1 \cdot \bar{\mathbf{m}}_2\right) d\xi_1 d\xi_2 + \bar{\mathbf{m}}_2 \cdot \bar{\mathbf{m}}_2 d\xi_2^2 \\ &= E d\xi_1^2 + F d\xi_1 d\xi_2 + G d\xi_2^2 \end{aligned} \tag{7.10}$$

where E, F and G are the first fundamental coefficient of a undeformed midplane surface [50]. The first fundamental coefficients E, F and G are identical to the component of metric tensor $\bar{\mathbf{g}}_{11}, \bar{\mathbf{g}}_{12}$ and $\bar{\mathbf{g}}_{22}$, respectively.

The component of curvature tensor are calculated with aid of the inner product of the unit normal vector and the vector which result from second partial derivative of the undeformed and deformed midplane surface with respect to

parameter (ξ_1, ξ_2). Therefore, the component of curvature tensor are calculated and denoted by Eq. (7.11).

$$\bar{\kappa}_{\alpha\beta} = -\bar{\mathbf{m}}_3 \cdot \frac{\partial \bar{\mathbf{m}}_\alpha}{\partial \xi_\alpha}, \quad \kappa_{\alpha\beta} = -\mathbf{m}_3 \cdot \frac{\partial \mathbf{m}_\alpha}{\partial \xi_\alpha} \tag{7.11}$$

Similarly, in differential geometry, the inner product of the unit normal vector and the vector which result from the second partial derivative of the undeformed midplane surface are used to represent second fundamental form of a undeformed midplane surface [50] as follow:

$$\begin{aligned} II &= \bar{\mathbf{m}}_3 \cdot \frac{\partial^2 \bar{\mathbf{r}}}{\partial \xi_1^2} d\xi_1^2 + \bar{\mathbf{m}}_3 \cdot \frac{\partial^2 \bar{\mathbf{r}}}{\partial \xi_1 \partial \xi_2} d\xi_1 d\xi_2 + \bar{\mathbf{m}}_3 \cdot \frac{\partial^2 \bar{\mathbf{r}}}{\partial \xi_2^2} d\xi_2^2 \\ &= L d\xi_1^2 + M d\xi_1 d\xi_2 + N d\xi_2^2 \end{aligned} \tag{7.12}$$

where L, M and N are the second fundamental coefficient of a undeformed midplane surface. Except for sign, the first fundamental coefficients L, M and N are identical to the component of curvature tensor $\bar{\kappa}_{11}, \bar{\kappa}_{12}$ and $\bar{\kappa}_{22}$, respectively.

When we determine the metric properties of a surface, such as length of line element, area of element, Gaussian curvature, it is convenient to use the first or second fundamental form. For this reason, hereafter, the metric properties of a surface is discussed by using the two fundamental forms.

Finally, from the definition of Lagrange strain tensor and the deformation gradient, the Lagrange strain tensor can be approximated by [61]

$$\mathbf{E}=\frac{1}{2}\left(\mathbf{F}^{\mathrm{T}}\mathbf{F}-\mathbf{I}\right)\approx\frac{1}{2}\left(g_{\alpha\beta}-\bar{g}_{\alpha\beta}\right)\bar{\mathbf{m}}^{\alpha}\otimes\bar{\mathbf{m}}^{\beta}+\xi_3\left(\kappa_{\beta}^{\lambda}-\bar{\kappa}_{\beta}^{\lambda}\right)g_{\alpha\lambda}\bar{\mathbf{m}}^{\alpha}\otimes\bar{\mathbf{m}}^{\beta} \qquad (7.13)$$

Where $\frac{1}{2}\left(\mathrm{g}_{\alpha\beta}-\bar{\mathrm{g}}_{\alpha\beta}\right)\overline{\mathbf{m}}^{\alpha}\otimes\overline{\mathbf{m}}^{\beta}$ is defined by midplane Lagrange strain tensor $\boldsymbol{\gamma}=\gamma_{\alpha\beta}\overline{\mathbf{m}}^{\alpha}\otimes\overline{\mathbf{m}}^{\beta}$ and $\frac{1}{2}\left(\kappa_{\beta}^{\lambda}-\bar{\kappa}_{\beta}^{\lambda}\right)\mathrm{g}_{\alpha\lambda}\overline{\mathbf{m}}^{\alpha}\otimes\overline{\mathbf{m}}^{\beta}$ is defined by curvature change tensor $\Delta\boldsymbol{\kappa}=\kappa_{\alpha\beta}\overline{\mathbf{m}}^{\alpha}\otimes\overline{\mathbf{m}}^{\beta}$.

It is noted that component of midplane Lagrange strain tensor is defined by the difference of the component of metric tensor on the deformed and undeformed midplane surface. In other words, the component of midplane Lagrange strain tensor re-expressed by matrix form using first fundamental coefficient as follow:

$$\frac{1}{2}\left(g_{\alpha\beta}-\bar{g}_{\alpha\beta}\right)=\frac{1}{2}\left\{\begin{bmatrix}E & F\\ F & G\end{bmatrix}-\begin{bmatrix}\bar{E} & \bar{F}\\ \bar{F} & \bar{G}\end{bmatrix}\right\} \qquad (7.14)$$

Moreover, the component of curvature change tensor can be re-expressed into by matrix form using first and second fundamental coefficient as follow:

$$\left(\kappa_{\beta}^{\lambda}-\bar{\kappa}_{\beta}^{\lambda}\right)g_{\alpha\lambda}=\kappa_{\alpha\beta}-g_{\alpha\lambda}\bar{g}^{\lambda\mu}\bar{\kappa}_{\mu\beta}=-\left\{\begin{bmatrix}L & M\\ M & N\end{bmatrix}-\begin{bmatrix}E & F\\ F & G\end{bmatrix}\begin{bmatrix}\bar{E} & \bar{F}\\ \bar{F} & \bar{G}\end{bmatrix}^{-1}\begin{bmatrix}\bar{L} & \bar{M}\\ \bar{M} & \bar{N}\end{bmatrix}\right\} \qquad (7.15)$$

7.3 Strain fields of the saddle-shaped bistable structure

A saddle surface is a surface containing a saddle point at which Gaussian curvature have minus value. A saddle-shaped bistable structure is realized by perfect bonding of two surfaces of a saddle-shaped panel on stress-free state

initially, as illustrated in Figure 7.2. These two surfaces are defined by an upper $\overline{\Omega}^{up}$ undeformed surface and a lower undeformed surface $\overline{\Omega}^{low}$ separately; depend on the relative position of the two surfaces. The two undeformed saddle-shaped surfaces $\overline{\Omega}$ are represented by a parametric equation with two parameters (Let $\xi_1 \equiv u$, $\xi_2 \equiv v$ in this section). A parametric surface f(u,v) is defined by a set three functions x(u,v), y(u,v) and z(u,v), one for each Cartesian coordinate as follow:

$$f(u,v) = \left[x(u,v), y(u,v), z(u,v)\right] \tag{7.16}$$

By using this representation type of surface, the surface chart of the two undeformed saddle-shape surfaces is represented as follow:

$$\bar{\Omega}(u,v) = \begin{bmatrix} \bar{\Omega}^{up} \\ \bar{\Omega}^{low} \end{bmatrix} = \begin{bmatrix} u, v, \frac{1}{2}\bar{\kappa}_{11}^{o}u^2 - \frac{1}{2}\bar{\kappa}_{22}^{o}v^2 \\ u, v, -\frac{1}{2}\bar{\kappa}_{11}^{o}u^2 + \frac{1}{2}\bar{\kappa}_{22}^{o}v^2 \end{bmatrix} \tag{7.17}$$

where $\overline{\kappa}_{11}^{o}$ and $\overline{\kappa}_{22}^{o}$ are corresponding to the principal curvature value at $\overline{\Omega}(0,0)$.

Based on the surface chart, the first and second fundamental coefficients of two undeformed saddle-shaped surfaces are expressed as follow:

$$\begin{bmatrix} \bar{E} = \bar{\mathbf{m}}_1 \cdot \bar{\mathbf{m}}_1 = 1 + \left(\bar{\kappa}_{11}^o\right)^2 u^2 & L = \bar{\mathbf{m}}_3 \cdot \bar{\mathbf{m}}_{1,1} = -\bar{\kappa}_{11} = \dfrac{\pm\left(\bar{\kappa}_{11}^o\right)^2}{\sqrt{1 + \left(\bar{\kappa}_{11}^o\right)^2 u^2 + \left(\bar{\kappa}_{22}^o\right)^2 v^2}} \\ \bar{F} = \bar{\mathbf{m}}_1 \cdot \bar{\mathbf{m}}_2 = -\bar{\kappa}_{11}^o \bar{\kappa}_{22}^o uv & M = \bar{\mathbf{m}}_3 \cdot \bar{\mathbf{m}}_{1,2} = -\bar{\kappa}_{12} = 0 \\ \bar{G} = \bar{\mathbf{m}}_2 \cdot \bar{\mathbf{m}}_2 = 1 + \left(\bar{\kappa}_{22}^o\right)^2 v^2 & N = \bar{\mathbf{m}}_3 \cdot \bar{\mathbf{m}}_{2,2} = -\bar{\kappa}_{22} = \dfrac{\mp\left(\bar{\kappa}_{22}^o\right)^2}{\sqrt{1 + \left(\bar{\kappa}_{11}^o\right)^2 u^2 + \left(\bar{\kappa}_{22}^o\right)^2 v^2}} \end{bmatrix} \tag{7.18}$$

where the upper signs of the $\pm$ and $\mp$ symbol is corresponding to the second fundamental coefficients of the upper undeformed saddle-shaped surface.

From the definition of Gaussian curvature, the Gaussian curvature of two undeformed saddle-shaped surfaces is expressed [50] as follow:

$$K = \frac{\det(II)}{\det(I)} = \frac{LN - M^2}{EG - F^2} = \frac{-\left(\bar{\kappa}_{11}^o\right)\left(\bar{\kappa}_{22}^o\right)}{\left(1 + \left(\bar{\kappa}_{11}^o\right)^2 u^2 + \left(\bar{\kappa}_{22}^o\right)^2 v^2\right)^2} \tag{7.19}$$

Something to notice here is that the Gaussian curvatures of two undeformed saddle-shaped surfaces are identical to each other, regardless of the sign of principal curvature.

Conceptually, after perfect bonding of these two surfaces, the assembled surface will deform like one surface. With this in mind, the deformed surface is treated as one independent surface. The deformed surface is assumed as a polynomial parametric surface in which the three set functions x(u,v), y(u,v) and z(u,v) have a same order of polynomials function. In this dissertation, three kinds of order are considered (i.e. 2-nd order, 3-rd order and 4-th order). The

corresponding three surface charts of deformed surface are represented as follow:

$$\Omega=\begin{bmatrix} x(u,v) \\ y(u,v) \\ z(u,v) \end{bmatrix}=\begin{bmatrix} a_0+a_1u+a_2v+a_3u^2+a_4uv+a_5v^2 \\ b_0+b_1u+b_2v+b_3u^2+b_4uv+b_5v^2 \\ c_0+c_1u+c_2v+c_3u^2+c_4uv+c_5v^2 \end{bmatrix} \tag{7.20}$$

$$\Omega=\begin{bmatrix} x(u,v) \\ y(u,v) \\ z(u,v) \end{bmatrix}=\begin{bmatrix} a_0+a_1u+a_2v+a_3u^2+a_4uv+a_5v^2+a_6u^3+a_7u^2v+a_8uv^2+a_9v^3 \\ b_0+b_1u+b_2v+b_3u^2+b_4uv+b_5v^2+b_6u^3+b_7u^2v+b_8uv^2+b_9v^3 \\ c_0+c_1u+c_2v+c_3u^2+c_4uv+c_5v^2+c_6u^3+c_7u^2v+c_8uv^2+c_9v^3 \end{bmatrix} \tag{7.21}$$

$$\Omega=\begin{bmatrix} x(u,v) \\ y(u,v) \\ z(u,v) \end{bmatrix}=\begin{bmatrix} a_0+a_1u+a_2v+a_3u^2+a_4uv+a_5v^2+a_6u^3+a_7u^2v+a_8uv^2+a_9v^3\ldots \\ \quad +a_{10}u^4+a_{11}u^3v+a_{12}u^2v^2+a_{13}uv^3+a_{14}v^4 \\ b_0+b_1u+b_2v+b_3u^2+b_4uv+b_5v^2+b_6u^3+b_7u^2v+b_8uv^2+b_9v^3\ldots \\ \quad +b_{10}u^4+b_{11}u^3v+b_{12}u^2v^2+b_{13}uv^3+b_{14}v^4 \\ c_0+c_1u+c_2v+c_3u^2+c_4uv+c_5v^2+c_6u^3+c_7u^2v+c_8uv^2+c_9v^3\ldots \\ \quad +c_{10}u^4+c_{11}u^3v+c_{12}u^2v^2+c_{13}uv^3+c_{14}v^4 \end{bmatrix} \tag{7.22}$$

Although the assembled surface deform like one surface externally, the stress and strain field of upper and lower surface are certainly different from each other internally. With this in mind, the Lagrange strain of saddle-shaped bistable structure is divided into a part of upper and a part of lower surface according to the position of surface on the basis of ξ_3-axis (i.e., $\xi_3 = 0$) because the saddle-shaped bistable structure is realized by perfect bonding between face-to-face surfaces of two saddle-shaped surface on stress-free state as shown in Figure 7.2. The Lagrange strain are thus given by

$$\mathbf{E}^{(upper)}=\left[\frac{1}{2}\left(g_{\alpha\beta}-\bar{g}_{\alpha\beta}^{(upper)}\right)+\xi_3\left(\kappa_\beta^\lambda-\bar{\kappa}_\beta^{\lambda(upper)}\right)g_{\alpha\lambda}\right]\bar{\mathbf{m}}^{\alpha(upper)}\otimes\bar{\mathbf{m}}^{\beta(upper)},\quad 0\le\xi_3\le\frac{h}{2} \tag{7.23}$$

$$\mathbf{E}^{(lower)}=\left[\frac{1}{2}\left(g_{\alpha\beta}-\bar{g}_{\alpha\beta}^{(lower)}\right)+\xi_3\left(\kappa_\beta^\lambda-\bar{\kappa}_\beta^{\lambda(lower)}\right)g_{\alpha\lambda}\right]\bar{\mathbf{m}}^{\alpha(lower)}\otimes\bar{\mathbf{m}}^{\beta(lower)},\quad -\frac{h}{2}\le\xi_3\le 0 \tag{7.24}$$

where the basis vector, metric and curvature tensor marked “upper” means the quantity calculated by the upper saddle-shaped surface on stress free state. On the contrary, the basis vector, metric and curvature tensor marked “lower” means the quantity calculated by the lower saddle-shaped surface on stress-free state.

7.4 Analytical model

7.4.1 Strain energy density of saddle-shaped bistable shell structure

In this section, an analytical model is developed to predict the final shape of the saddle-shaped bistable structure. The solution (i.e., the final shape) is obtained by minimizing the total potential energy of the bistable structure. This minimization is achieved by equating the first variation of the total potential energy, $\delta\Pi$.

Using the aforementioned total strain field and assuming a plane stress state, the total potential energy is expressed as integration of energy density over the volume [61].

$$\Pi = \int_V \frac{1}{2}\left(\gamma_{\alpha\beta} + \theta^3 \Delta\kappa_{\alpha\beta}\right) D^{\alpha\beta\rho\mu} \left(\gamma_{\rho\mu} + \theta^3 \Delta\kappa_{\rho\mu}\right) dV \tag{7.25}$$

The volume integral can be re-expressed as the integral over the midplane and through thickness. Therefore, the total potential energy is re-expressed as integration of energy density over the midplane and through thickness [61].

$$\Pi = \sum_{i=1}^{n} \int_{-\frac{L}{2}}^{\frac{L}{2}} \int_{-\frac{L}{2}}^{\frac{L}{2}} \int_{h_i^{btm}}^{h_i^{top}} \frac{1}{2} \left(\gamma_{\alpha\beta} + \xi_3 \Delta\kappa_{\alpha\beta}\right) D^{\alpha\beta\rho\mu} \left(\gamma_{\rho\mu} + \xi_3 \Delta\kappa_{\rho\mu}\right) \left(1 + \xi_3 \kappa_\lambda^\lambda\right) \sqrt{\det\left(g_{\alpha\beta}\right)} d\xi_3 d\xi_2 d\xi_1 \quad (7.26)$$

where L is the side length of the bistable structure. Symbols h_i^{top}, h_i^{btm} refer to the position of the upper surface and the lower surface corresponding to i-th surface, respectively.

The plane stress constitutive equations $D^{\alpha\beta\rho\mu}$ for homogeneous linear elastic isotropic material are given in terms of the metric tensor of undeformed midplane surface as follow:

$$D^{\alpha\beta\rho\mu} = \frac{E}{2(1-\nu^2)} \left(\left(\bar{g}^{\alpha\rho} \bar{g}^{\beta\mu} + \bar{g}^{\alpha\mu} \bar{g}^{\beta\rho} \right) (1-\nu) + 2\nu \bar{g}^{\alpha\beta} \bar{g}^{\rho\mu} \right) \quad (7.27)$$

7.4.2 Minimization of total potential energy

The first variation of total potential energy, $\delta\Pi$ should be equal to zero to guarantee the existence of solution. The requirement for the existence of solution is as follow.

$$\delta\Pi = \sum_{i=1}^{n} \left\{ \left(\frac{\partial \Pi}{\partial a_i} \right) \delta a_i + \left(\frac{\partial \Pi}{\partial b_i} \right) \delta b_i + \left(\frac{\partial \Pi}{\partial c_i} \right) \delta c_i \right\} = 0 \quad (7.28)$$

Eq. (7.27) is the nonlinear algebraic equations which have n-unknowns. In order to solve these nonlinear algebraic equations, The Newton-Raphson iterative method was used. At first iteration, an initial solution was assumed as a undeformed saddle shape. At next iteration, a solution is updated and the updated solution is considered as a candidate solution subsequent. The second

variation of total potential energy (i.e., jacobian) was estimated to identify the stability of the system in each iteration. The jacobian is calculated by using complex derivative method [58].

7.5 The comparison between the analytical result and FE result

For the verification of the analytical model, FE analysis was performed. The FE model and analysis procedure are equivalent to the FE model in Chapter 5. As mentioned in section 6.4, the analysis are performed for three kinds of undeformed saddle shape of which the order are 2-nd, 3-rd and 4-th order subsequently. Material properties of plate used in analysis are summarized in Table 7.1.

Two stable shapes of the saddle-shaped bistable panel can be defined separately by Mode 1 and Mode 2 according to the sign of curvature as shown in Figure 7.3. Mode 1 is defined as a saddle shape with $\kappa_{11} > 0$ and $\kappa_{22} < 0$. On the contrary, Mode 2 is defined as a saddle shape with $\kappa_{11} < 0$ and $\kappa_{22} > 0$.

The results of the analytical model are shown in Table 7.2 and 7.3. As shown on the result, all kind of case study shows the bistability and the configuration of those are saddle shape seemingly.

Moreover, this final saddle shape closely identical to the initial undeformed saddle shape midplane surface as shown in Figure 7.4. Specifically, when

compared to the undeformed saddle quantitatively at each material coordinate (ξ_1, ξ_2), the maximum absolute error between the position of undeformed and deformed saddle shape is about 1.5mm as shown in Figure 7.5. Moreover, the Gaussian curvature of deformed shape is also almost same with that of undeformed saddle shape midplnae surface at $\overline{\Omega}(0,0)$. The maximum absolute error between the Gaussian curvautre of undeformed and deformed saddle shape is also negligible small (i.e. $0.15m^{-1}$) as shown in Figure 7.6.

This result means that the deformed midplane saddle shape can be easily determined and designed by the undeformed midplane saddle shape without complicated analysis.

7.6 Manufacturing of saddle shape bistable shell structure

The feasibility of saddle shape bistable structure was studied by numerical analysis. However, it is necessary to identify the feasibility of saddle shape bistable structure experimentally for rigorous validation. The saddle shape bistable shell structure is manufactured by casting technique. For casting, firstly, casting mold is needed to be designed. The casting mold is designed by using 3D CAD program for the saddle shape bistable structure with initial curvature $10m^{-1}$, side-length 150mm and thickness 1mm; as shown in Figure 7.7. The casting mold consists of two part in order to make assembling and de-assembling work

easily.

The designed CAD models are printed by 3D printer, Eden 350 of Stratasys Ltd., with resolution 28μm. The material of mold is RGD 535. Printing time is about 20hr. The printed molds are fastened by nuts and bolts, as shown in Figure 7.8. Final product, saddle shape shell structure, is manufactured by injecting the casting material into the printed molds; and by curing the injected casting material. The casting material is PMC-790 of Smooth-On Inc., which consist of Part A and Part B. The mix ratio of PMC is 2A : 1B by weight.

The casting material which is injected into casting mold is cured for 48hr at room temperature. After curing, two saddle shape shell structure is demolded from casting mold, as shown Figure 7.9.

The saddle shape bistable shell structure is induced by face-to-face perfect bonding of two saddle shape shell structure on stress-free state. Based on this idea, the saddle shape bistable structure is realized experimentally as following procedure.

1) Two saddle shape shell structure are aligned parallel to each other in principal direction of curvature but the curvature values are opposite each other.

2) The aligned two shell structure is pressing by two high-strength acrylic plate and the acrylic plates are clamped by four clampers and for nuts

and bolts set as shown in Figure 7.10 (a) and (b) . The two pressed shell structures are bonded by URE-BOND of Smooth-On Inc., which is a urethane adhesive compound.

3) After pressing and bonding, the boned shell structure is relaxed by removing the four clampers and four nuts and bolts.

4) As the four clampers and four nuts and bolts are removed, one stable saddle shape shell structure is generated as shown in Figure 7.11 (a). Following this step, the other stable saddle shape is induced by mechanical load (i.e. moment) as illustrated in Figure 7.11 (b).

When observing the final shape of manufactured saddle shape bistable shell structure with the naked eye, the surface of saddle shape bistable shell is almost identical to the surface of casting mold. This result coincides with the result obtained by the numerical analysis.

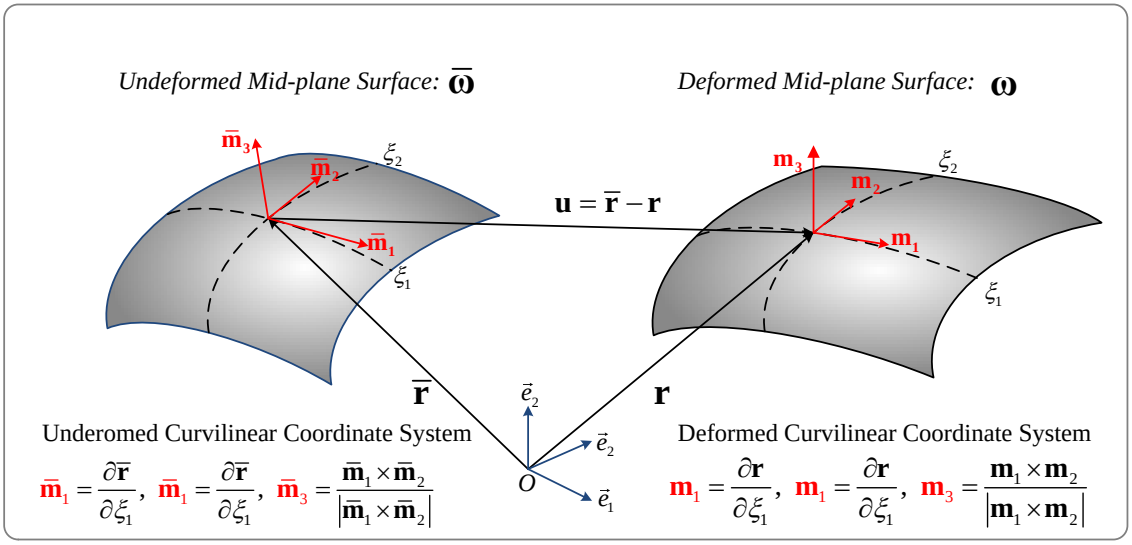

Figure 7.1 The mid-plane surface in undeformed and deformed configurations. Two vector $\bar{\mathbf{r}}$ and $\mathbf{r}$, indicate the position of the same material point in the Mid-plane surfaces.

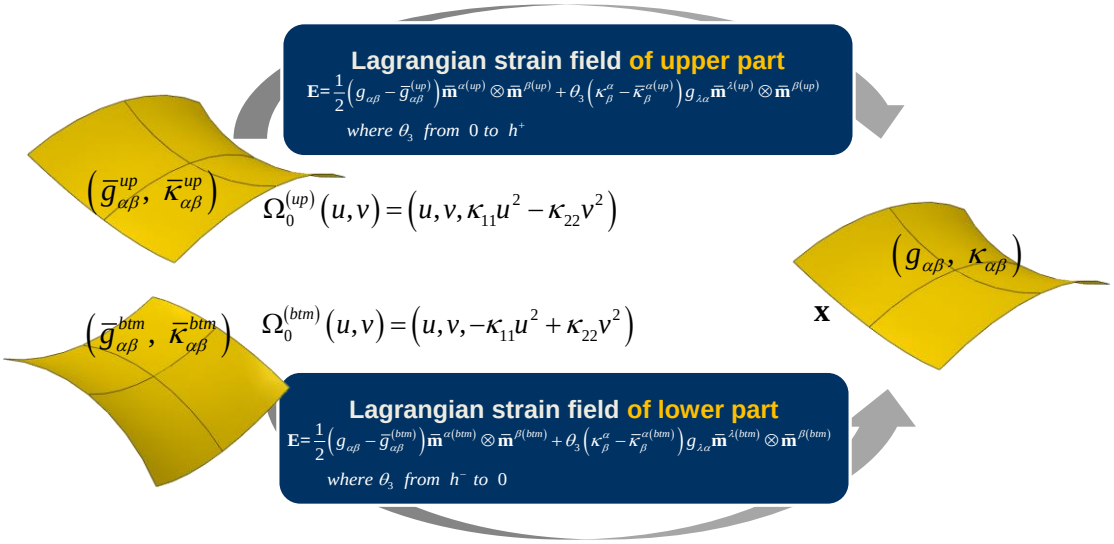

Figure 7.2 Lagrangian strain field of saddle shape bi-stable shell structure.

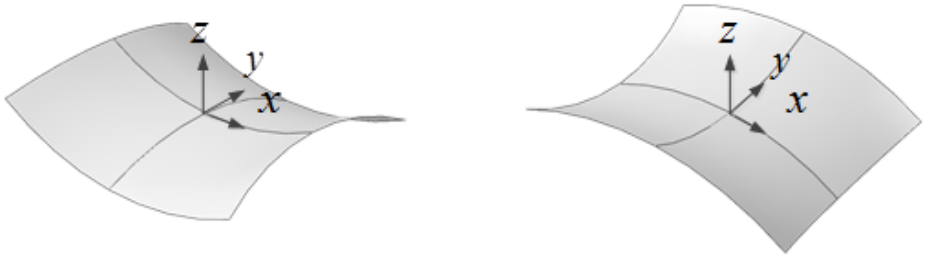

(a) (b)

Figure 7.3 Two possible configurations of the saddle shaped bi-stable panel: (a) Mode 1: $\kappa_{xx}>0,\ \kappa_{yy}<0$, (b) Mode 2: $\kappa_{xx}<0,\ \kappa_{yy}>0$

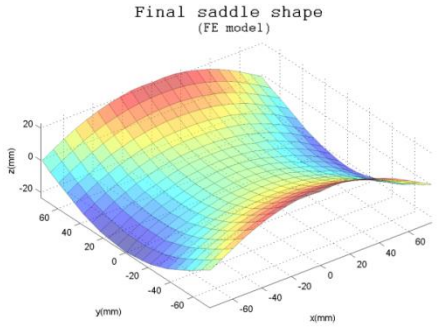

(a)

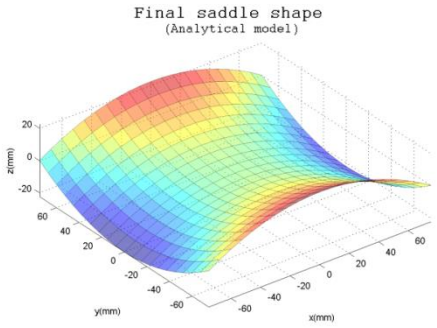

(b)

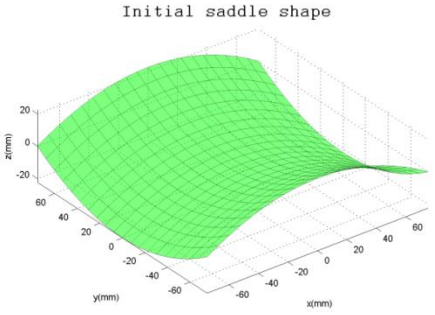

(c)

Figure 7.4 Comparison of saddle shape middle plane surface on: (a) Mode 1 deformed state (FE model), (b) Mode 1 deformed state (analytical model), and (c) Mode 1 initial undeformed state

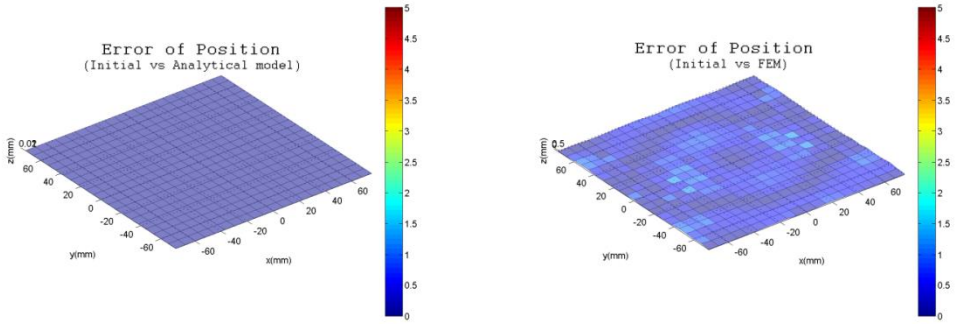

(a) (b)

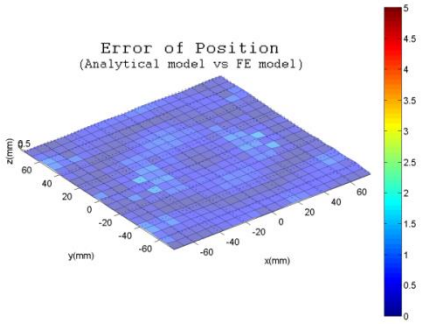

(c)

Figure 7.5 Maximum absolute error of position between: (a) undeformed state and deformed state (analytical model), (b) undeformed state and deformed state (FE model), and (c) deformed state (analytical model) and deformed state (FE model)

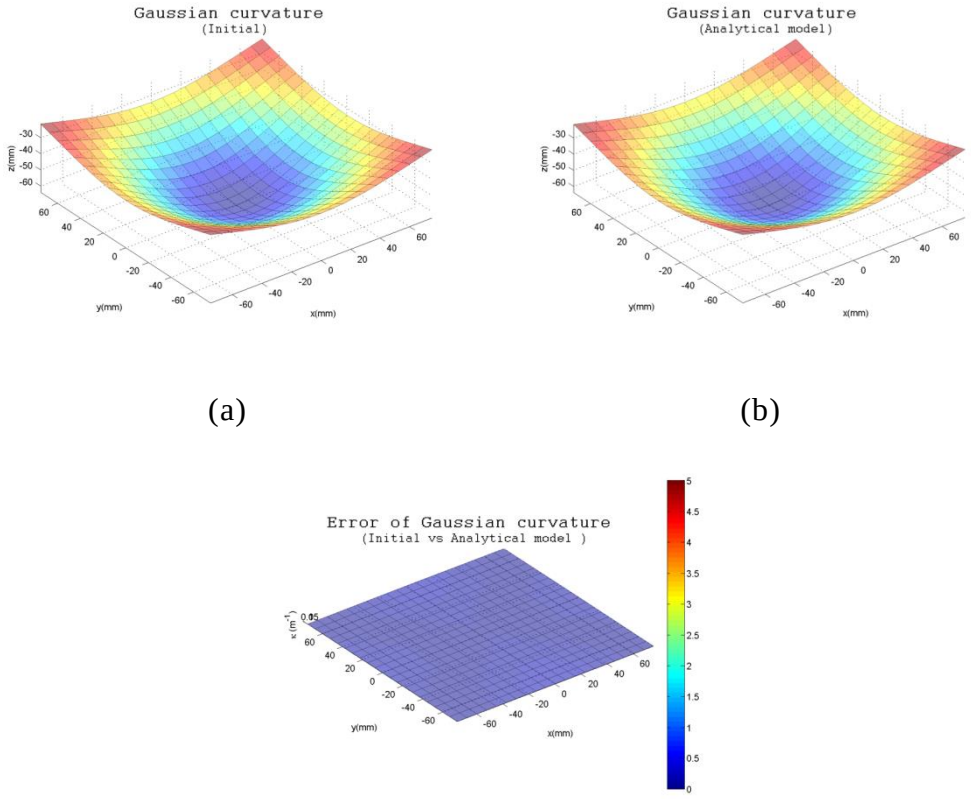

(a) (b)

(c)

Figure 7.6 Gaussian curvature field of**:** (a) undeformed midplane surface and (b) deformed midplane surface (analytical model); (c) Maximum absolute error of position between undeformed midplane surface and deformed midplane surface (analytical model)

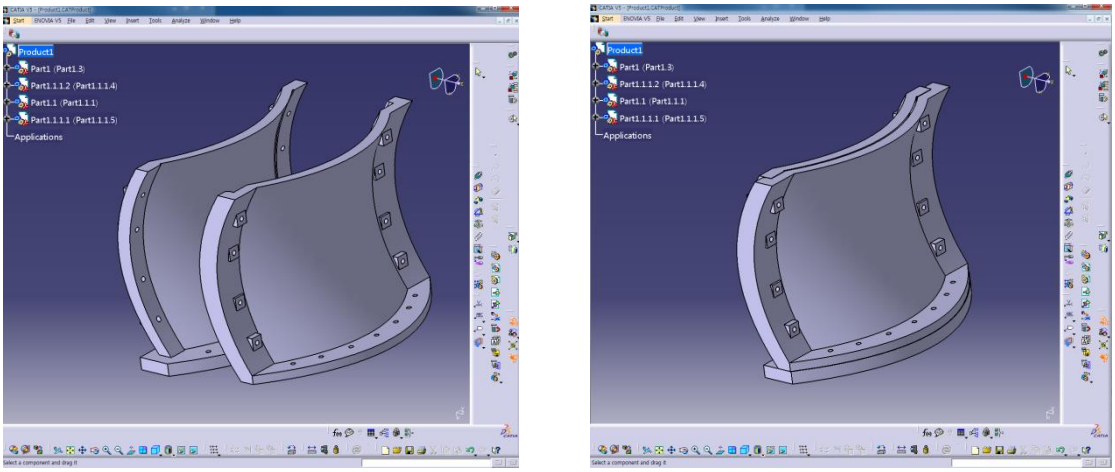

Figure 7.7 The casting mold designed by using 3D CAD program for the saddle shape bi-stable structure

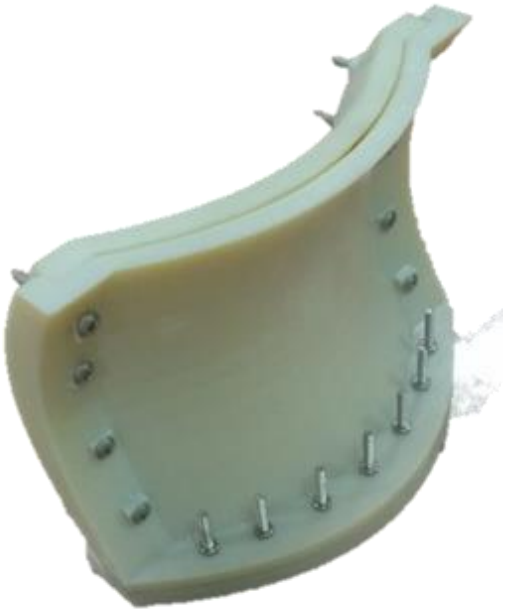

Figure 7.8 The printed molds fastened by nuts and bolts

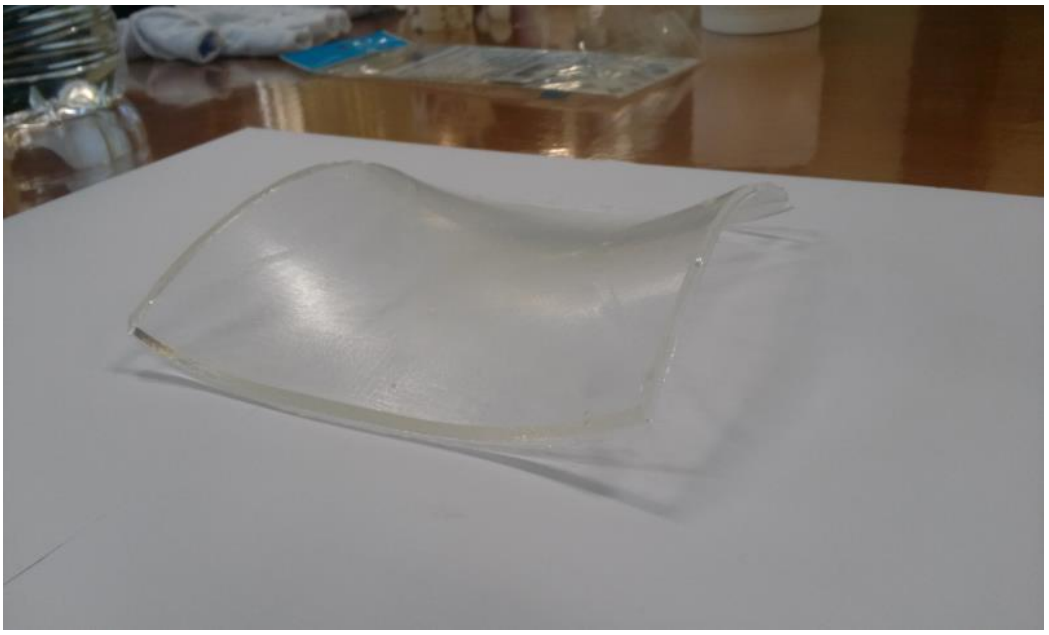

Figure 7.9 Cured saddle shape shell structure

(a)

(b)

Figure 7.10 Experimental pressing procedures: (a) aligned two saddle shape shell structure and (b) clamping for inducing residual stress

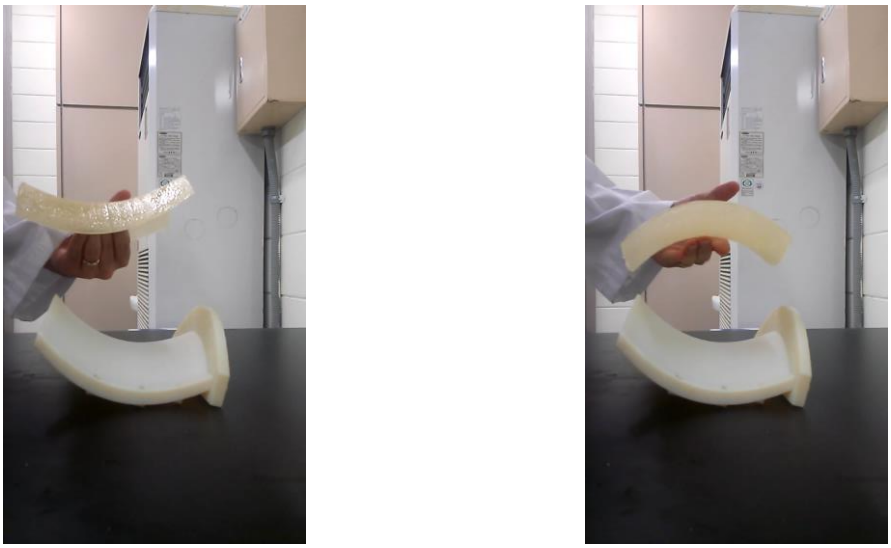

Figure 7.11 Sample of stable saddle shape shell structure: (a) Mode 1 and (b) Mode 2

Table 7.1 Material properties of shell

Property	Value
Elastic modulus (MPa)	1.8
Poisson's Ratio (v)	0.3
Thickness (mm)	1

Table 7.2 Mode 1 configuration obtained by the analytical model with respect to different polynomials order

2-nd order	x (u,v)	y (u,v)	z (u,v)
u	1.004556	0	0
v	0	0.995531	0
u^2	0	0	**4.992809**
uv	0	0	**0**
v^2	0	0	**-5.00494**
u^3			
u^2v			
uv^2			
v^3			
u^4			
u^3v			
u^2v^2			
uv^3			
v^4			

3-nd order	x (u,v)	y (u,v)	z (u,v)
u	1.005202	0	0
v	0	0.995485	0
u^2	0	0	**4.952172**
uv	0	0	**0.081099**
v^2	0	0	**-4.99129**
u^3	0.636468	-1.77342	0
u^2v	-5.24594	-0.70174	0
uv^2	-0.98056	5.431046	0
v^3	1.783134	0.084852	0
u^4			
u^3v			
u^2v^2			
uv^3			
v^4			

4-nd order	x (u,v)	y (u,v)	z (u,v)
u	1.005103	0	0
v	0	0.995202	0
u^2	0	0	**4.967065**
uv	0	0	**0**
v^2	1E-15	0	**-5.00092**
u^3	0.193423	0	0
u^2v	0	0.024452	0
uv^2	-0.32955	0	0
v^3	0	0.111527	0
u^4	0	0	-0.19364
u^3v	0	0	0
u^2v^2	0	0	0.63331
uv^3	0	0	0
v^4	0	0	0.57223

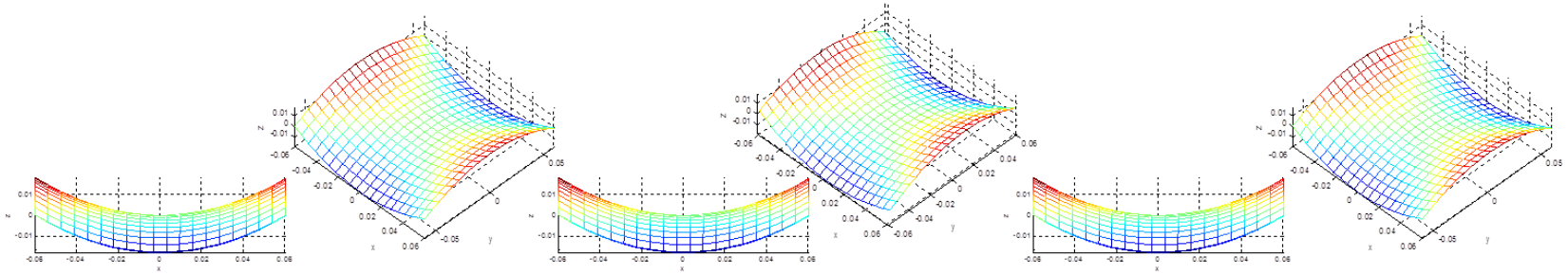

Table 7.3 Mode 2 configuration obtained by the analytical model with respect to different polynomials order

2-nd order	x (u,v)	y (u,v)	z (u,v)
u	1.004556	0	0
v	0	0.995531	0
u^2	0	0	**-4.99281**
uv	0	0	**0**
v^2	0	0	**5.004944**
u^3			
u^2v			
uv^2			
v^3			
u^4			
u^3v			
u^2v^2			
uv^3			
v^4			

3-nd order	x (u,v)	y (u,v)	z (u,v)
u	1.005202	0	0
v	0	0.995485	0
u^2	0	0	**-4.95217**
uv	0	0	**-0.0811**
v^2	0	0	**4.991288**
u^3	0.636468	-1.77342	0
u^2v	-5.24594	-0.70174	0
uv^2	-0.98056	5.431046	0
v^3	1.783134	0.084852	0
u^4			
u^3v			
u^2v^2			
uv^3			
v^4			

4-nd order	x (u,v)	y (u,v)	z (u,v)
u	1.005103	0	0
v	0	0.995202	0
u^2	0	0	**-4.96706**
uv	0	-2E-15	**0**
v^2	0	0	**5.000917**
u^3	0.193423	0	0
u^2v	0	0.024452	0
uv^2	-0.32955	0	0
v^3	0	0.111527	0
u^4	0	0	0.193641
u^3v	0	0	0
u^2v^2	0	0	-0.63331
uv^3	0	0	0
v^4	0	0	-0.57223

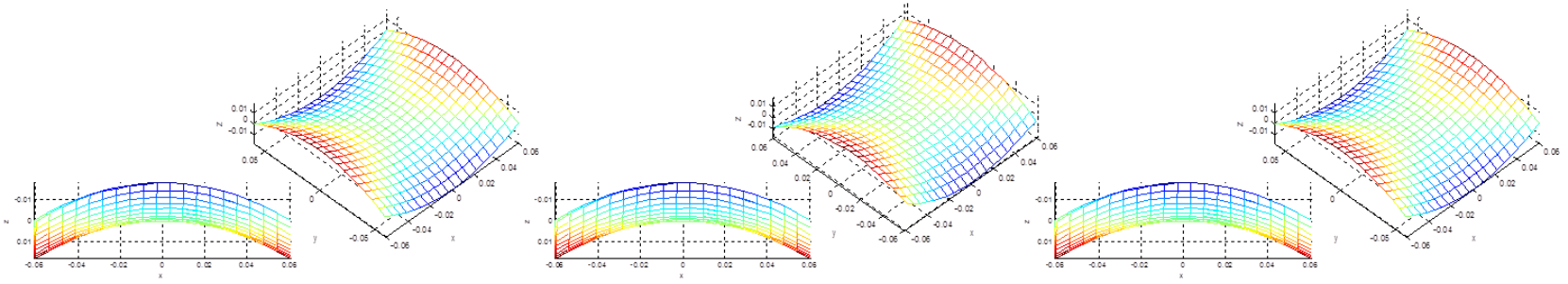

Chapter 8

Conclusion

In this dissertation, the numerical analysis model and design technique is bistable plate and shell with arbitrary shape has been developed as following.

First, in Chapter 2, to control the final curvatures of both stable states of a bistable CFRP laminate with a cylindrical tool-plate, the effect of misalignment between fiber direction and principal curvature directions of the tool-plate has been studied. Through experiment and an analytical model, it is verified that the final curvature of a bistable CFRP cross-ply laminate is the sum of the normal curvature of the tool-plate and final curvature of the laminates without initial curvature. It is expected that the results of this study will provide convenient guideline for designers seeking to tailor smart structures with bistable CFRP laminate.

In Chapter 3, the snap-through of square cross-ply bistable composites has been simulated and experimentally validated in order to evaluate the effect of the initial tool-plate curvature on the snap-through load. This effect has been estimated by the present simple analytical model. Furthermore, for the validation

of the pre-identified initial tool-plate curvature effect, experiments and FE analysis had been performed under a practical loading condition (i.e., vertical load). The following conclusion has been drawn from these analyses.

1. The snap-forth load increases linearly with increasing initial tool-plate curvature.
2. In contrast, the snap-back load decreases linearly with increasing initial tool-plate curvature.

Given this linear relation, the snap-through load of square cross-ply bistable composites with an arbitrary initial curvature can be easily predicted by just two snap-through experiments: with and without the initial curvature. Additionally, the approach of adding an initial curvature is expected to reduce the design complexity of square cross-ply bistable composites because the snap-through load is controllable without any changes in the existing design variables (e.g., thickness and lay-up sequence). For all these reasons, it is expected that the designers of bistable composites will be able to easily predict and design the snap-through load by making use of the initial tool-plate curvature effect through a simple analysis.

In Chapter 4, full FE model of bistable shell structure with SMA (Shape Memory Alloy) spring has been developed. Firstly, in order to simulate the behavior of SMA, Lagoudas model, most well-known SMA model, was utilized by writing ABAQUS user subroutine (UMAT) with FORTRAN. Secondly, FE model of SMA spring was integrated over bistable composite and then the snap-

through of bistable composite was induced by using shape memory effect of SMA spring. From this simulation, it is verified that SMA spring is a proper actuator for inducing the snap-through of bistable plate and shell structure. It is expected that this full FE model will be used as optimization tool in the position selection of actuator on the bistable shell structure.

In Chapter 5, a novel saddle-shaped bistable shell structure was proposed which cannot be expected to be manufactured from conventional shapes of composite laminated bistable structure. By defining the total strain field of the saddle-shaped bistable panel in material coordinate system, the mechanical model was discussed to explain the fundamental principle on the saddle-shaped bistable shell structure. Proposed analytical model can identify the bistability and predict the final curvature of the saddle-shaped bistable panel with respect to the change of a side-length. The results of analytical model are in accordance with those obtained by numerical prediction through finite element method. It is expected that this new saddle-shaped bistable panel and morphing concept through SMA spring will be a new potential smart structures based on the non-conventional shape of bistable structure because it utilizes the bistable structures not only for cylinder shape, but also more widely for general shapes.

In Chapter 6, analysis model of saddle shape bistable structure based on the assumed strain field have been developed by combining the compatibility condition without tiresome works, i.e. integration of assumed mid-plane strain

field and re-differentiation of the integrated stain field to substitute mid-plane shear strain-displacement relation. As a result, the analysis of bistable structure has been performed more efficiently. Moreover, from the analysis with increasing the polynomial approximation order of strain field and deflection field, the developed model has been verified. As a result, it is expected that the analysis of bistable structure, even bistable structure with complex shape, will be performed efficiently and accurately.

In Chapter 7, the analysis model of saddle shape bistable structure has been developed based on the shell theory, in order to represent the large deformed curvature. The accuracy of developed analysis model is validated by comparing the Final (deformed) shape obtained by the analysis model with the result obtained by FE analysis. In addition, the Gaussian curvature field obtained by the analysis model was compared with the initial Gaussian curvature field. From this result, it is identified that the Gaussian curvature field hardly change in order to minimize the deformation energy of structure. The tendency of the variation of Gaussian curvature field follows with the Gauss's Theorema Egregium.

The morphological design technique and model of bistable plate and shell structure, which are developed and verified in the dissertation, overcome the morphological limitation of the existing bistable structure and improve the design degree freedom of it. If the improved design degree freedom and the

bistability is applied into the classic mechanical system which have been focus on the mechanical property (i.e. strength or mass), the new mechanical system accompanied by the concept of morphing can be designed and expected as the high value-added system breaking stereotype.

Appendix

APPENDIX A: Detail expression of strain energy.

$$\begin{aligned} u_{\text{normal}} &= C_{xxxx}\left(E_{xx}-\alpha_{xx}\Delta T\right)\left(E_{xx}-\alpha_{xx}\Delta T\right) \\ &\quad +2C_{xxyy}\left(E_{xx}-\alpha_{xx}\Delta T\right)\left(E_{yy}-\alpha_{yy}\Delta T\right) \\ &\quad +C_{yyyy}\left(E_{yy}-\alpha_{yy}\Delta T\right)\left(E_{yy}-\alpha_{yy}\Delta T\right) \\ U_{\text{normal}} &= \frac{1}{2}\int_V u_{\text{normal}}\,dV \end{aligned} \tag{A-1}$$

$$\begin{aligned} u_{\text{shear}} &= 4C_{xyxy}\left(E_{xy}-\alpha_{xy}\Delta T\right)\left(E_{xy}-\alpha_{xy}\Delta T\right) \\ U_{\text{shear}} &= \frac{1}{2}\int_V u_{\text{shear}}\,dV \end{aligned} \tag{A-2}$$

$$\begin{aligned} u_{\text{coupling}} &= 2C_{xxxy}\left(E_{xx}-\alpha_{xx}\Delta T\right)\left(E_{xy}-\alpha_{xy}\Delta T\right) \\ &\quad +2C_{yyxy}\left(E_{yy}-\alpha_{yy}\Delta T\right)\left(E_{xy}-\alpha_{xy}\Delta T\right) \\ U_{\text{coupling}} &= \frac{1}{2}\int_V u_{\text{coupling}}\,dV \end{aligned} \tag{A-3}$$

Where, E_{ij} is Green-Lagrangian strain tensor component, α_{ij} is thermal expansion coefficient component, ΔT is the temperature change during curing process, and u_{normal}, u_{shear}, $u_{coupling}$ are strain energy density functions.

APPENDIX B: Detail expression of stiffness expression and force/moment resultant.

$$\begin{bmatrix} T_{11} & T_{12} & T_{13} \\ T_{21} & T_{22} & T_{23} \\ T_{31} & T_{32} & T_{33} \end{bmatrix} = \begin{bmatrix} \cos^2\theta & \sin^2\theta & -2\cos\theta\sin\theta \\ \sin^2\theta & \cos^2\theta & 2\cos\theta\sin\theta \\ \cos\theta\sin\theta & -\cos\theta\sin\theta & \cos^2\theta-\sin^2\theta \end{bmatrix} \tag{B-1}$$

where, θ is angle between fiber direction and x-axis.

$$\begin{bmatrix} Q_{11}^{(i)} & Q_{12}^{(i)} & 0 \\ Q_{12}^{(i)} & Q_{22}^{(i)} & 0 \\ 0 & 0 & Q_{66}^{(i)} \end{bmatrix} = \begin{bmatrix} T_{11} & T_{12} & T_{13} \\ T_{21} & T_{22} & T_{23} \\ T_{31} & T_{32} & T_{33} \end{bmatrix} \begin{bmatrix} \frac{E_1}{1-\nu_{12}\nu_{21}} & \frac{\nu_{12}E_2}{1-\nu_{12}\nu_{21}} & 0 \\ \frac{\nu_{12}E_2}{1-\nu_{12}\nu_{21}} & \frac{E_2}{1-\nu_{12}\nu_{21}} & 0 \\ 0 & 0 & G_{12} \end{bmatrix} \begin{bmatrix} T_{11} & T_{21} & T_{31} \\ T_{12} & T_{22} & T_{32} \\ T_{13} & T_{23} & T_{33} \end{bmatrix} \tag{B-2}$$

$$\begin{bmatrix} A_{11} & A_{12} & A_{13} \\ A_{21} & A_{22} & A_{23} \\ A_{31} & A_{32} & A_{33} \end{bmatrix} = \sum_{i=1}^{n} \begin{bmatrix} Q_{11}^{(i)} & Q_{12}^{(i)} & 0 \\ Q_{12}^{(i)} & Q_{22}^{(i)} & 0 \\ 0 & 0 & Q_{66}^{(i)} \end{bmatrix} z\Big|_{z_i^{btm}}^{z_i^{top}} \tag{B-3}$$

$$\begin{bmatrix} B_{11} & B_{12} & B_{13} \\ B_{21} & B_{22} & B_{23} \\ B_{31} & B_{32} & B_{33} \end{bmatrix} = \frac{1}{2}\sum_{i=1}^{n} \begin{bmatrix} Q_{11}^{(i)} & Q_{12}^{(i)} & 0 \\ Q_{12}^{(i)} & Q_{22}^{(i)} & 0 \\ 0 & 0 & Q_{66}^{(i)} \end{bmatrix} z^2\Big|_{z_i^{btm}}^{z_i^{top}} \tag{B-4}$$

$$\begin{bmatrix} D_{11} & D_{12} & D_{13} \\ D_{21} & D_{22} & D_{23} \\ D_{31} & D_{32} & D_{33} \end{bmatrix} = \frac{1}{3}\sum_{i=1}^{n} \begin{bmatrix} Q_{11}^{(i)} & Q_{12}^{(i)} & 0 \\ Q_{12}^{(i)} & Q_{22}^{(i)} & 0 \\ 0 & 0 & Q_{66}^{(i)} \end{bmatrix} z^3\Big|_{z_i^{btm}}^{z_i^{top}} \tag{B-5}$$

$$\begin{bmatrix} N_1 \\ N_2 \\ N_6 \end{bmatrix} = \sum_{i=1}^{n} \begin{bmatrix} Q_{11}^{(i)} & Q_{12}^{(i)} & 0 \\ Q_{12}^{(i)} & Q_{22}^{(i)} & 0 \\ 0 & 0 & Q_{66}^{(i)} \end{bmatrix} \begin{bmatrix} \alpha_{xx}^{(i)} \\ \alpha_{yy}^{(i)} \\ 2\alpha_{xy}^{(i)} \end{bmatrix} z \Big|_{z_i^{btm}}^{z_i^{top}} \tag{B-6}$$

$$\begin{bmatrix} M_1 \\ M_2 \\ M_6 \end{bmatrix} = \frac{1}{2} \sum_{i=1}^{n} \begin{bmatrix} Q_{11}^{(i)} & Q_{12}^{(i)} & 0 \\ Q_{12}^{(i)} & Q_{22}^{(i)} & 0 \\ 0 & 0 & Q_{66}^{(i)} \end{bmatrix} \begin{bmatrix} \alpha_{xx}^{(i)} \\ \alpha_{yy}^{(i)} \\ 2\alpha_{xy}^{(i)} \end{bmatrix} z^2 \Big|_{z_i^{btm}}^{z_i^{top}} \tag{B-7}$$

APPENDIX C: Detail derivation of reduced compatibility equation.

$$\text{Independant variable: } \varepsilon_{xx}^{u} = \frac{\partial u}{\partial x},\ \varepsilon_{yy}^{v} = \frac{\partial v}{\partial y},\ \gamma_{xy}^{u,v} = \frac{\partial u}{\partial y} + \frac{\partial v}{\partial x},\ w \tag{C-1}$$

$$\begin{aligned} &\frac{\partial^2}{\partial y^2}\left(\frac{\partial u}{\partial x} + \frac{1}{2}\left(\frac{\partial w}{\partial x}\right)^2\right) + \frac{\partial^2}{\partial x^2}\left(\frac{\partial v}{\partial y} + \frac{1}{2}\left(\frac{\partial w}{\partial y}\right)^2\right) - \frac{\partial^2}{\partial x \partial y}\left(\frac{\partial u}{\partial y} + \frac{\partial v}{\partial x} + \frac{\partial w}{\partial x}\frac{\partial w}{\partial y}\right) \\ &= \left(\frac{\partial^2 w}{\partial x \partial y}\right)^2 - \frac{\partial^2 w}{\partial x^2}\frac{\partial^2 w}{\partial y^2} \end{aligned} \tag{C-2}$$

By substituting the independent variables of Eq. (C-1) into the compatibility equation as denoted in (C-2), Compatibility equation re-expressed as follow:

$$\begin{aligned} &\frac{\partial^2}{\partial y^2}\left(\varepsilon_{xx}^{u} + \frac{1}{2}\left(\frac{\partial w}{\partial x}\right)^2\right) + \frac{\partial^2}{\partial x^2}\left(\varepsilon_{yy}^{v} + \frac{1}{2}\left(\frac{\partial w}{\partial y}\right)^2\right) - \frac{\partial^2}{\partial x \partial y}\left(\gamma_{xy}^{u,v} + \frac{\partial w}{\partial x}\frac{\partial w}{\partial y}\right) \\ &= \left(\frac{\partial^2 w}{\partial x \partial y}\right)^2 + \left(\frac{\partial^2 w}{\partial x^2}\frac{\partial^2 w}{\partial y^2}\right) \end{aligned} \tag{C-3}$$

where differential term related with displacement, w, are canceled out each other as follow:

$$\begin{aligned} &\Big(\frac{\partial^2 \varepsilon_{xx}^{u}}{\partial y^2} + \underbrace{\frac{\partial^3 w}{\partial x \partial y^2}\frac{\partial w}{\partial x}}_{a} + \underbrace{\left(\frac{\partial^2 w}{\partial x \partial y}\right)^2}_{b} + \frac{\partial^2 \varepsilon_{yy}^{v}}{\partial x^2} + \underbrace{\frac{\partial^3 w}{\partial x^2 \partial y}\frac{\partial w}{\partial y}}_{c} + \underbrace{\left(\frac{\partial^2 w}{\partial x \partial y}\right)^2}_{d} \\ &\quad - \frac{\partial^2 \gamma_{xy}^{u,v}}{\partial x \partial y} - \underbrace{\frac{\partial^3 w}{\partial x^2 \partial y}\frac{\partial w}{\partial y}}_{c} - \underbrace{\left(\frac{\partial^2 w}{\partial x \partial y}\right)^2}_{d} - \underbrace{\left(\frac{\partial^2 w}{\partial x^2}\frac{\partial^2 w}{\partial y^2}\right)}_{e} - \underbrace{\frac{\partial w}{\partial x}\frac{\partial^3 w}{\partial x \partial y^2}}_{a}\Big) = \underbrace{\left(\frac{\partial^2 w}{\partial x \partial y}\right)^2}_{b} - \underbrace{\left(\frac{\partial^2 w}{\partial x^2}\frac{\partial^2 w}{\partial y^2}\right)}_{e} \end{aligned} \tag{C-4}$$

Accordingly, compatibility equation is finally reduced as follow:

$$\frac{\partial^2 \varepsilon_{xx}^{u}}{\partial y^2} + \frac{\partial^2 \varepsilon_{yy}^{v}}{\partial x^2} - \frac{\partial^2 \gamma_{xy}^{u,v}}{\partial x \partial y} = 0 \tag{C-5}$$

Bibliography

[1] Thompson JMT, Hunt GW. A general theory of elastic stability: John Wiley & Sons; 1973.

[2] Timoshenko SP, Gere JM. Theory of elastic stability. 1961. McGrawHill-Kogakusha Ltd, Tokyo. 1961.

[3] Li B, Cao Y-P, Feng X-Q, Gao H. Mechanics of morphological instabilities and surface wrinkling in soft materials: a review. Soft Matter. 2012;8(21):5728-5745.

[4] Suresh S. Perspectives for the Inaugural Issue. Extreme Mechanics Letters. 2014;1:2.

[5] Kim S-W, Koh J-S, Lee J-G, Ryu J, Cho M, Cho K-J. Flytrap-inspired robot using structurally integrated actuation based on bistability and a developable surface. Bioinspiration & biomimetics. 2014;9(3):036004.

[6] Winterflood J, Blair D, Slagmolen B. High performance vibration isolation using springs in Euler column buckling mode. Physics Letters A. 2002;300(2):122-130.

[7] Avramov K, Mikhlin YV. Snap-through truss as a vibration absorber. Journal of Vibration and Control. 2004;10(2):291-308.

[8] Lynch JP, Loh KJ. A summary review of wireless sensors and sensor networks for structural health monitoring. Shock and Vibration Digest.

2006;38(2):91-130.

[9] Batra R, Porfiri M, Spinello D. Review of modeling electrostatically actuated microelectromechanical systems. Smart Materials and Structures. 2007;16(6):R23.

[10] Begley MR, Barker NS. Analysis and design of kinked (bent) beam sensors. Journal of Micromechanics and Microengineering. 2007;17(2):350.

[11] Yuen SC, Nurick G. The energy-absorbing characteristics of tubular structures with geometric and material modifications: an overview. Applied Mechanics Reviews. 2008;61(2):020802.

[12] Arrieta A, Hagedorn P, Erturk A, Inman D. A piezoelectric bistable plate for nonlinear broadband energy harvesting. Applied Physics Letters. 2010;97(10):104102.

[13] Winkelmann C, Kim SS, La Saponara V. Design and development of hybrid composite bistable structures for energy absorption under quasi-static tensile loading. Composite Structures. 2010;93(1):171-178.

[14] Harb A. Energy harvesting: State-of-the-art. Renewable Energy. 2011;36(10):2641-2654.

[15] Kim HS, Kim J-H, Kim J. A review of piezoelectric energy harvesting based on vibration. International Journal of precision engineering and manufacturing. 2011;12(6):1129-1141.

[16] Betts DN, Kim HA, Bowen CR, Inman D. Optimal configurations of bistable piezo-composites for energy harvesting. Applied Physics Letters.

2012;100(11):114104.

[17] Pellegrini SP, Tolou N, Schenk M, Herder JL. Bistable vibration energy harvesters: A review. Journal of Intelligent Material Systems and Structures. 2012:1045389X12444940.

[18] Dong L, Lakes R. Advanced damper with high stiffness and high hysteresis damping based on negative structural stiffness. International Journal of Solids and Structures. 2013;50(14):2416-2423.

[19] Harne R, Wang K. A review of the recent research on vibration energy harvesting via bistable systems. Smart Materials and Structures. 2013;22(2):023001.

[20] Kalathur H, Lakes R. Column dampers with negative stiffness: high damping at small amplitude. Smart Materials and Structures. 2013;22(8):084013.

[21] Shen L, Cha Y, Shams A, Porfiri M. Fabrication and buckling analysis of ionic polymer metal composite pipes. Smart Materials and Structures. 2013;22(10):105032.

[22] Zhang W-M, Yan H, Peng Z-K, Meng G. Electrostatic pull-in instability in MEMS/NEMS: A review. Sensors and Actuators A: Physical. 2014;214:187-218.

[23] Mattioni F, Weaver P, Friswell M, Potter K. Modelling and applications of thermally induced multistable composites with piecewise variation of lay-up in the planform. Collection of Technical Papers-AIAA/ASME/ASCE/AHS/ASC Structures, Structural Dynamics and Materials Conference, American Institute of Aeronautics and Astronautics Inc, Reston, VA, 2007. p. 20191-24344.

[24] Schultz MR. A concept for airfoil-like active bistable twisting structures. Journal of Intelligent Material Systems and Structures. 2007.

[25] Daynes S, Weaver P, Potter K. Aeroelastic study of bistable composite airfoils. Journal of Aircraft. 2009;46(6):2169-2174.

[26] Pirrera A, Avitabile D, Weaver P. Bistable plates for morphing structures: a refined analytical approach with high-order polynomials. International Journal of Solids and Structures. 2010;47(25):3412-3425.

[27] Arrieta AF, Bilgen O, Friswell M, Hagedorn P. Passive load alleviation bi-stable morphing concept. AIP Advances. 2012;2(3):032118.

[28] Arrieta AF, Bilgen O, Friswell MI, Ermanni P. Modelling and configuration control of wing-shaped bi-stable piezoelectric composites under aerodynamic loads. Aerospace Science and Technology. 2013;29(1):453-461.

[29] Arrieta AF, Kuder IK, Rist M, Waeber T, Ermanni P. Passive load alleviation aerofoil concept with variable stiffness multi-stable composites. Composite Structures. 2014;116:235-242.

[30] Hyer MW. Some observations on the cured shape of thin unsymmetric laminates. Journal of Composite Materials. 1981;15(2):175-194.

[31] Hyer MW. The room-temperature shapes of four-layer unsymmetric cross-ply laminates. Journal of Composite Materials. 1982;16(4):318-340.

[32] Jun W, Hong C. Effect of residual shear strain on the cured shape of unsymmetric cross-ply thin laminates. Composites science and technology. 1990;38(1):55-67.

[33] Jun W, Hong C. Cured shape of unsymmetric laminates with arbitrary lay-up angles. Journal of reinforced plastics and composites. 1992;11(12):1352-1366.

[34] Ren L, Parvizi-Majidi A, Li Z. Cured shape of cross-ply composite thin shells. Journal of Composite Materials. 2003;37(20):1801-1820.

[35] Cho M, Kim M-H, Choi HS, Chung CH, Ahn K-J, Eom YS. A study on the room-temperature curvature shapes of unsymmetric laminates including slippage effects. Journal of composite materials. 1998;32(5):460-482.

[36] Cho M, Roh HY. Non-linear analysis of the curved shapes of unsymmetric laminates accounting for slippage effects. Composites science and technology. 2003;63(15):2265-2275.

[37] Lee J-G, Ryu J, Lee H, Cho M. Saddle-shaped, bistable morphing panel with shape memory alloy spring actuator. Smart Materials and Structures. 2014;23(7):074013.

[38] Dano M-L, Hyer M. Snap-through of unsymmetric fiber-reinforced composite laminates. International Journal of Solids and Structures. 2002;39(1):175-198.

[39] Dano M-L, Hyer M. SMA-induced snap-through of unsymmetric fiber-reinforced composite laminates. International Journal of Solids and Structures. 2003;40(22):5949-5972.

[40] Diaconu CG, Weaver PM, Arrieta AF. Dynamic analysis of bi-stable composite plates. Journal of Sound and Vibration. 2009;322(4):987-1004.

[41] Ryu J, Kong J-P, Kim S-W, Koh J-S, Cho K-J, Cho M. Curvature tailoring

of unsymmetric laminates with an initial curvature. Journal of Composite Materials. 2012:0021998312462915.

[42] Seffen KA, Guest SD. Prestressed morphing bistable and neutrally stable shells. Journal of Applied Mechanics. 2011;78(1):011002.

[43] Kebadze E, Guest S, Pellegrino S. Bistable prestressed shell structures. International Journal of Solids and Structures. 2004;41(11):2801-2820.

[44] Kim S-W, Koh J-S, Cho M, Cho K-J. Design & analysis a flytrap robot using bi-stable composite. Robotics and Automation (ICRA), 2011 IEEE International Conference on: IEEE; 2011. p. 215-220.

[45] Panesar AS, Weaver PM. Optimisation of blended bistable laminates for a morphing flap. Composite Structures. 2012;94(10):3092-3105.

[46] Sousa C, Camanho P, Suleman A. Analysis of multistable variable stiffness composite plates. Composite Structures. 2013;98:34-46.

[47] Arrieta AF, Kuder IK, Waeber T, Ermanni P. Variable stiffness characteristics of embeddable multi-stable composites. Composites Science and Technology. 2014;97:12-18.

[48] Daynes S, Potter K, Weaver P. Bistable prestressed buckled laminates. Composites Science and Technology. 2008;68(15):3431-3437.

[49] Daynes S, Diaconu C, Potter K, Weaver P. Bistable prestressed symmetric laminates. Journal of composite materials. 2010;44(9):1119-1137.

[50] Struik DJ. Lectures on classical differential geometry: Courier Corporation; 2012.

[51] ABAQUS V. 6.12. Abaqus/CAE User's Manual, SIMULIA Corp. 2012.

[52] Potter K, Weaver P, Seman AA, Shah S. Phenomena in the bifurcation of unsymmetric composite plates. Composites Part A: Applied Science and Manufacturing. 2007;38(1):100-106.

[53] Lagoudas DC, Bo Z, Qidwai MA. A unified thermodynamic constitutive model for SMA and finite element analysis of active metal matrix composites. Mechanics of Composite Materials and Structures. 1996;3(2):153-179.

[54] An S-M, Ryu J, Cho M, Cho K-J. Engineering design framework for a shape memory alloy coil spring actuator using a static two-state model. Smart Materials and Structures. 2012;21(5):055009.

[55] L'vov V, Cesari E, Recarte V, Pérez-Landazábal J. Entropy change of martensitic transformation in ferromagnetic shape memory alloys. Acta Materialia. 2013;61(5):1764-1772.

[56] Salzbrenner R, Cohen M. On the thermodynamics of thermoelastic martensitic transformations. Acta Metallurgica. 1979;27(5):739-748.

[57] Ventsel E, Krauthammer T. Thin plates and shells: theory: analysis, and applications: CRC press; 2001.

[58] Kim S, Ryu J, Cho M. Numerically generated tangent stiffness matrices using the complex variable derivative method for nonlinear structural analysis. Computer Methods in Applied Mechanics and Engineering. 2011;200(1):403-413.

[59] Pietraszkiewicz W, Szwabowicz M, Vallée C. Determination of the midsurface of a deformed shell from prescribed surface strains and bendings via

the polar decomposition. International Journal of Non-Linear Mechanics. 2008;43(7):579-587.

[60] Pietraszkiewicz W, Szwabowicz M. Determination of the midsurface of a deformed shell from prescribed fields of surface strains and bendings. International journal of solids and structures. 2007;44(18):6163-6172.

[61] Bower AF. Applied mechanics of solids: CRC press; 2009.

국문 요약

본 논문에서는 최근 모핑 구조물로써 주목받고 있는 쌍안정 판 및 쉘 구조물의 임의의 형상 설계를 위한 해석 및 설계 기법을 개발하였다. 기존의 쌍안정 판 및 쉘 구조물의 경우 두 개의 쌍안정 형상이 원통형 형상에 국한되어 있을 뿐만 아니라, 재료 변경 혹은 두께 변경 없이는 두 개의 쌍안정 형상간의 곡률 차이를 구현이 불가능하다. 이러한 쌍안정 판 및 쉘 구조물의 형상학적 제한은 그 응용에 있어서 기술적 걸림돌이 되어왔다. 요약하자면, 해당 문제는 크게 두 개의 공학적 문제로 구분된다. 첫째는 '어떻게 원통형 형상을 가지는 전통적인 쌍안적 구조물의 곡률을 제어할 것인가?' 이고 둘째는 '어떻게 하면 비-원통형 형상을 가지는 쌍안정 구조물을 유도할 것인가? 이다. 이 문제를 해결하기 위해, 본 연구에서는 첫째, 초기에 곡률을 가진 원형판을 이용한 전통적인 쌍안정 구조물의 곡률을 제어하는 기술을 제안하였고, 해당 기술은 수치해석과 실험을 통해 검증되었다. 둘째, 가우스의 빼어난 정리에 근거하여 비-원통형 형상을 가지는 쌍안정 구조물을 구현할 수 있는 차세대 기술을 제안하였고, 해당 구현 기술은 수학적, 실험적으로 검증하였다.

좀 더 자세하게는, 비-원통형 형상을 가지는 쌍안정 구조물의 구현 기술은 동일한 가우스 곡률 텐서를 가지는 평면간의 변형에 있어서는 중립면 기준, 전단 변형이 발생하지 않는다는 기하학적 성질에서 착안되었다. 해당 기하학적 성질을 기반으로 하여 가전면이 아닌 초기 형상으로 비 가전면을 가지는 판 및 쉘 구조물 간의 완전 접합을 통해 비 가전면을 가지는 쌍안정 판 및 쉘 구조물을 구현하는 기술을 제안하였다. 이 기술은 레이레이-리쯔 해석법과 더불어 실험을 통해 보다 엄밀하게 검증하였다.

위의 쌍안정 구조물 관련 공학적 문제를 다루기 위해, 보다 효율적이면서도 정확도가 높은 모델을 개발하였다.

첫째, 기존의 레이레이-리쯔 해석에 있어서 쌍안정 판 및 쉘의 변형에너지는 본질적으로는 변위장으로 표현되지 않기 때문에 변위장이 아닌 임의의 변형률장 가정을 통한 해석이 보다 효율적이다. 이를 위해 단순히 외연적 변위장이 아닌, 적합조건이 부과된 임의의 변형률장을 기반으로 하는 새로운 개념의 해석기법 제안하였고, 고차의 변형률 장의 차수 변화에 따라 얻어지는 해석 결과들 간의 비교를 통해 제안한 해석 기법의 정확성과 효율성을 검증하였다.

둘째, 기존의 쌍안정 판 및 쉘 구조물의 해석 모델의 경우는 실제 쌍안정 판 및 쉘 구조물의 곡률이 판 이론으로 표현하기에는 너무 큼에도 불구하고 수치 미분의 정밀도 한계 및 계산의 복잡성으로 인해 판 이론에 기반한 해석 모델을 주요하게 사용되고 있다. 하지만 보다 정확한 해를 도출하기 위해서 본 논문에서는 쉘 이론에 기반한 해석 모델 또한 개발하였다. 해당 쉘 모델을 개발함에 있어서는 메트릭스 미분법 도입을 통해 지적 받아온 수치 미분의 정밀도의 한계 및 계산의 복잡성을 동시에 해결하였다. 결과적으로, 보다 정확하면서도 효과적으로 쌍안정 판 및 쉘의 해석이 가능해졌다.

마지막으로, 쌍 안정 판 및 쉘 구조물의 형상 해석 연구에만 국한하지 않고 실질적인 응용을 위해 좌굴 현상 중, 하나인 형상 전환에 대한 해석과 이를 통한 쌍 안정 쉘 구조물의 형상과 형상 전환 하중 간의 관계를 규명하는 연구가 수행되었다. 또한 해당 형상 전환을 유도하기 위한 작동기로 형상기억합금 스프링이 제안되었다. 먼저, 앞선 형상전환 해석을 통해 얻어진 형상 전환 하중 값을 토대로, 형상기억합금 스프링의 사양을 제안하였다. 제안된 형상기억합금 스프링의 형상기억효과 성능을 검증하기 위해 유한요소해석이 독립적으로 수행되었다. 형상기억합금의 형상기억 물질 거동 전산모사를 위해서는 라고다스(Lagoudas)의 형상기억합금 구성방정식이 이용되었다.

이 후 형상기억합금 스프링이 장착된 쌍안정 쉘 구조물에 대한 통합적 유한요소해석을 통해 형상기억합금 스프링을 이용한 효율적인 형상전환이 가능함을 검증하였다.

본 논문에서 제안되고 개발된 쌍안정 판 및 쉘 구조물의 형상 및 설계 기술을 토대로 쌍안정 구조물의 형상학적 제약을 해소하였다. 이렇게 개선된 쌍안정 판 및 쉘 구조물의 설계 자유도와 해당 구조물의 쌍안정 특성을 기계적 특성(즉, 강성 및 무게)만이 강조되어온 기존의 기계시스템에 적용한다면 성능 향상뿐만이 아닌 모핑이라는 새로운 개념을 추가하여 높은 부가가치를 가지는 기계시스템 설계 및 구현이 가능해 질 것이다.

주요어: 쌍안정, 판 및 쉘, 가우스의 빼어난 정리, 적합방정식, 형상기억합금 스프링

학번: 2009-23913